University of California

Los Angeles

Search for Low Mass Dark Matter with the XENON100 Experiment and Simulations for 1 ton and 10 ton Dark Matter Detectors

A dissertation submitted in partial satisfaction

of the requirements for the degree

Doctor of Philosophy in Physics

by

Ethan Craig Brown

2010

The dissertation of Ethan Craig Brown is approved.

Edward Young

Pietro Musumeci

Alexander Kusenko

Katsushi Arisaka, Committee Chair

University of California, Los Angeles

2010

To my loving wife . . .

Table of Contents

List of Figures

List of Tables

Acknowledgments

I would like to offer my sincere thanks to the many people who have helped make this thesis possible. I couldn't have done it without the help, advice and encouragement of so many along the way.

First I would like to thank the Department of Energy and the Pauley Foundation for funding my research and education costs. This work would not have been possible without your generous financial support.

Next, I give my thanks to my advisor, Professor Katsushi Arisaka, for giving me the opportunity to persue a PhD and perform this work.

I offer a special thanks for all of my collaborators, who have been like a second family for me the past few years. Among the many, Alfredo Ferella, Alex Kish, Ali Askin, Antonio Melgarejo, Eirini Tziaferi, Guillaume Plante, Kyungeun Lim and Marc Schumann helped me keep my sanity while living far from home, and offered invaluable advice. Also thanks to Rafael Lang, who gave me the best advice I have ever received for finishing a thesis. I also give my sincere thanks to Professor Elena Aprile for leading such a competetive collaboration and allowing me to be a part of it.

I would like to thank the UCLA group, Artin Teymourian, Kevin Lung and Michael Lam. Also, I am forever indebted to Hanguo Wang and Emilija Pantic, whose encouragement and advice helped me not only in the completion of this thesis, but in other areas of life as well. Thank you Emilija for encouraging me to attend the dark matter school in Les Houches, which completely changed my life.

I would also like to thank my family for giving me continual support and

encouragement. To my mother and father, thank you so much for your daily concern and your interest in my work and wellbeing.

Last, but certainly not least, I offer my deepest gratitude to my beloved wife, to whom this thesis is dedicated. You have carried me through such difficult times, and encouraged me to keep going when I thought I could not continue. I am here because of your endless support, and feel that I can never repay you.

Vita

1979	Born, Salt Lake City, Utah, USA.
2006	B.S. (Physics), University of California, San Diego
2006 - 2007	Teaching Assistant Physics and Astronomy Department, UCLA
2007 - Present	Research Assistant Physics and Astronomy Department, UCLA

Publications

K. Arisaka et al., *XAX: a multi-ton, multi-target detection system for dark matter, double beta decay and pp solar neutrinos.* Astropart. Phys. 31, 63 (2009).

XENON100 Collaboration (E. Aprile et al.), *First Dark Matter Results from the XENON100 Experiment.* arXiv:1005.0380v2.

Abstract of the Dissertation

Search for Low Mass Dark Matter with the XENON100 Experiment and Simulations for 1 ton and 10 ton Dark Matter Detectors

by

Ethan Craig Brown

Doctor of Philosophy in Physics

University of California, Los Angeles, 2010

Professor Katsushi Arisaka, Chair

The XENON100 experiment, located in the Gran Sasso National Laboratory (LNGS) in Italy, looks for dark matter in the form of Weakly Interacting Massive Particles (WIMPs) by observing scintillation and ionization signals in xenon in a dual phase Time Projection Chamber (TPC). This thesis presents an increased sensitivity to low mass WIMPs by reducing the energy threshold in the standard analysis, and by implementing a new analysis based on only the ionization signal, which allows XENON100 to probe the phase space consistent with claims of WIMP interactions in the DAMA/Libra and CoGeNT experiments. The results of this study are inconsistent with the other claims, as the absence of a dark matter signal in XENON100 allows an upper limit to be calculated for the WIMP-nucleon cross section that is well below the allowed regions from said claims.

Additionally, this thesis presents studies and developmental research for future large scale xenon dark matter detectors. Measurements were conducted to characterize a new low radioactivity photo sensor, the QUartz Photon Intensifying Detector (QUPID), which may serve as a key ingredient to build low background

1 ton and 10 ton scale detectors. Simulations were also performed to assess the mechanical design and light collection of these large detectors, whose sensitivity will be sufficient to probe many theories of dark matter, explore neutrinoless double beta decay in ^{136}Xe and detect solar neutrinos from the p-p chain.

CHAPTER 1

Dark Matter

One of the most amazing cosmological discoveries is that most of the universe is as yet undetected. In the last decades, scientists have determined that all of the visible matter in the universe contributes only 5% of the energy density of the universe. The remaining 95% is then a new form of energy that has thus far remained invisible. Current cosmology indicates that this is composed of two components, one of which is matter and comprises 25% of the universe. This new dark matter is a subject of great interest to physicists today, and countless theories have been developed to describe its nature. Currently, experiments are beginning to test some of these theories, and human-kind may well be on the verge of discovering this new form of matter. This thesis addresses one scientist's contribution to an experiment to detect dark matter and advance human-kind's understanding of the structure of the universe.

1.1 Evidence for the Existence of Dark Matter

There is a proponderance of evidence indicating that a substantial portion of the energy density of the universe is composed of a new form of non-baryonic matter called dark matter. Rather than exhausively cover the subject, the most important measurements are presented here, which not only indicate that dark matter must exist, but also give some insight to some of its characteristics.

1.1.1 Galactic Rotation Curves

The first evidence observed indicating that the universe contains a dark matter component came from the analysis of galactic rotation curves. The majority of the luminous mass of a galaxy is located at the galactic center, thus the motion of stars about the galactic center should be planet-like, that is, a body orbiting a central mass. In this instance, the circular velocity should scale as $r^{-1/2}$, where r is the distance to the galactic center.

However, this is not what is observed. The circular velocity instead remains constant out to very large distances, as demonstrated in figure 1.1 [33], indicating that galaxies do not follow planet-like motion. One solution to this is to impose a new matter distribution with a dark matter halo component with a mass density proportional to r^{-2}. The sum of the contributions from the visible matter in the disk and the dark matter in the halo reproduce the observed rotation curve. This was the first proposed model of dark matter, and remains one of the leading proofs of its existence today.

1.1.2 Gravitational Lensing

Further evidence for dark matter comes from the phenomenon of gravitational lensing. General relativity predicts that light bends in a gravitational field. Gravitational lensing occurs when a large gravitational field, such as a cluster of galaxies, lies between Earth and a distant luminous object. The gravitational field then acts as a lense, as light that travels in different directions around the gravitational field is focused to an observer on Earth. An astronomer sees multiple images of the distant object in different directions about the foreground galaxy cluster.

By measuring the amount of deflection of light by the field, gravitational

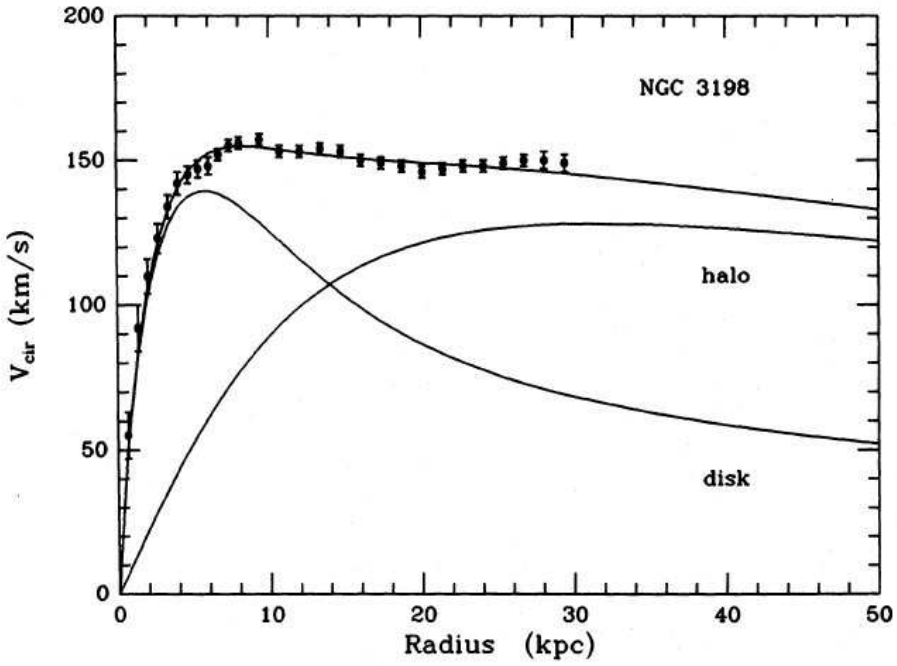

Figure 1.1: Rotation curve showing constant circular velocity as a function of galactic radius, which is consistent with the presence of dark matter

lensing can be used to determine the mass of the galaxy cluster. The luminous mass of galaxy clusters is calculated based on the x-ray luminosity, so the two methods can be used to compare the luminous and gravitational mass. When this comparison is made, there is disagreement, indicating the presence of a non-luminous mass in the cluster, which is currently understood to be due to the presence of dark matter.

In addition to this, there is a particular gravitational lensing measurement whose peculiar characteristics indicate that the dark matter interpretation is correct. The Bullet Cluster is a system of two galaxy clusters that have recently collided. In the collision process, the stars, which are point like objects, do not collide, but simply pass by one another. Should dark matter be present in the clusters, it too would interact only gravitationally and the two dark matter halos

would pass through one another unaffected. The hot gas in the cluster, however, is diffuse and collides, slowing down in the process. Thus, the star fields are ahead of the gas after the collision. Since the majority of the luminous mass is in the hot gas, one would expect that without the presence of dark matter, the gravitational mass would trail the star fields as well after the collision.

Figure 1.2 shows that this is not the case. The green contours show the gravitationoal mass, as measured by gravitational lensing, which follows the star field shown on the left. The hot gas, shown on the right, trails both the star fields and the gravitational mass after the collision, indicating that the luminous mass is not the dominant component of the clusters. This is consistent with dark matter models, and more importantly, illiminates, or at least severely constrains, other theories such as modified newtonian dynamics. The Bullet Cluster is considered by many in the field to be conclusive evidence for the existence of dark matter.

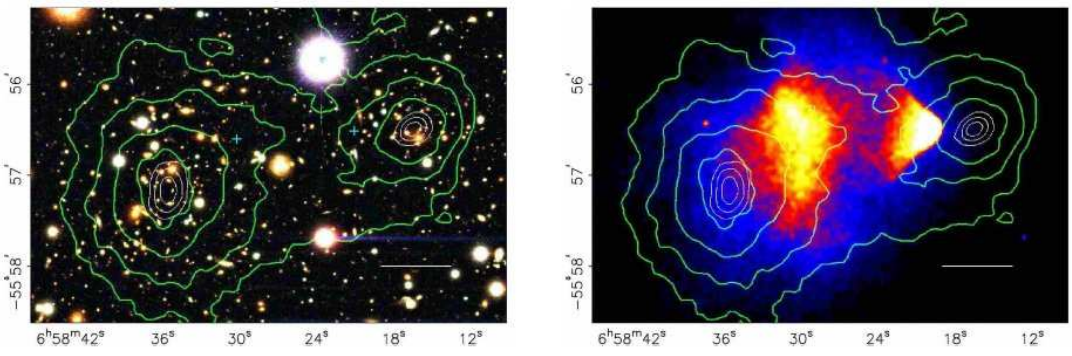

Figure 1.2: Map of the gravitational potential of the Bullet Cluster 1E0657-558 from [12]

1.1.3 CMB Measurements

The cosmic microwave background (CMB) is a very nearly uniform background of photons in all directions on the sky. Its spectral distribution follows a black body spectrum of a body at 2.73 K. In the early universe, the temperature was high enough that matter was ionized, and thus photons could not propagate freely. As the universe expanded and cooled, the matter de-ionized, and the photons could then propagate and thus decoupled from the matter. As the universe has continued to expand since that time, the free photons have redshifted to microwave wavelengths, which is what is detected today.

The precise temperature of the CMB today, then, tells detailed information about the temperature, or equivalently the energy density, at the time of decoupling. The Wilkinson Microwave Anisotropy Probe (WMAP) made very precice measurements of the anisotropy of the CMB on the entire sky [28]. From the angular power spectrum shown in figure 1.3, the size of the energy density fluctuations can be derived, thus yielding a map of the mass distribution in the early universe. From this, the seven year data from WMAP [28] has been used to measure both the total matter density and the baryonic matter density. The analysis shows that the matter component is $\Omega_m h^2 = 0.1265 \pm 0.0080$ and the baryonic component is $100\Omega_B h^2 = 2.230 \pm 0.074$. Thus, baryonic matter only contributes 18% of the matter density in the universe, and the remaining matter in the universe must be non-baryonic. As the baryonic density matches the luminous mass measurements, the non-baryonic matter component must be non-luminous. This not only provides a precice measurement of the amount of dark matter, but constrains its characteristics, telling that it must be non-baryonic.

Combining the precice measurements from WMAP with the observational evidence from galactic rotation curves and gravitational lensing measurements,

in addition to other evidence which has not been presented here, the standard cosmological model is naturally developed. In this model, 5% of the universe is ordinary matter, 25% is composed of non-baryonic dark matter, and the remaining 70% is an unknown component called dark energy.

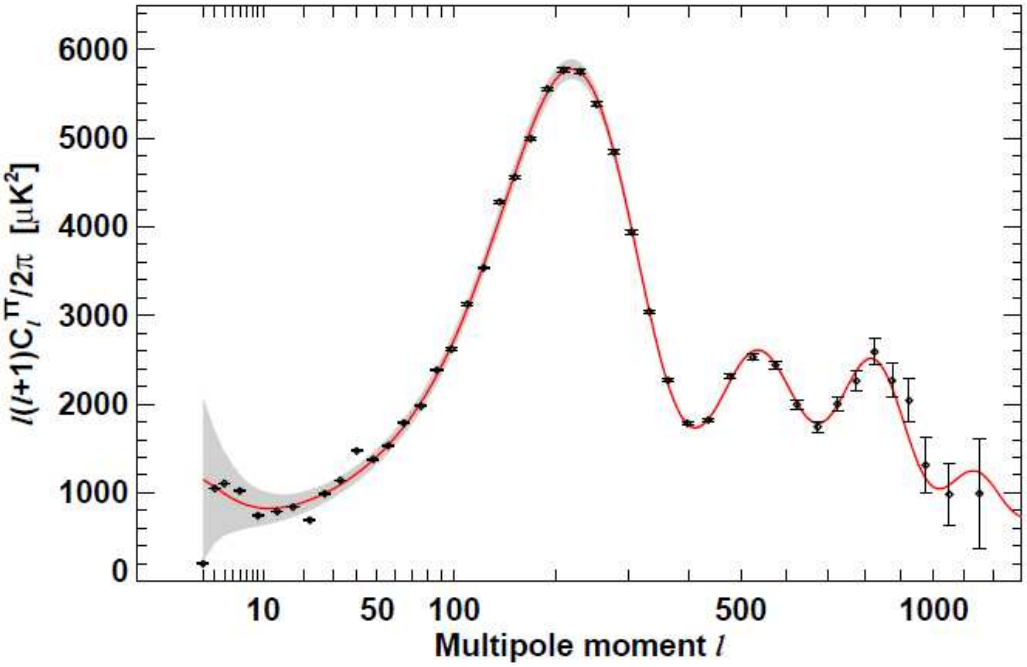

Figure 1.3: Angular Power Spectrum of the CMB Anisotropy measured by WMAP [28]

1.2 Dark Matter Theory

1.2.1 Supersymmetry

There is one proposed theory of dark matter that falls naturally out of known physics, namely a supersymmetric dark matter particle. The standard model of particle physics describes electromagnetic, weak, and strong interactions from a

quantum field theory approach. All of the characteristics of every known particle are derived from the Lagrangian. There are, however, certain shortcomings of the standard model, and extensive efforts have been made to add new physics to it. One such extension is to add an extra symmetry to the Lagrangian between bosons and fermions called Supersymmetry (SUSY). In this model, every boson in the standard model would have a supersymmetric fermion partner, and every fermion would have a boson partner, thus doubling the number of particles in the standard model.

If SUSY were an exact symmetry, superparticles would share all quantum numbers except spin with their partner particles, including mass. If the masses of the superparticles were identical to that of their partner particles, they would have been created in collider experiments. But as no SUSY particles have been detected thus far, for SUSY to exist in nature it must be a broken symmetry, which would allow for the masses of particles and superparticles to be different. This, however, fits naturally into the standard model, since the Higgs mechanism, which gives rise to electroweak symmetry breaking in the standard model, can also break SUSY. There is one technicality to this, namely that to avoid anomalies in the Lagrangian, two scalar Higgs bosons are required, and accordingly two fermion superpartners. Since the Higgs boson has not yet been detected, it is certainly plausible that there are two such scalar particles as opposed to one as required by the standard model. The number of elementary particles in SUSY would then be double the number in the standard model plus two.

In the standard model, the descrepency between the expected mass of the yet undetected Higgs boson at $\tilde{1}80$ GeV and the Planck energy scale at 10^{19} GeV. To determine the Higgs mass from the quantum field theory calculation, terms from contributions of bosons and fermions must cancel to one part in 10^{34}. By

adding supersymmetric particles, the cancelation comes naturally since bosons and fermions contribute with opposite signs. Thus, SUSY provides a natural explanation to this discrepency.

SUSY is also added to the standard model to arrive at a unification of forces at a high energy scale. In the standard model, the electromagnetic and weak interactions are united into a single electroweak interaction. The standard model alone, however, cannot combine all forces into a grand unified theory (GUT). The addition of SUSY allows for this. Figure 1.4 shows how the strength of the coupling of each force changes with energy with and without SUSY. When SUSY is included, the forces meet at a single point. This is a suggestion that SUSY may be a necessary extension of the standard model.

While SUSY could solve existing problems with the standard model, it is by no means simple. When unconstrained, it contains 105 free parameters [27] in addition to those already present in the standard model. Thus, in order to develop managable theories out of it, several simplifying assumptions are made. The most common of these comprise the minimal supersymmetric standard model (MSSM) and reduce the number of free parameters to 4 valued parameters and one sign. These constraints have been used to develop many different SUSY theories.

One of the constraints in the MSSM is conservation of a quantity called R-parity, which is a quantum number assigned to all particles and superparticles. Each particle has an R-parity of $+1$ and each superparticle has an R-parity of -1. A consequence of conserving this quantum number is that two superparticles must be present at every interaction vertex, and accordingly, the lightest superparticle cannot decay and is stable. This lightest supersymmetric particle (LSP) is then a likely candidate for dark matter.

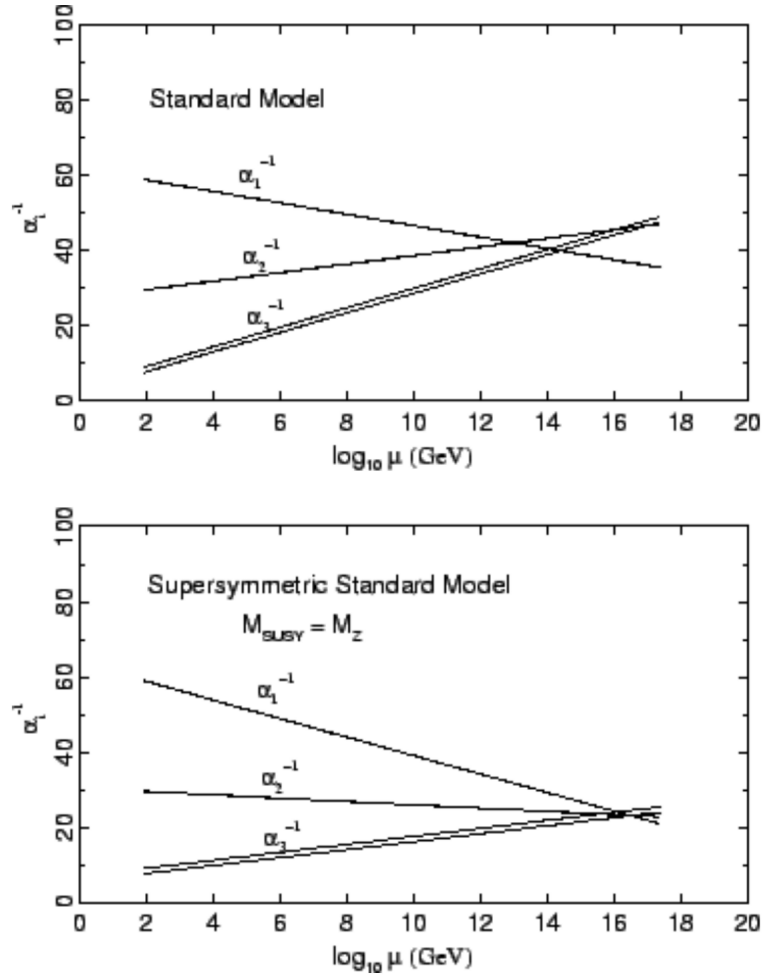

Figure 1.4: Energy Dependence of Force Couplings, without (top) and with (bottom) SUSY. When SUSY is introduced, the couplings meet at one point, indicating force unification at that energy

1.2.2 The WIMP

While there are many proposed dark matter particles, one that shows great promise for current experimental searches is the weakly interacting massive particle (WIMP). Other theories indeed have merit, but the purpose of this thesis is to take one such theory and place it under the experimentalist's microscope to

test its validity. The theory chosen for this is WIMP dark matter.

There are four neutral particles in SUSY that are likely the LSP. They are a linear combination of the partners of the two Higgs bosons and of the neutral gauge bosons, and are called the neutralinos, χ. The neutralino is assumed to be a majorana particle, meaning it is its own antiparticle and can thereby annihilate with other neutralinos.

Assuming the neutralino is the LSP, and that it has weak scale interactions with ordinary matter, a simple production mechanism for dark matter exists. In the early universe, all particles and superparticles are present in thermal equilibrium. As the universe expands and cools, there is no longer sufficient energy to create heavy particle antiparticle pairs. The remaining heavy particles will then decay into lighter particles. For the LSP, however, R-parity conservation dictates that there is no lighter particle to decay into, so it remains stable.

When the universe was in thermal equilibrium, the density of wimps was high enough that the annihilation rate was equal to the production rate. As the universe became too cold to produce WIMPs, they kept annihilating and the number density decreased. This continued until the number density was too low for WIMPs to find one another, at which point they froze out and a relic of WIMPs remained. This is shown schematically in figure 1.5. The point where the freeze out occurs is dependent on the cross section of the WIMP. For a higher cross section, the WIMPs annihilate longer, and the relic density is lower.

The interaction of WIMPs with ordinary matter, in addition to providing a production mechanism, provides a means of detecting them by looking for signatures of WIMPS scattering off of a target material. Indeed, this is why this theory is so exciting from an experimentalist's viewpoint, as one can simply build detectors to probe the predicted phase space of said interactions, and either con-

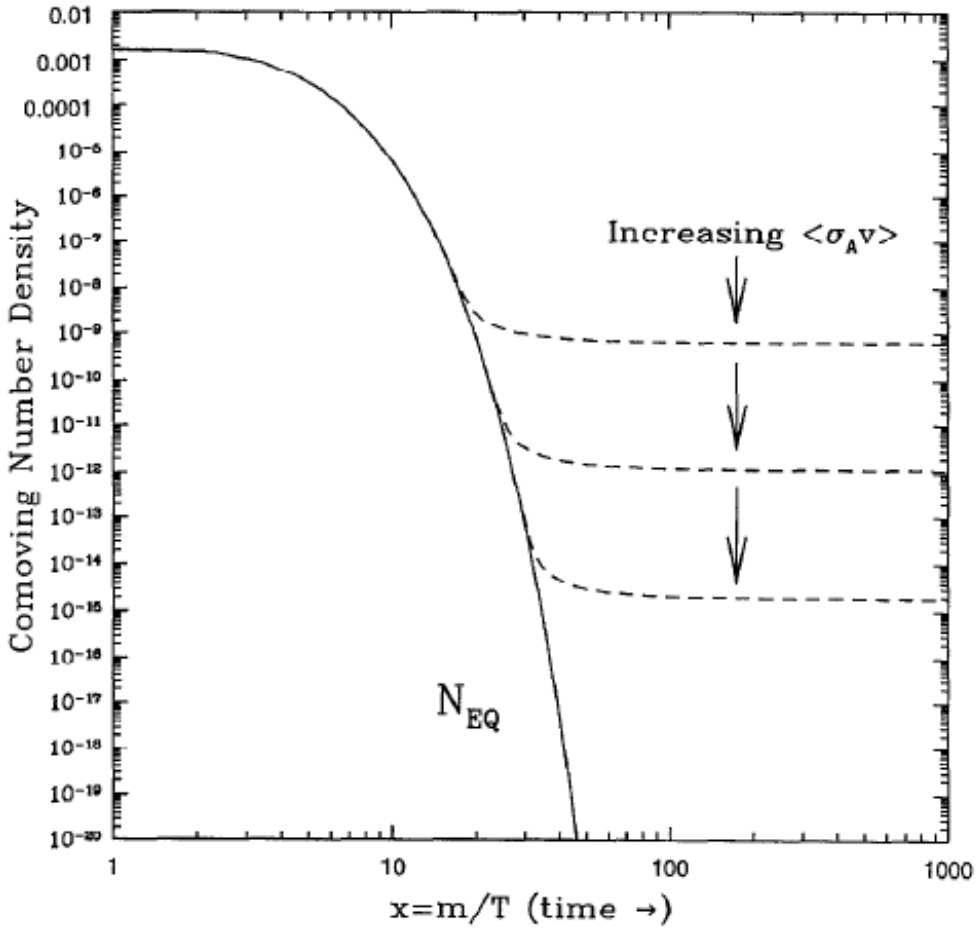

Figure 1.5: Diagram of the freeze out process for the production of WIMP dark matter

firm or refute the WIMP theory of dark matter. Such experiements are now well developed and significant progress has been made in recent years, as is outlined in section 1.3.

1.3 Experimental Detection

There are two general branches of detection methods utilized in current experiments to detect WIMP dark matter. Indirect searches look for the signatures of

WIMP annihilations in the universe. Since this requires to WIMPs meeting, the rate is proportional to the square of the dark matter density. These then often focus on regions where the local dark matter density is high to enhance the signal. Experiments such as Fermi and Veritas are currently utilizing this technique and indirect dark matter searches are under way.

The other branch of experiments looks for direct dark matter interactions with a target material in a detector. The weak coupling of WIMPs to ordinary matter gives rise to two fundamental kinds of interactions in such a detector. The WIMP can either have a spin coupling to a target nucleus (spin dependent), or it can couple coherently to the nucleus (spin independent). Many experiments are currently looking for these interactions.

1.3.1 Interaction Rate

The WIMP interaction in a target is a combination of both spin dependent and spin independent components, and experiments accordingly are designed to measure one or the other, and in some cases both. In general, the differential interaction rate in any target can be written as

$$\frac{dR}{dQ} = \frac{2\rho_0}{m_\chi} \int_{v_{min}}^{v_{esc}} \frac{d\sigma}{d|\mathbf{q}|^2} v f(v) dv, \tag{1.1}$$

where $\rho_0 = 0.3$ GeV/cm^3 is the local dark matter density, m_χ is the WIMP mass, v and $f(v)$ are the speed and speed distribution of the WIMPs in the galaxy, $v_{min} = (Qm_N/2m_r^2)^{1/2}$, $v_{esc} = 544$ km/s is the escape velocity of WIMPs in the Milky Way, $Q = |\mathbf{q}|^2/2m_N$ is the recoil energy, m_N is the mass of the nucleus, and $\frac{d\sigma}{d|\mathbf{q}|^2}$ is the differential cross section. The difference between the spin dependent and spin independent rates comes from the difference in the differential cross sections. While xenon is sensitive to both types of interactions, the focus of this thesis is on the spin independent interaction. Thus, only this will be presented

in detail.

The spin independent interaction is due to a coherent scatter off of the nucleus and has a differential cross section given by

$$\frac{d\sigma}{d|\mathbf{q}|^2} = \frac{\sigma_0}{4m_r^2 v^2} F^2(Q), \tag{1.2}$$

where σ_0 is the nuclear scattering cross section at zero momentum transfer, m_r is the reduced mass of the WIMP nucleus system, and $F^2(Q)$ is the nuclear form factor. Typically the Helm form factor is used, which has the form [23],

$$F(Q) = \frac{3j_1(qR_1)}{qR_1} exp(-qs), \tag{1.3}$$

with $q = \sqrt{2Qm_N}$, $R_1 = \sqrt{R^2 - 5s^2}$, $R = 1.2A^{1/3}$ fm, $s = 1$ fm, and $j1(x)$ is a spherical bessel function.

For the integral over velocities, a form for the speed distribution must be chosen. This is typically taken to be a Maxwellian distribution. Accounting for the relative motion of the earth and sun through the galaxy v_e, and the escape velocity of dark matter particles v_{esc}, the integral becomes [29]

$$\int_{v_{min}}^{v_{esc}} \frac{f(v)}{v} dv = \frac{2}{v_0\sqrt{\pi}} \frac{k_0}{k_1} \times \left[\frac{\sqrt{\pi} v_0}{4v_e} \left(erf\left(\frac{v_{min}+v_e}{v_0} \right) - erf\left(\frac{v_{min}-v_e}{v_0} \right) \right) - exp\left(-\frac{v_{esc}^2}{v_0^2} \right) \right], \tag{1.4}$$

where $v_0 = 220$ km/s is the speed of the sun about the center of the galaxy and,

$$k_1 = k_0 \left[erf\left(\frac{v_{esc}}{v_0} \right) - \frac{2v_{esc}}{\sqrt{\pi} v_0} exp\left(-\frac{v_{esc}^2}{v_0^2} \right) \right]. \tag{1.5}$$

The zero momentum cross section is can be written as [27]

$$\sigma_{0SI} = \frac{4m_r^2}{\pi} [Z f_p + (A - Z) f_n]^2, \tag{1.6}$$

where Z is the number of protons in the nucleus, A is the number of nucleons, and f_p and f_n are the couplings to the proton and neutron respectively. For coherent scattering, it is typical to make the approximation $f_p = f_n = f_N$, and the cross section can be written in terms of the proton cross section σ_p as,

$$\sigma_0 = A^2 \left(\frac{m_r}{m_p}\right)^2 \sigma_p, \tag{1.7}$$

then the differential rate for spin independent scatters can be written as

$$\frac{dR}{dQ} = \frac{\sigma_p \rho_0 A^2}{\sqrt{\pi} v_0 m_\chi m_p^2} F^2(Q) \, \frac{k_0}{k_1} \times \left[\frac{\sqrt{\pi} v_0}{4 v_e}\left(erf\left(\frac{v_{min}+v_e}{v_0}\right) - erf\left(\frac{v_{min}-v_e}{v_0}\right)\right) - exp\left(-\frac{v_{esc}^2}{v_0^2}\right)\right]. \tag{1.8}$$

Using equation 1.3.1 in combination with the correct form factor, it is straightforward to calculate the differential scattering rate in any detector. Figure 1.6 shows such a calculation for a WIMP mass of 100 GeV and a cross section of 10^{-44} cm^2 for a variety of target nuclei. Heavy targets like xenon give the largest rate at low energies, but at higher energies the form factor suppression makes lower mass targets like germanium and argon more sensitive.

1.3.2 Current Dark Matter Search Experiments

There are currently countless experiments in operation and in design to detect dark matter both directly and indirectly. While dark matter has yet to be definitevely detected, the leading experiments in the field are now beginning to probe the regions of phase space where many SUSY dark matter theories predict the neutralino to exist. Figure 1.7 shows the region of $\sigma - m$ space where theory predicts the neutralino to lie and exclusion curves from recent experiments for spin

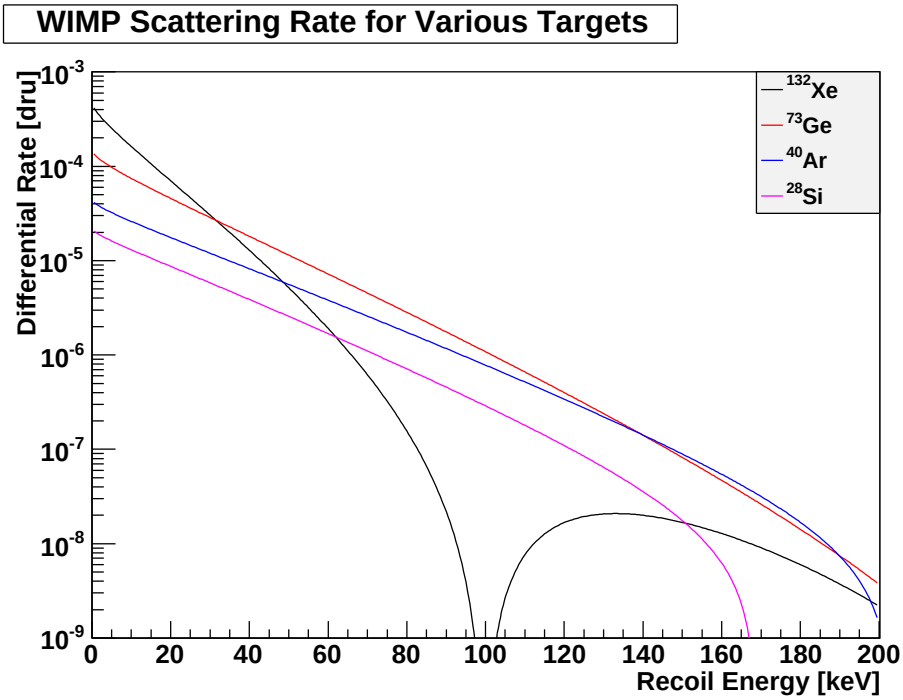

Figure 1.6: Differential WIMP spin independent scattering rate for several targets with $m_\chi = 100$ GeV and $\sigma_p = 10^{-44}$ cm^2

independent interactions. Experiments are sensitive to cross sections above the limit curve for each WIMP mass, so the absense of a signal in these experiments excludes the region of phase space above the limit curves. Indeed, experiments are currently beginning to probe the predicted region of phase space, and will thus be able to discover the WIMP or refute specific theories.

The most sensitive experiments in the spin independent search have been conducted by the XENON and CDMS collaborations, each taking turns releasing results with the most sensitive limit on the spin-independent cross section at the time. XENON10 and CDMSII each reached a sensitivity of 5×10^{-44} cm^2, with CDMSII being more sensitive at higher WIMP masses.

Both experiments look for signatures of nuclear recoils, which are characteris-

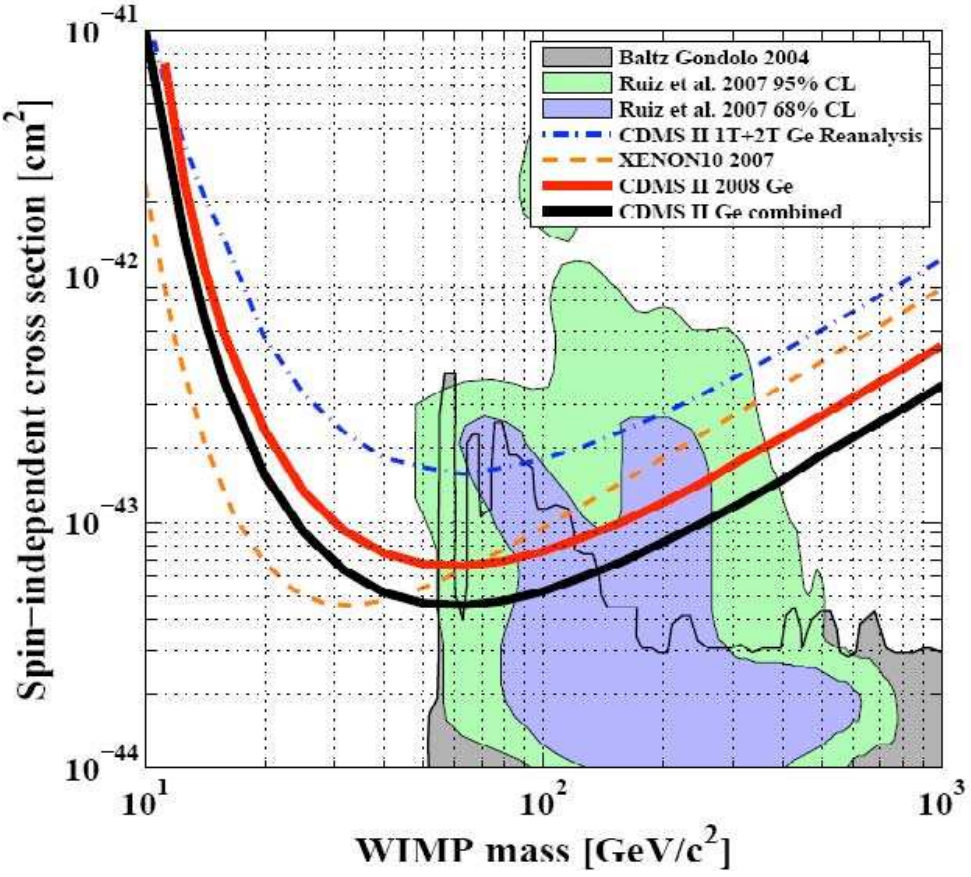

Figure 1.7: Phase space of WIMP-nucleon spin independent scattering with theoretical predictions, as well as exclusion curves from experiments

tic of WIMPs coherently scattering off of a nucleus of the target material. They utilize discrimination techniques to apply an event by event rejection of electron recoils, and reconstruct the position of events to fiducialize the volume, accepting only events from the quiet central region.

CDMS operates germanium and silicon cryogenic crystals, and monitors the heat and charge signals from interactions to search for WIMPs. The experiment uses the ionization energy per unit phonon energy, which is much larger for electron recoils than nuclear recoils, to discriminate the two types of interactions

and reduce the gamma background. Additionally, the risetime of the phonon signal is used to remove events from the surface, reducing the background even further.

Of particular interest is the most recent result from the CDMSII combined data, the bottom curve in figure 1.7. Two events were observed within the WIMP acceptance region with an expected background of 0.8 ± 0.3 events. This is certainly within the fluctuations of the background, since by Poisson statistics there is a 23% probability of observing 2 or more background events, but the CDMS collaboration claims that this may constitute a dark matter signal.

XENON, on the other hand, uses a dual phase xenon target inside of a time projection chamber (TPC) that monitors the light and charge signals of interactions. The ratio of the charge to light signals provides a discrimination of electron recoils, and position reconstruction based on the charge drift time and the charge signal pattern allows for fiducialization to remove surface backgrounds. XENON10 achieved a sensitivity of 4.5×10^{-44} cm^2 at 30 GeV and XENON100 has released its first results with a sensitivity of 3×10^{-44} cm^2 at 50 GeV, similar to the sensitivity of CDMS but with no background events [14]. This will be discussed in chapter 3.

One advantage of the liquid xenon detectors is that they are easily scalable by orders of magnitude in size. Additionally, the high Z value gives rise to a strong self shielding ability, so the background is reduced substantially by implementing large fiducial cuts for large scale detectors, thereby making ton scale and multiton scale detectors a feasible possibility in the near future. XENON is currently preparing a 1 ton scale detector and studies have been conducted for the development of a 10 ton scale liquid noble detector (see chapter 7 and reference [5]), showing great promise for increasing the sensitivity to the spin independent

WIMP cross section by orders of magnitude over the next years.

Searches for dark matter have not, however, simply yielded null results and corresponding cross section limits. In particular, the DAMA and CoGeNT collaborations have observed signals in their detectors and have made claims of dark matter discoveries. While these claims have been met with a great deal of controversy, particularly since other experiments have found contradictory results, their findings are presented here and will be addressed in detail in chapter 4.

The DAMA collaboration used NaI crystals to search for an annual modulation signal, characteristic of dark matter interactions. Since the earth's motion through the galaxy is different in summer and winter, due to the motion with or against the sun's motion, the speed distribution for dark matter changes, giving rise to a change in the event rate in a detector. DAMA has searched for this signal as a detection method for dark matter.

Figure 1.8 shows the modulation signal from the DAMA/LIBRA [9], where a clear modulation is visible in summer vs winter. However, since DAMA's NaI detectors do not have the possibility of distinguishing nuclear recoils from electron recoils, their search is only sensitive to the modulation of all events and it is impossible to determine what kind of particle was involved in any given interaction. This is the source of the criticism that the collaboration has received, as they cannot claim with absolute certainty that the modulation is not due to some other background.

If the DAMA signal is due to WIMPs, the mass and cross section would be constrained as shown in figure 1.9 [19], which shows the allowed region in $\sigma - m$ phase space with and without ion channeling in the detector, as well as exclusion curves from XENON10 and CDMSII. Note that the majority of the accepted region has been ruled out by XENON and CDMS, with the only

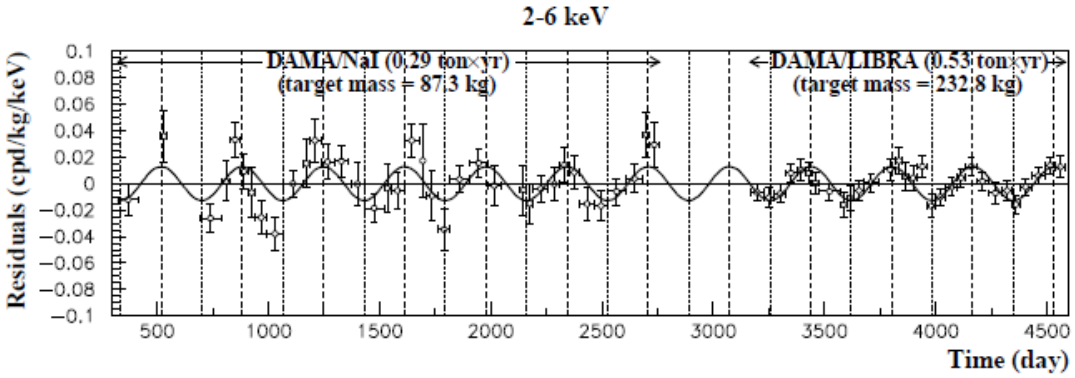

Figure 1.8: Annular modulation signal from DAMA/LIBRA [9]

remaining compatibility being a low mass WIMP. Further constraints on the compatibility of low mass WIMPs and the DAMA results are presented in chapter 4.

Like DAMA, the CoGeNT collaboration has seen a signal in its detector and has stated that it is evidence for a dark matter detection. CoGeNT uses germanium crystals, similar to those used in CDMS but with a lower energy threshold. The collaboration claims that hundreds of low energy events are due to scatters from low mass (7 GeV) WIMPs [1], similar to the DAMA results. Also like DAMA, this has been met with criticisms that claim the signal is likely due to unknown backgrounds. The phase space where WIMPs are compatible with the CoGeNT data is shown in figure 1.10, along with the favored region for DAMA and theoretical models. Also shown is the exclusion curve for the CDMSII combined results along with the region compatible with the 2 observed CDMS events as dark matter events.

The next phase of experiments is therefore in an interesting and exciting position. As the sensitivity is increased for high WIMP masses, experiments will probe the predicted regions of phase space and be able to confirm or deny specific

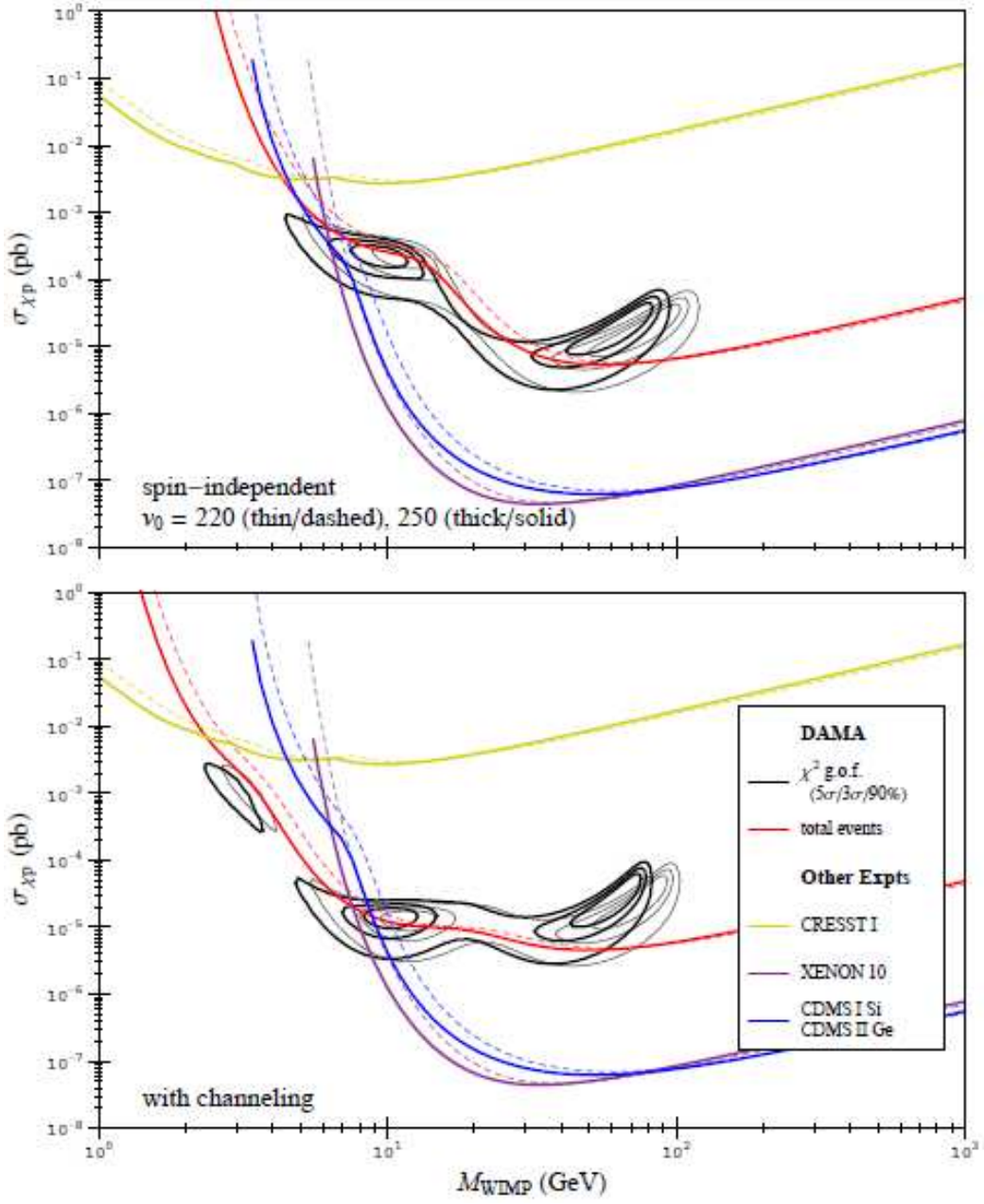

Figure 1.9: Allowed region for DAMA with (bottom) and without (top) ion channeling and exclusion curves from CDMSII and XENON10

theories. Additionally, the sensitivity to low mass WIMPs is also necessary to resolve the conflict surrounding the DAMA and CoGeNT claims. Both of these

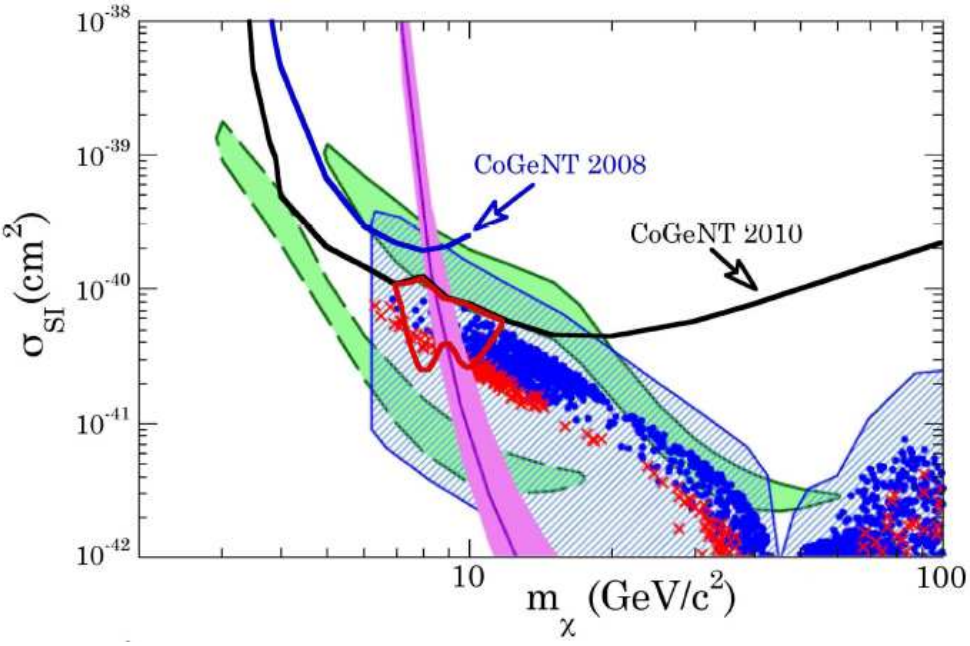

Figure 1.10: Preferred region for CoGeNT data (red contour) and DAMA data (green contours, dashed including channeling), as well as theoretical predictions (thatched blue and scatter plots)

items are addressed in the remainder of this thesis.

CHAPTER 2

The XENON100 Detector

While dark matter detectors are being constructed from a great variety of materials, dual phase xenon detectors have several advantageous properties that have allowed competitive searches to be performed. This chapter outlines these properties relevant to the dark matter search and specifically how they are utilized in the XENON100 detector to obtain the highest sensitivity to WIMP recoils.

2.1 Liquid Xenon as a Dark Matter Target

Liquid xenon is known to be a good scintillator, emitting UV photons at 178 nm. When a particle interacts with the xenon target, the energy transfer is split between ionization and excitation. In the absence of an electric field, the ionization component recombines, and along with the excitation component, emits the uv photons through an excimer state as it decays back to the ground state. Because the photons come from the decay of the excimer state, xenon atoms do not absorb their own scintillation light, so this light can be collected by photo multiplier tubes (PMTs) surrounding the target. When an electric field is applied, some of the ionization component does not recombine and can be collected independently from the light.

An advantage of xenon is that its scintillation light can be directly detected by PMTs since quartz windows are transparent to 178 nm light. Thus, no wave-

length shifting is necessary, as is the case for argon scintillation light for example. Additionally, photocathodes have been developed that are highly sensitive to UV light, achieving a relatively high quantum efficiency (QE), or probability of collecting a photoelectron emitted by an incident photon, of greater than 30%.

Since dark matter recoils typically deposit an energy of only a few keV, corresponding to a few electrons, the ionization signal is too small to be read out directly. A common technique to collect these small ionization signals is the use of a dual phase Time Projection Chamber (TPC). The target volume inside of the TPC is filled with liquified xenon and a small gas gap is left at the top. The electrons are drifted by a strong electric field to the top of the liquid volume, and are then extracted into the gas phase where the field is high enough to induce photoluminescence and a secondary scintillation pulse is created proportional to the ionization signal (S2). The time delay between the prompt scintillation of the excitation component (S1) and the proportional scintillation of the ionization component (S2) allows the two signals to be collected by the PMTs independently.

Typical TPCs for liquid xenon detectors are composed of a cylindrical reflective surface, such as teflon, and are monitored above and below by PMTs. Xenon has a high index of refraction of 1.67 at UV wavelengths, so there is a strong total internal reflection at the liquid gas interface. Therefore, the majority of the S1 light is collected by the bottom PMT array, and the top is used to collect the S2 light, which is emitted in the gas phase. Since the S2 is emitted very close the the top PMTs, there is a strong localization, which can be used to reconstruct the x and y position of an interaction, the details of which will be presented in section 2.4.1. Additionally, the uniform drift speed allows for a linear conversion from drift time to depth within the detector, thereby allowing for a three dimensional position reconstruction.

The ability to measure both the primary scintillation and the ionization component of an interaction is of crucial importance for discrimination between electron recoils and nuclear recoils. The ratio of S2 to S1 is much larger for electron recoils than for nuclear recoils, so an event by event discrimination is possible to distinguish these two types of interactions. Since WIMPs scatter coherently off of the nucleus and other particles such as gammas scatter off of the electron cloud, the electron recoil background can be reduced substantially by this technique, allowing for increased sensitivity to WIMPs.

Another profound advantage of xenon as a target is that it has a self shielding property. Due to its high Z of 54, the gamma stopping power is very high, as shown in figure 2.1, so low energy gammas do not penetrate deeply into the target. This gives rise to a great possibility for background reduction by fiducialization, accepting only events from the quiet central region of the detector.

Of particular importance is the fact that xenon has no long lived radioactive isotopes, and can hence be made incredibly radiopure. Contaminants such as ^{85}Kr can be removed by distillation, creating an environment effectively free from internal radioactive backgrounds. Additionally, naturally produced xenon is composed of nearly half odd isotopes, allowing for the measurement of both spin dependent and spin independent interactions.

2.2 The XENON100 Detector

2.2.1 The Physical Detector

XENON100 is the current stage of the XENON dark matter search program, and is composed of 165 kg of xenon in a dual phase TPC. The cryostat is built from low activity stainless steel, and the internal structure is built from low activity

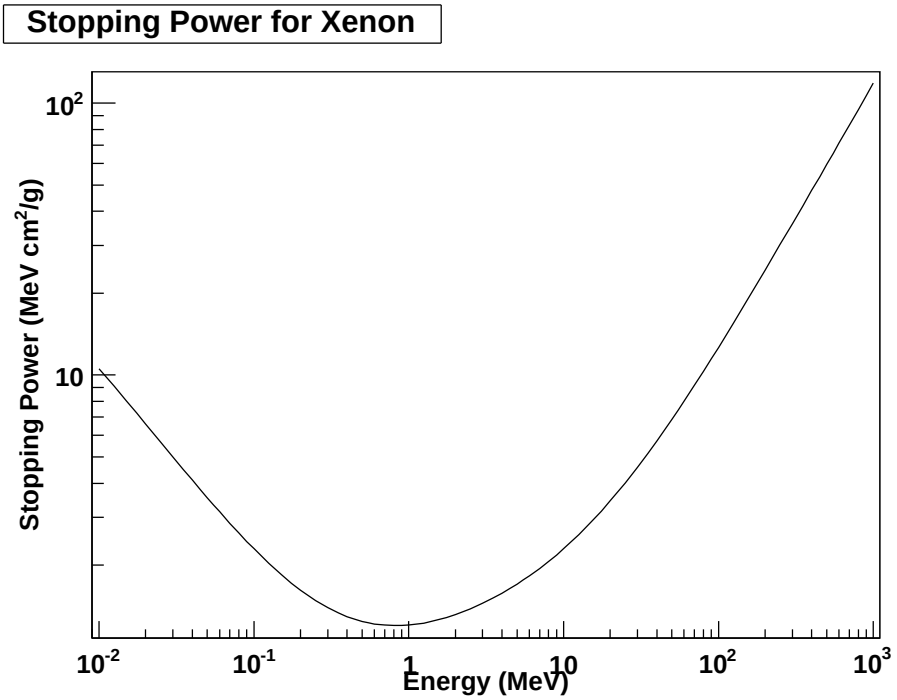

Figure 2.1: Stopping power as a function of energy for gammas in xenon.

teflon and copper.

The TPC is 30 cm high by 30 cm diameter, and is built from a teflon reflector. The bottom of the TPC is monitored by 80 high QE ($> 30\%$) PMTs closely packed for optimal S1 light collection. The top of the TPC has 98 PMTs spread in a circular pattern, including a row outside the edge of the TPC, to reconstruct event positions from the S2 hit pattern. These PMTs, which are reused from XENON10, have a lower QE around 20%, but this is acceptable since the majority of the S1 light is collected by the bottom array.

Additionally, the TPC is surrounded entirely by a 2 cm layer of liquid xenon, which is monitored by 64 additional PMTs and used as an active veto for background reduction purposes. In order to fill the top veto with liquid xenon without filling the gas layer in the TPC, the top of the TPC is built as a diving bell so

that an overpressure can be applied to the gas. Figure 2.2 contains a picture and diagram of the detector. In the diagram in figure 2.2(a) the internal structure of the TPC is visible, while the picture in figure 2.2(b) shows the veto region and diving bell structure.

(a) Diagram (b) Picture

Figure 2.2: Diagram and picture of the XENON100 detector.

The PMTs used in the detector are the same as those used in XENON10, the Hamamatsu R8520. They are low activity photo tubes with a quartz window, and are specifically designed for a high QE for xenon scintillation light.

The drift field in XENON100 is maintained by applying a negative bias voltage to a cathode made from a stainless steel transparent mesh. Another transparent

screening mesh held at ground is located 2.5 mm below the liquid surface. A field of 500 V/cm is maintained inside the TPC to separate and drift the charge signal. A double layer of field shaping rings inside the teflon reflector serve to maintain a uniform field at the side of the TPC.

Similarly, the anode is constructed of a transparent screening mesh 2.5 mm above the liquid surface. This is held at 4 kV to collect the charge and to maintain the high field necessary for electron extraction and to induce proportional scintillation. No field shaping is necessary since the anode is so close to the screening mesh.

2.2.2 Event Recording

The waveforms of events are recorded for all 242 PMTs individually. However, a zero length encoding algorithm is used to reduce the data size by suppressing signals below a threshold on each channel. This threshold is set at one third of a photoelectron so that noise is suppressed while single photoelectron signals are recorded with high efficiency.

The hardware trigger is based on S2 signals, and uses an integrator to trigger on large signals spread over 1-2 μs. Since large S1s can also cause a trigger, the waveform is digitized for 320 μs centered at the trigger so that the maximum drift time of 160 μs can be captured on either side of the trigger. In this way, events that trigger on a large S1 are still capable of recording an S2 from the bottom of the detector, and events triggering on an S2 from the bottom of the detector can record the associated S1 at the beginning of the waveform. The FADCs used for digitization utilize a circular buffer that allows for zero deadtime in the acquisition process.

The trigger threshold is set just above the noise, and has >99% efficiency

at 300 pe, which is well below the energy threshold utilized in the dark matter analysis.

2.3 Background Reduction

The backgrounds for XENON100 are essentially limited to two categories, gammas and neutrons. Alphas and betas from external radioactive sources do not penetrate the detector, and those from internal sources have a high energy deposition and are therefore not of concern for the dark matter region.

The cosmic ray background is reduced by conducting the dark matter search in a deep underground laboratory. XENON100, for example, is located in the Laboratori Nazionali del Gran Sasso in Italy, which at a depth of 3100 meters water equivalent (MWE) blocks all of the cosmic ray background except for the energetic muons, which act as a neutron source.

The remaining background is due to the neutrons generated in alpha-n reactions after an alpha decay and gammas associated with radioactive decays in materials within the detector and in the environment.

External backgrounds from the radioactive elements in the laboratory environment are reduced by a passive shielding structure. The shield, from outside to inside, is composed of 20 cm of lead, the inner 5 cm of which has a low activity of ^{210}Pb, followed by a 20 cm layer of polyethylene, which in turn is followed by a 5 cm layer of copper. Additionally, the four vertical walls of the shield are surrounded by a 20 cm layer of water. Figure 2.3 shows both a diagram and the actual shielding structure used for the experiment, but does not include the 20 cm of water on the sides.

While the event discrimination from S2/S1 reduces the electron recoil back-

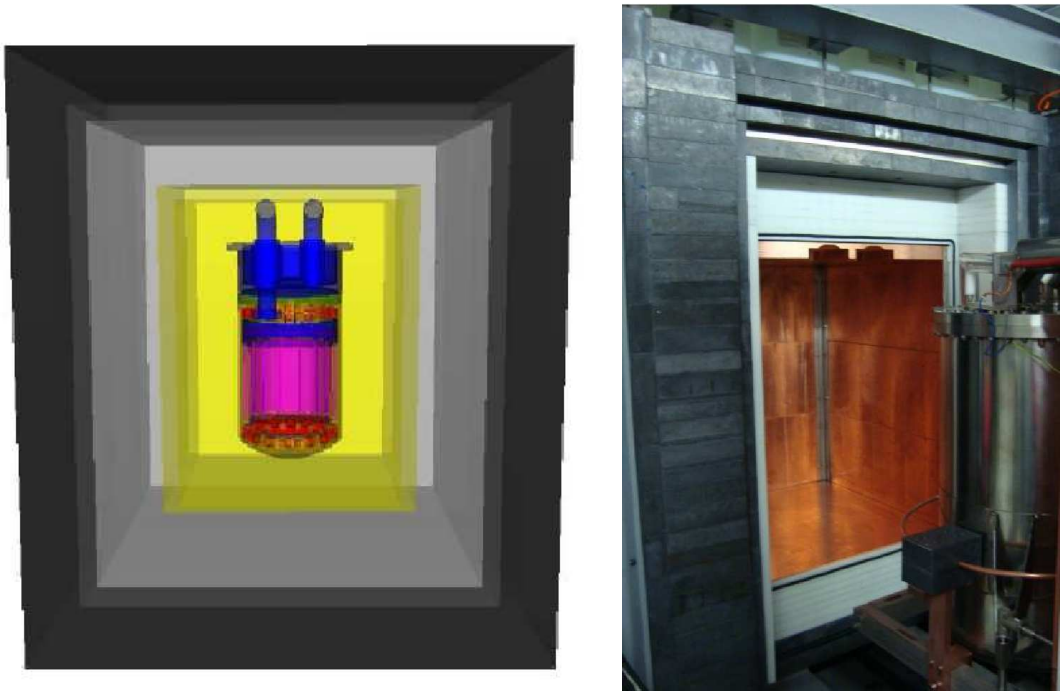

(a) Diagram (b) Shield

Figure 2.3: Shielding structure for XENON100, showing the two lead layers, the polyethylene layer, and the copper layer with the detector inside. The water shield on the four vertical sides is not shown.

ground from gammas, the leakage into the nuclear recoil band makes the discrimination imperfect. Therefore, the gamma background must be reduced as much as possible. Gammas come primarily from radioactive decays of ^{60}Co and ^{40}K and from the decay chains of ^{238}U and ^{232}Th decay chains. Neutrons are also generated from alpha-n reactions in the ^{238}U and ^{232}Th decay chains, as well as from the Pb^{210} decay chain and muon induced neutrons.

The shielding structure is also used to reduce the level of radon gas in the detector environment. ^{222}Rn accumulates naturally underground as it is produced in the decay chain of ^{238}U and is itself radioactive. While the laboratory provides a flow of fresh air from outside the mountain to blow the radon out from

underground, this does not reduce the level of radon to adequate levels for a dark matter search. To further reduce the level of radon in the detector environment, nitrogen gas is blown inside the shielding structure to purge radon from the structure to a level of < 1 Bq/m^3.

Internal backgrounds are reduced as much as possible by choosing ultra clean materials for construction of the detector. A screening was conducted for all materials that were used in the detector to ensure that they were indeed sufficiently radiopure, and also to obtain the activity for use in monte carlo simulations of the background. Table 2.1 lists the measured activity for all materials used in the detector and the shielding structure.

Material	**Unit**	**^{238}U [mBq/unit]**	**^{232}Th [mBq/unit]**	**^{60}Co [mBq/unit]**	**^{40}K [mBq/unit]**	**^{210}Pb [Bq/unit]**
Stainless steel	kg	< 1.7	< 1.9	5.5±0.6	< 9.0	
PTFE	kg	< 0.31	< 0.16	< 0.11	< 2.25	
PMTs	piece	0.15±0.02	0.17±0.04	0.6±0.1	11±2	
PMT bases (cirlex)	piece	0.16±0.02	0.07±0.02	<0.01	<0.16	
Support bars (steel)	kg	< 1.3	2.9±0.7	1.4±0.3	< 7.1	
Copper (inside)	kg	< 0.22	< 0.16	0.20±0.08	< 1.34	
Resistor chain	piece	0.027±0.004	0.014±0.003	< 0.003	0.19±0.03	
Cathode support ring	kg	3.6±0.8	1.8±0.5	7.3±1.3	< 4.92	
Top grids support rings	kg	< 2.7	< 1.5	13±1	< 12	
PMT signal cables	kg	< 1.6	3.7±1.8	< 0.69	35±13	
Copper shield	kg	< 0.07	< 0.03	< 0.0045	< 0.06	
Polyethylene shield	kg	0.23±0.05	< 0.094	< 0.89	0.7±0.4	
Lead shield (inner)	kg	< 0.66	< 0.55	< 0.11	< 1.46	26±6
Lead shield (outer)	kg	< 0.92	< 0.72	< 0.12	14±3	530±70

Table 2.1: Measured activity of each material used in the XENON100 detector.

One additional feature particular to XENON100 is that the feedthrough tubes for all of the electronics extend through the shielding structure, so all external electronic components are located outside the shield. This is a key design difference from XENON10, which greatly reduces the amount of radioactive materials inside the shield, thus reducing the overall background.

In addition to passive shielding, there is an active veto of liquid xenon that

completely surrounds the TPC. This serves not only to reduce the gamma background from external sources, but also to tag events associated with decays within detector materials.

Background particles that do scatter within the detector without depositing energy in the veto can still be rejected. Since WIMPs will only scatter once in the detector due to the extremely small cross section, a multiple scatter cut is applied to remove double scatters from gammas or neutrons.

Backgrounds that are not screened or tagged from these methods are ultimately reduced by a fiducial cut. By rejecting all events near the edge of the detector, and selecting only those far from detector materials in the center of the detector, the background is reduced to an acceptable level for a dark matter search.

The final background level is due to a combination of leakage events from the aforementioned reduction techniques and radioactive decays of impurities within the xenon itself. Constant recirculation of the xenon through a getter removes electronegative impurites, but there is still a contamination due to non electronegative elements such as ^{85}Kr. To address these backgrounds, the xenon is purified by distillation prior to the experiment to reduce the amount of ^{85}Kr to the ppb level.

2.4 Calibration of XENON100

The characteristic behavior of XENON100 is understood based on a series of detailed calibrations, which are designed to provide a full understanding of the position, energy and recoil type of a given interaction. These calibrations are described in this section.

2.4.1 Position Reconstruction

The position of events within the detector are primarily of interest for the purposes of fiducialization and position dependent corrections, such as the energy calibration. It is therefore desirable to reconstruct the x-y-z position of an event with fair accuracy. The position reconstruction of an event in the TPC is broken naturally into two parts. The z position is determined by the time difference between the S1 and S2 while the x-y position is determined by the hit pattern of the S2 on the top PMT array.

The determination of the z position is quite simple, since electrons drift at a constant velocity of 1.8 mm/μs. There is a diffusive process also affiliated with the drift, but this should only modify the width of the S2, as the electron cloud as a whole moves at the drift velocity. The contribution from diffusion is therefore minimized by defining the drift time as the time between the peaks of the S1 and S2 signals, which should correspond to the drift time of the center of the electron cloud. The z position is then simply the drift velocity divided by the drift time. The resolution of the z position is determined by the width of the S2, and is estimated to be < 2 mm.

The reconstruction of the x and y coordinates is more complicated as it is based on the hit pattern of the S2 on the top PMT array. Three different algorithms have been developed for this purpose, based on a neural network, a vector regression, and a chi-squared minimization. The algorithms are trained based on Monte Carlo simulations of S2s inside the detector using Geant4. All three algorithms are consistent, and have a resolution of < 3 mm.

2.4.2 PMT Calibration

The signal from each PMT must be converted into a physical variable, so that an interpretation can be made. The gain, which is the ratio of charge output to charge input to the multiplication chain, is a natural physical variable for a PMT. It converts the signal in ADC counts to the number of photoelectrons (pe) ejected from the photocathode.

Part of the work performed for the PMT calibration was done for this thesis, and is presented in detail in chapter 5. The main results are briefly summarized here.

The gain of all 242 PMTs in XENON100 is measured inside the detector with % level error. This allows for periodic calibrations throughout the detector operation, as well as a calibration in the conditions of the dark matter search. Weekly calibrations are performed, and the gains are monitored continuously, both to ensure that the PMT performance is not degrading and to measure and correct for long term drifts in gain. The gains are then implemented in the raw data processor to convert all PMT signals to pe.

2.4.3 Energy Calibration

Determination of the energy of an event is a somewhat delicate process. The detector responds differently to electron recoils than to nuclear recoils, so a different energy scale is needed for these two types of events. Dark matter interactions occur as nuclear recoils, so it is ultimately the nuclear recoil energy scale that is important for dark matter searches. However, since the background is composed of electron recoils, this energy scale needs to be fully understood as well.

The electron recoil energy scale, or electron equivalent energy, is measured in

units of keVee. To perform this calibration, a ^{137}Cs source was used, which emits 662 keV gammas. The single gamma line allows for an absolute calibration of the energy scale by fitting the full absorption peak of the spectrum to obtain the number of photoelectrons per keVee. Since this is dependent on the light yield, which itself depends on the xenon purity, weekly calibrations are performed. In addition to the absolute calibration, these high energy gammas penetrate the entire TPC, allowing for position dependent corrections to be made.

The resolution of the energy scale can be improved by invoking the anti-correlation between S1 and S2, which arises from fluctuations in recombination. Using this method, an electron equivalent energy has been developed, which is a function of S1 and S2, with a resolution of $\sigma/E = 1.9\%/\sqrt{E}$.

The nuclear recoil energy, measured in keVr, is not as straightforward to measure for two reasons. First, the energy scale is determined by nuclear quenching, which is a non-linear effect, thereby making the energy scale non-linear. Second, neutron sources give a spectrum of energies. Consequently, great care must be taken to disentangle the source spectrum from the energy scale measurement. For this reason, dedicated measurements have been used to define the nuclear recoil energy scale.

The nuclear recoil energy is related to the S1 signal by,

$$E_{nr} = \frac{S1}{LY}\frac{1}{\mathcal{L}_{eff}}\frac{S_{ee}}{S_{nr}}, \tag{2.1}$$

where LY is the S1 Light Yield in pe/keVee, S_{ee} and S_{nr} are the field quenching factors, measured to be 0.58 and 0.95 respectively at the operational voltage of 530 V/cm [4], and $\mathcal{L}_{eff}$ is the nuclear quenching factor. $\mathcal{L}_{eff}$ is then the critical variable to measure, as it contains the energy dependent conversion from S1 to nuclear recoil energy.

Several dedicated experiments have been performed to measure $\mathcal{L}_{eff}$ [3] [30]

[6] [36]. The difficulty arises at the lowest energies, where the measurements do not agree well. To account for the disagreement, a global fit was made to all measurements of $\mathcal{L}_{eff}$, and a constant extrapolation was used below 4 keVr where there are no data available. Figure 2.4 shows this fit with the 90% CL contours, along with all of the measurements.

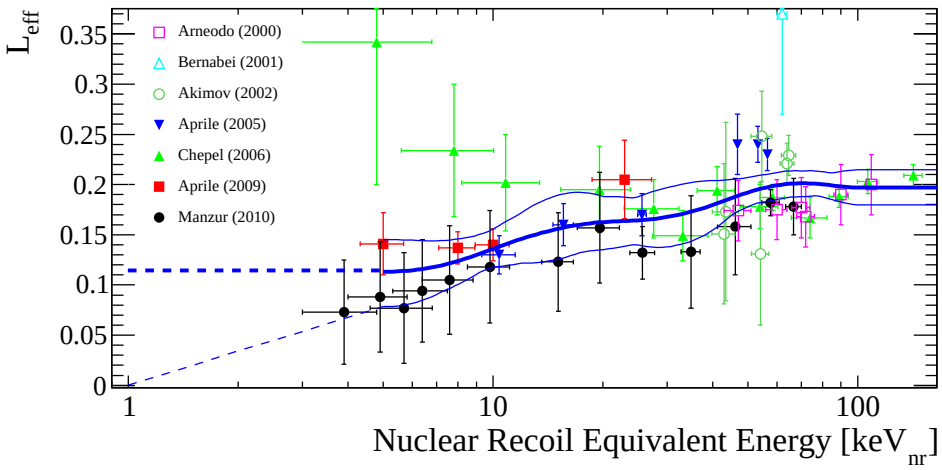

Figure 2.4: Global fit and 90% CL contours with all measured data for $\mathcal{L}_{eff}$

Once the energy scales are defined, the detector response to electron recoils and nuclear recoils can be measured using dedicated calibration runs. The electron recoil band is measured using gammas from a ^{60}Co source while the nuclear recoil band is measured using neutrons from an ^{241}AmBe source. Figure 2.5 shows these bands in the parameter of log10(S2/S1) as a function of nuclear recoil energy. The different response of this parameter for the two bands allows for event by event discrimination between electron and nuclear recoils (described in section 3.1.1).

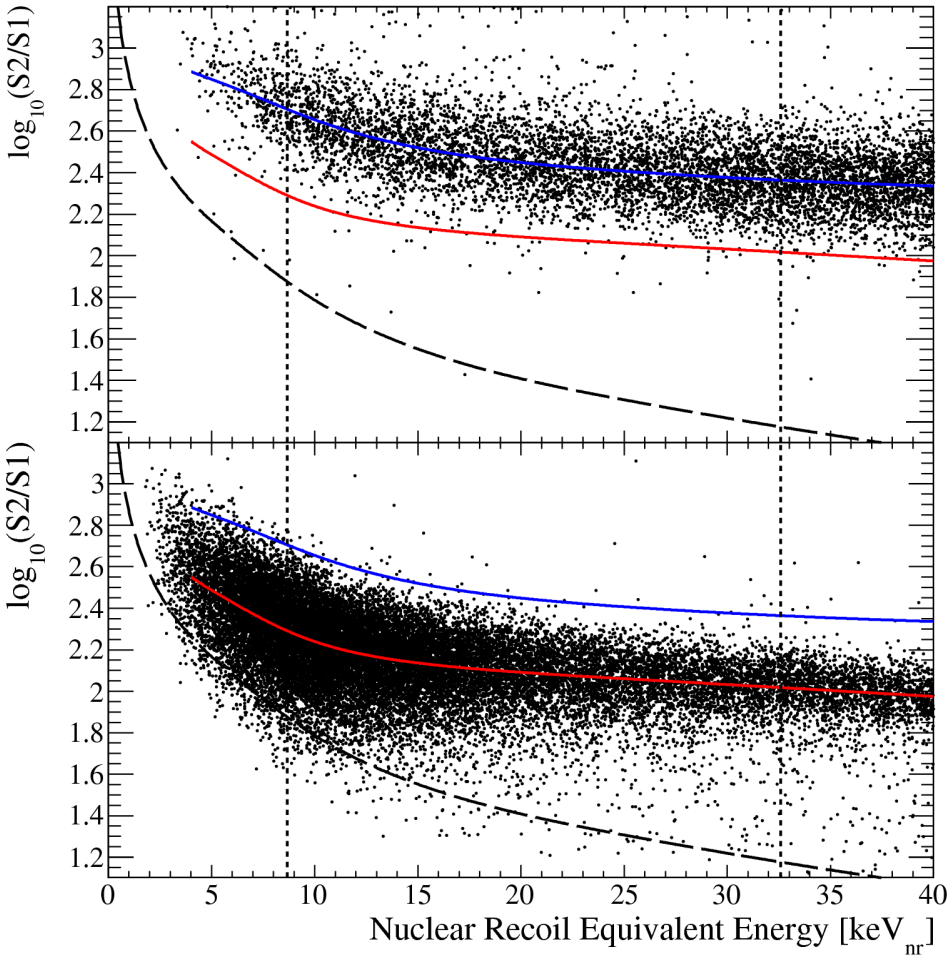

Figure 2.5: Detector response to electron recoils from a ^{60}Co source (top) and nuclear recoils from an ^{241}AmBe source.

CHAPTER 3

First Dark Matter Results from XENON100

The standard analysis for the first dark matter results from XENON100 [14] are presented in some detail in this chapter. While this analysis was a collaborative effort, the work for this thesis described in chapters 4 and 5 are based to a large extent on this analysis. Therefore, the focus of this chapter is on the portions of the standard analysis that are relevant to the remainder of the thesis.

The analysis is based on data obtained in October and November of 2009, with a total of 11.17 days exposure. Usually, a blinded analysis is performed, in which the analysis is based on a limited sample of data and the experiment is run without looking at the data for the WIMP search. The analysis is finalized before the data are unblinded, then the results are presented based on the pre-defined analysis. This was not done for the first results of XENON100 because these data were acquired during the commissioning phase of the detector. Since XENON100 is so massive, the sensitivity of this limited data sample is competitive with other dark matter searches. Hence, this non-blind analysis demonstrates the low background operation of the detector, as well as giving competitive scientific results. A dedicated blinded run has subsequently been performed, and the results of this are upcoming.

3.1 Data Cuts

A series of data quality cuts was developed to remove spurious events, with a focus of leaving the nuclear recoil band unchanged, thus increasing the signal to noise ratio without drastically reducing the efficiency for nuclear recoils.

3.1.1 Description of Cuts

The first cuts are based on the hardware S2 trigger threshold of the detector. A software threshold is implemented at 300 pe for S2s, which is high enough that it has 100% efficiency. All S2s smaller than 300 pe are discarded.

This software threshold can then be used to implement a multiple scatter cut. Since the cross section of WIMP-nucleon scattering is so low, the probability of a double scatter in the detector is essentially zero. Thus, any double scatters must be due to background. Double scatters occur on a shorter time scale than the scintillation process, so the S1s from the distinct scatters are combined into one larger S1. However, the S2s will be collected separately as long as the vertical distance between the scatters is large enough that the S2s do not overlap. The typical width of an S2 in the energy range of interest is 0.5 μs, so multiple S2s can be distinguished when separated by more than 1 μs = 1.7 mm. The drift region in the TPC is 30 cm, so this cut is 99.4% effective for scatters above threshold.

For the S1 signal, a coincidence cut was applied requiring a 2 fold coincidence within 20 ns window. Each S1 must have at least 2 PMTs above threshold within the window for the S1 to be considered valid. This avoids misidentifying dark counts from PMTs, which appear as single photoelectrons, as S1s. In addition, events with multiple S1s, each of which must pass the coincidence cut, are discarded.

Similarly, the active veto is implemented by requiring that there be no S1 in the veto region in coincidence with an S1 inside the TPC. This helps identify high energy backgrounds from outside the detector, as well as backgrounds from the TPC materials.

A cut is made based on the signal to noise ratio for a waveform. The noise is defined as the area of the entire waveform and the signal is the area of the S1 and S2. Events with a signal to noise ratio less than one are discarded.

When particles scatter in the gas phase above the anode, an S1 and S2 are still produced. The S2 occurs when the drifted charge approaches the anode to the point where the field is high enough to produce proportional scintillation. This, however, is spread over a longer time than the S2s created by charge extracted from the liquid, so the width is much larger. Therefore, an S2 width cut was developed to remove such events.

Additionally, a few PMTs exhibited a large amount of noise in various circumstances. Cuts were developed to exclude these PMTs from the waveform in these instances.

The final cuts are based solely on background rejection, as opposed to data quality. The first of these is a fiducial cut, which removes surface backgrounds (as described in section 2.1). Only events within a radius of 135 mm and a depth between 33 mm and 276 mm were kept, defining a 40 kg fiducial target.

The other background reduction cut distinguishes electron recoils from nuclear recoils based on the variable S2/S1. The detector response to electron recoils is calibrated with gammas from a ^{60}Co source, and the nuclear recoil response is calibrated with neutrons from a ^{241}AmBe source. These bands, shown in figure 2.5 are shown again here in figure 3.1. The mean of the electron recoil band is shown with the blue curve and the mean of the nuclear recoil band is shown with

the red curve for both the upper and lower plots. The value of $\log_{10}$(S2/S1) is much larger for electron recoils than for nuclear recoils, thus the electron recoil band is separated from the nuclear recoil band by this variable. A cut is defined at the mean of the nuclear recoil band, effectively removing the majority of the electron recoils while only reducing the sensitivity to nuclear recoils by 50%. Also shown in this figure are the software threshold of 300 pe marked by the dashed curve and the energy window for the WIMP search marked by the vertical dashed lines.

3.1.2 Cut Efficiencies

The cut efficiencies, or probability that a WIMP event will pass the cuts, have been estimated as a function of S1, or equivalently as a function of energy. These estimations are described here.

Because WIMPs have essentially zero probability to double scatter, the efficiency of the multiple hit cut is 100%. Similarly, since other data quality cuts are used to identify S1s in the TPC and the active veto, the veto anticoincidence cut and single S1 cut have an efficiency of 100%.

For the remaining cuts, the energy dependent cut efficiency had to be estimated by another means. To do this, the data from the ^{241}AmBe calibration were used to estimate the effect that each cut had on the nuclear recoil band as a function of energy. Good nuclear recoil events were defined as events that passed all data cuts except two. Then the efficiency of a given cut was defined as the fraction of these events that passed said cut.

Figure 3.2 shows the resultant cut efficiency as a function of S1 for all data quality cuts cumulatively, excluding the fiducial and S2/S1 cuts, as these are treated separately.

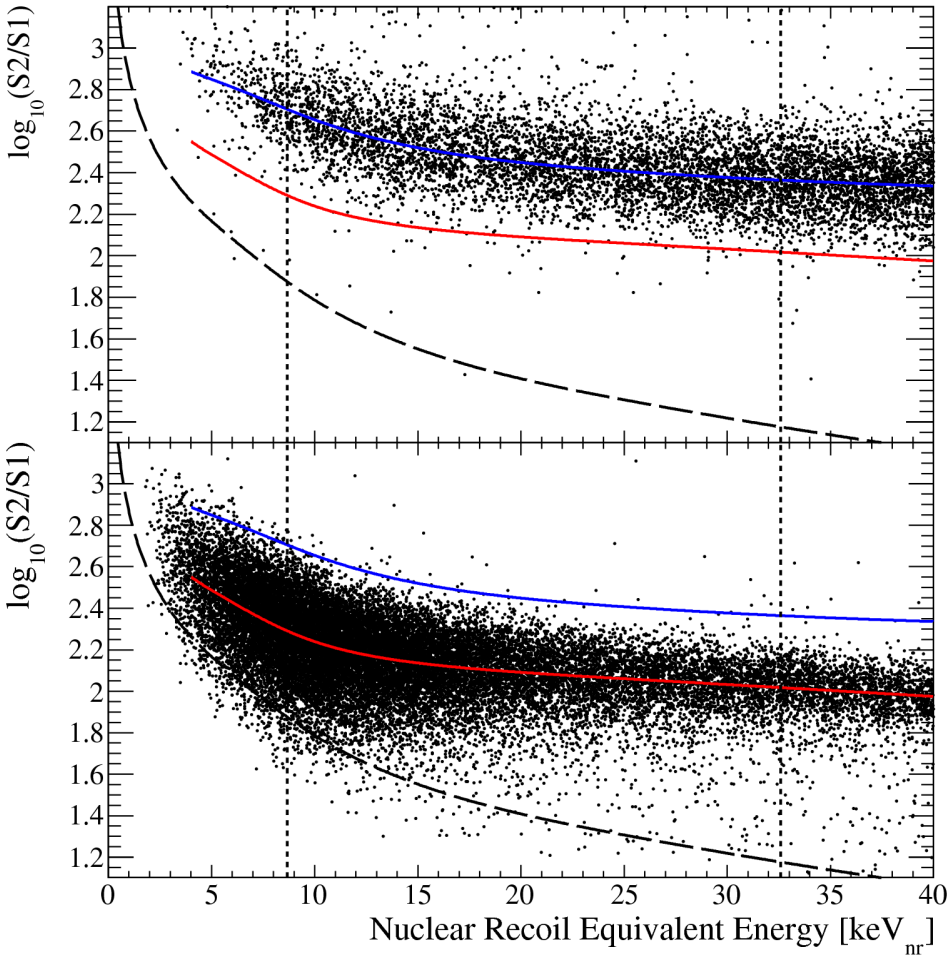

Figure 3.1: Detector response to electron recoils from ^{60}Co gamma rays (top) and nuclear recoils from ^{241}AmBe neutrons. The mean of the electron recoil and neutron recoil bands are marked with the blue and red curves respectively. The S2 software threshold of 300 pe is marked with the dashed curve and the energy range considered for the WIMP search is marked with the vertical dashed lines.

The efficiency for the background rejection cuts is known exactly. The fiducial cut simply reduces the target mass. This is accounted for in the sensitivity calculations. The S2/S1 cut has 50% efficiency at all energies, since it is defined at the mean of the nuclear recoil band.

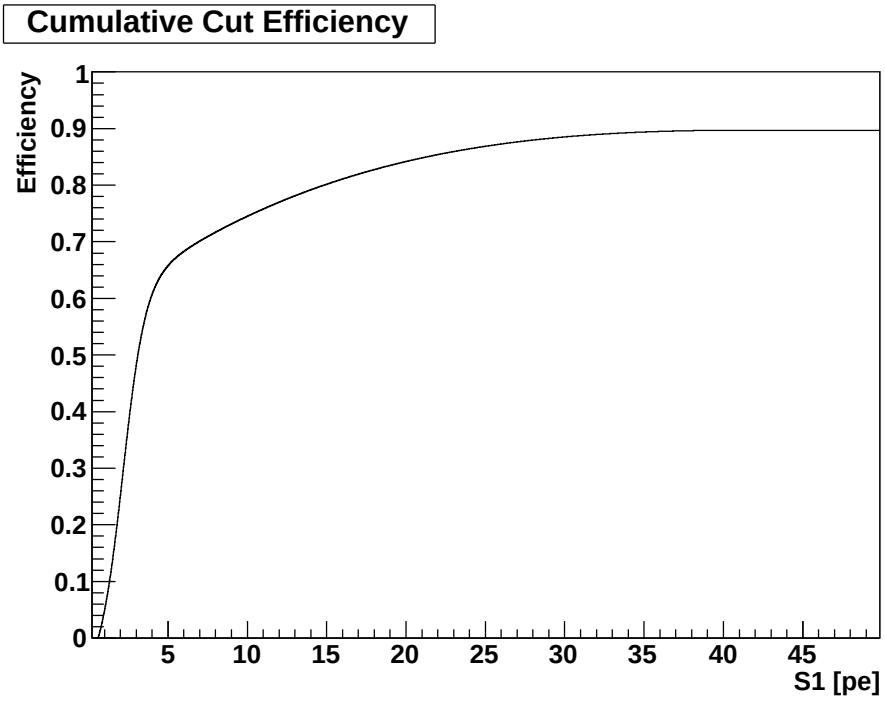

Figure 3.2: Efficiency as a function of S1 for all data quality cuts, excluding the fiducial and S2/S1 cuts.

3.2 Energy Window for WIMP Analysis

The energy threshold for the standard XENON100 analysis is determined by the light yield of the detector. With a threshold of n photoelectrons, the energy threshold is not merely found by converting n pe to keVr, but is rather found by considering Poisson fluctuations in the number of photoelectrons from all energies. That is, events with a recoil energy corresponding to a mean of μ pe have a likelihood to have an S1 with k photoelectrons according to the Poisson distribution,

$$P(k;\mu) = \frac{\mu^k e^{-\mu}}{k!}. \tag{3.1}$$

Therefore, a threshold of n photoelectrons has contributions from energies above and below the corresponding energy, smeared according to equation 3.1. Thus, the relevant variable for defining the energy window is photoelectrons, not energy. However, it is customary to convert this to an energy window, but one should recall that a Poisson smearing of the photoelectron distribution is always implied.

For the standard analysis, a lower threshold of 4 pe was chosen because the efficiency remains high ($> 60\%$) above this threshold. An upper threshold of 20 pe was chosen, since this is high enough to include the dominant portion of the dark matter spectrum for the WIMP mass ranges considered. Using the global fit for $\mathcal{L}_{eff}$, this corresponds to an energy window of $8.67 < E < 32.59$ keVr.

3.3 Limits on Dark Matter Cross Section

As previously mentioned, the data used for the first results of XENON100 were collected in October and November of 2009, comprising 11.17 days of livetime. A non-blind analysis was performed using the cuts described above. The distribution of events within the TPC for this data set is shown in figure 3.3, which shows all events with a black dot and events with S2/S1) less than the nuclear recoil mean with a red circle. The 40 kg fiducial volume is shown with the dashed lines. Indeed, the majority of the events are located near the edge of the detector, consistent with surface backgrounds, and of the 22 events in the fiducial volume, none are below the nuclear recoil mean.

All events within the 40 kg fiducial volume are shown in figure 3.4, which shows the S2/S1) vs nuclear recoil energy. This figure clearly shows that all 22 events within the energy window are within the electron recoil band, above the nuclear recoil mean. At the top of this figure, the efficiency curve from figure

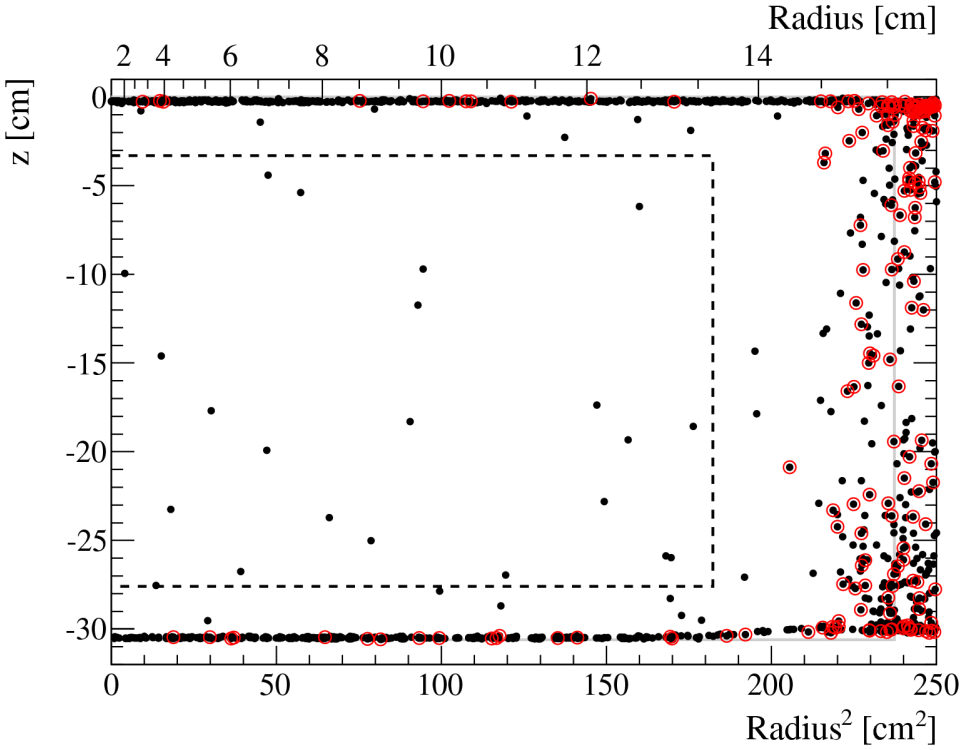

Figure 3.3: Distribution of all events (black dots) within the TPC in the energy range of 8.67 to 32.59 keVr used for the WIMP search. Events that with S2/S1) below the nuclear recoil mean are marked with a red circle.

3.2 is shown as well, but with the x axis converted to keVr. Thus, there are no candidate WIMP events in this data set, nor are there any electron recoil backgrounds in the WIMP search region.

With a background free data set for a WIMP search, it is straightforward to calculate the sensitivity of the run and set an upper limit on the dark matter cross section as a function of WIMP mass. In this analysis, the statistical method of Feldman and Cousins [21] was used. A data set with zero events and zero expected backgrounds is consistent with less than 2.44 dark matter events at 90% CL. This 90% CL upper limit is used in combination with the differential rate, which is integrated (after Poisson smearing) over the energy range considered to determine

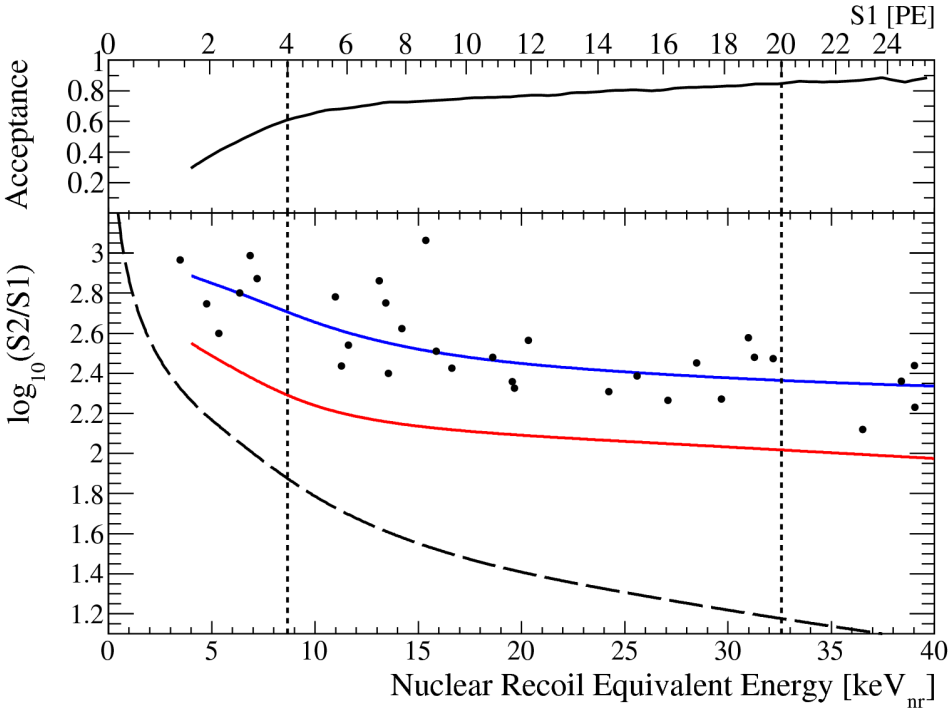

Figure 3.4: Distribution of events in the 40 kg fiducial volume from the 11.17 days data set in $\log_{10}$(S2/S1) vs nuclear recoil energy, along with the energy range for the wimp search (vertical lines). Also shown is the efficiency curve in units of keVr.

the 90% CL upper limit on the cross section.

Figure 3.5 shows the upper limit on the WIMP cross section as a function of WIMP mass derived by this method for the 11.17 day data set [14], along with the most recent limit from the CDMS collaboration [20] and the theoretically predicted region of phase space [37]. Additionally, the 90% CL regions allowed by DAMA [9] and CoGeNT [1] are shown.

The resultant limit from this analysis is comparable to that of CDMS, having slightly higher sensitivity at low WIMP mass, and a minimum of $\sigma < 3 \times 10^{-44}$ cm^2 at 50 GeV/c^2. It is, however, in disagreement with the interpretation that

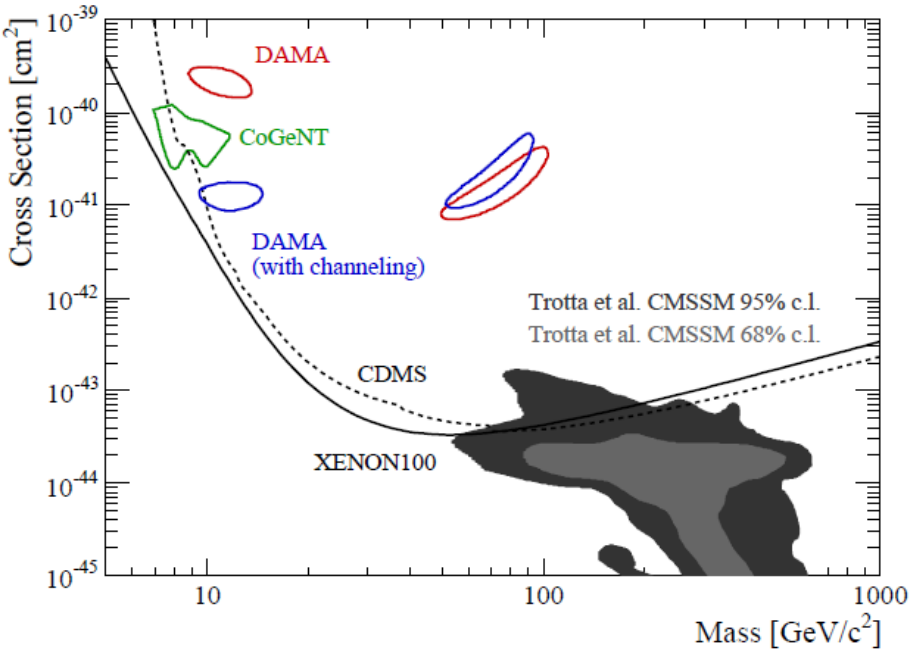

Figure 3.5: 90% CL upper limit on dark matter cross section from the 11.17 day data set in XENON100 [14], with the limit from CDMS [20], theoretically predicted region [37] and the allowed regions from DAMA [9] and CoGeNT [1]

the results of DAMA and GoGeNT are due to low mass WIMPs. This assertion has been challenged by the community [15] [16], as the uncertainty in $\mathcal{L}_{eff}$ has a large impact on the sensitivity to low mass WIMPs. While the XENON100 collaboration stands by these results [13], it is clear that the case of low mass WIMP sensitivity in XENON100 needs careful consideration. The next chapter describes the work done for this thesis that addresses this issue.

CHAPTER 4

Limits on Low Mass WIMPs from XENON100 Based on a Reduced Energy Threshold

In an attempt to address the concerns about the sensitivity of XENON100 to low mass WIMPs, a new analysis was developed, which provides both an increased sensitivity to low energy nuclear recoils and a detailed estimation of the systematic uncertainties. The key deficiency in the standard analysis regarding low mass WIMPs comes from the uncertainty in nuclear quenching factor $\mathcal{L}_{eff}$ and the energy threshold of the detector.

The energy threshold of 4 pe used for the first results of XENON100 was chosen because the efficiency drops quickly below this value. This is dominated by the limitations of detecting low energy S1s, which is due in large part to the light collection and two fold PMT coincidence requirement. In fact, the requirement of an S1 drastically reduces the energy threshold since several photons are necessary to have an S1 of two or more photoelectrons. In contrast, S2s are detectable down to very low energies because the proportional scintillation process generates hundreds of photons per electron, which is sufficient to obtain tens of photoelectrons per electron.

Two methods are explored with the aim of reducing the energy threshold in XENON100 to obtain an increased sensitivity to low mass WIMPs. The first is a simple reduction of the S1 energy threshold compared to the standard analysis,

while carefully accounting for the efficiency and systematic uncertainty introduced by the poor knowledge of $\mathcal{L}_{eff}$. The second eliminates the requirement for an S1, thereby reducing the energy threshold dramatically and avoiding the large systematic uncertainty from $\mathcal{L}_{eff}$. For this purpose, an analysis of only the S2 signal has been developed to achieve an increased sensitivity to low mass WIMPs.

4.1 Low Mass WIMP Interpretation of the DAMA/Libra and CoGeNT Signals

If the signals observed in the DAMA/Libra and CoGeNT experiments are interpreted to be due to WIMP interactions, this would require that the WIMP have a low mass, $m_\chi < 10$ GeV/c^2, and relatively large cross section, $\sigma > 10^{-41}$ cm^2. Figure 4.1 shows the spectrum from the DAMA/Libra data. The steep spectrum at low energies is consistent with a low mass WIMP.

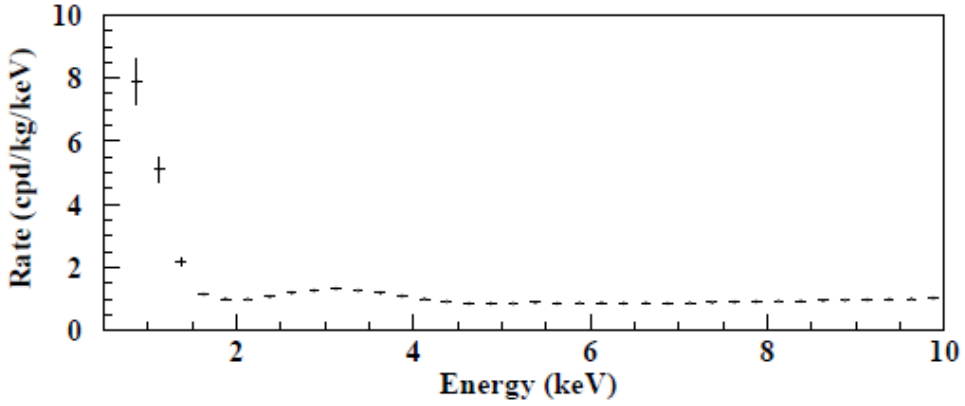

Figure 4.1: Spectrum from DAMA/Libra data [9].

Similarly, the CoGeNT spectrum is peaked at very low energy, as shown in figure 4.2. Also shown in this figure are the spectra for 7 and 10 GeV/c^2 WIMPs. Indeed, the steep spectrum from the data are also quite suggestive of a low mass

WIMP. The 90% CL fit from the data yields a WIMP with a mass between 7 and 11 GeV/c^2.

If the results of DAMA/Libra and CoGeNT are indeed due to low mass WIMPs, XENON100 should also be sensitive to these interactions, even with the limited exposure of the preliminary 11.17 days data. The difficulty lies in reducing the energy threshold sufficiently to obtain a high enough sensitivity to fully test the parameter space that is consistent with the DAMA/Libra and CoGeNT results. Figure 4.3 shows the differential spectra of 7 and 10 GeV/c^2 WIMPs in a xenon target. Both the raw event rate, and the rate smeared by the detector S1 resolution obtained using the global fit for $\mathcal{L}_{eff}$ are shown. The remainder of this chapter addresses the reduction of the energy threshold and the systematic uncertainty of both the energy scale and the energy threshold introduced by the uncertainly of $\mathcal{L}_{eff}$.

4.2 Characterization of Small S2 Signals

4.2.1 Single Electron S2s

As described in chapter 2.2.2, the trigger threshold requires rather large S2s of hundreds of photoelectrons. However, very small S2s are generated by slow decays of the xenon excimers produced in particle interactions that release single electrons that are clearly distinguishable from the original large S2. Thus, by looking at small secondary S2s after the primary S2 that generates the trigger, it is possible to calibrate the detector response to S2s down to the single electron level, and correspondingly measure the S2 light yield, or number of pe per electron.

Single electron S2s look the same, regradless of the depth in the detector where they are generated, since both diffusion and electron capture by electronegative

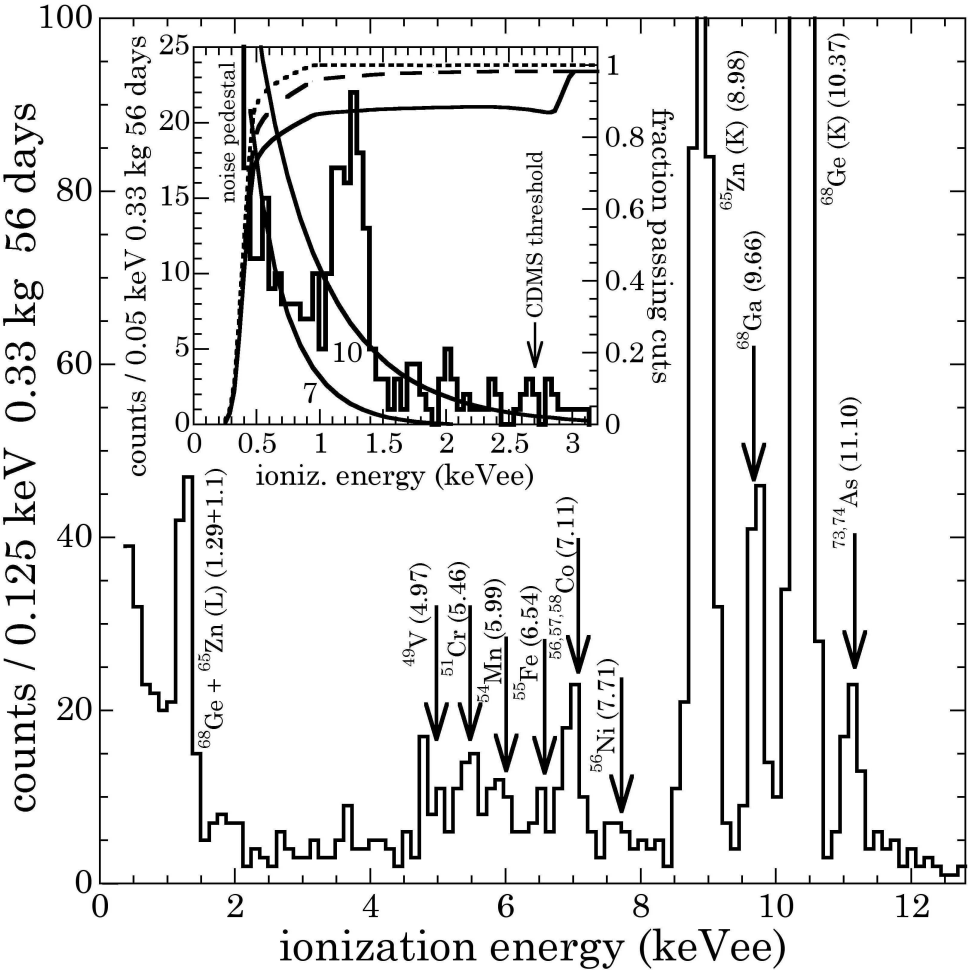

Figure 4.2: Spectrum from CoGeNT data, along with the spectra for 7 GeV/c^2 and 10 GeV/c^2 WIMPs. [1]

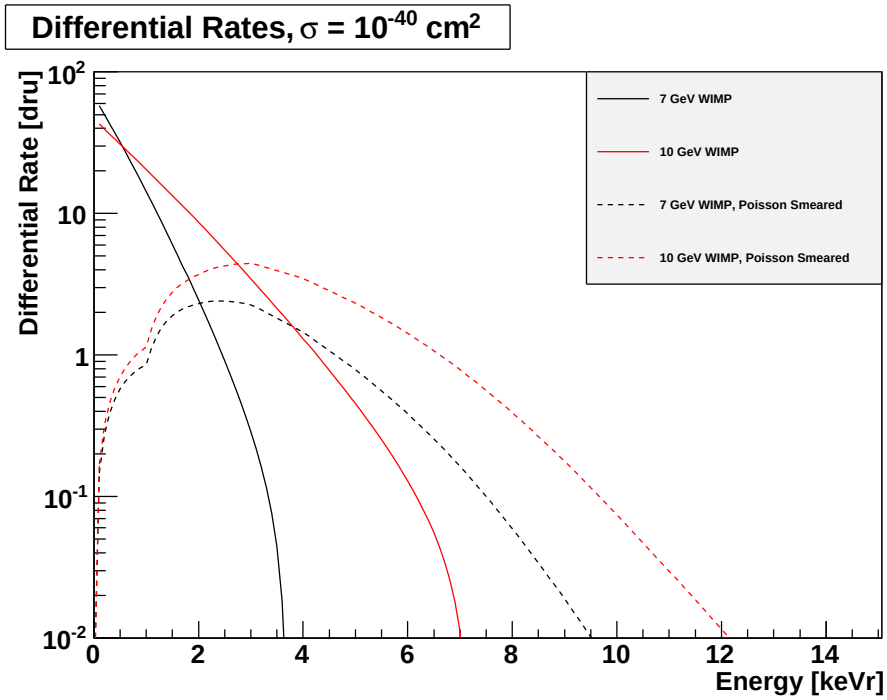

Figure 4.3: Differential Rate in dru (counts/day/keVr/kg) for 7 and 10 GeV/c^2 WIMPs. The dashed curves show the differential rate after including the detector resolution.

impurities are discrete processes. The characteristic signature of an S2 produced by a single electron is several photoelectrons spread over about one μs, the time that the electron takes to drift between the liquid surface and the anode. Figure 4.4 shows examples of such S2s produced by single electrons.

Figure 4.5 shows the spectrum of the lowest energy S2s from the 11.17 day data set, along with a gaussian fit for the one to four photoelectron contributions and a detection efficiency function. The lowest energy S2s are truncated in this spectrum due to the raw data processor's inefficiency in detecting small S2s. This comes from the fact that the processor must distinguish between small S2s and S1s, which becomes difficult at the level of a few pe. The efficiency was modeled

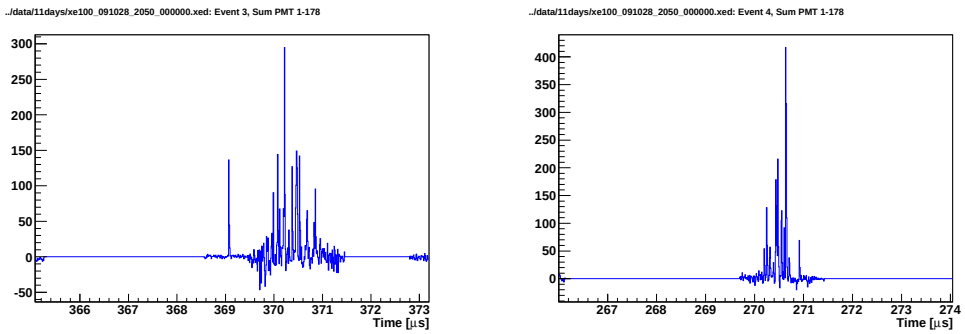

(a) (b)

Figure 4.4: Waveforms of single electron S2s.

using a variety of two parameter functions, each going to zero at zero and one at high S2 values. Additionally, the gaussian fits for the n electron contributions were constrained by the linearity of S2s, i.e. $\mu_n = n\mu_1$, and Poisson fluctuations by $\sigma_n = \sqrt{n}\sigma_1$, but all amplitudes were left as free parameters since the ratio of n to 1 electron events is not known. All fitting functions gave a consistent result of the S2 light yield of $LY_{S2} = 19.4$ pe/electron.

4.2.2 Width Distribution of Small S2s

Diffusion is responsible for the width distribution of S2s as a function of depth in the detector, with the electron cloud of the ionization signal spreading with increased drift length. However, smaller S2 signals are more prone to fluctuations in the size of the spread, since there are fewer electrons involved and statistical fluctuations become more important. Nonetheless, it is possible to obtain information about the Z position of an event from the S2 signal alone by looking at the width of the signal.

Examples of the waveforms of S2s near threshold are shown in figure 4.6. These waveforms also had an S1 present, so the Z position could be measured by

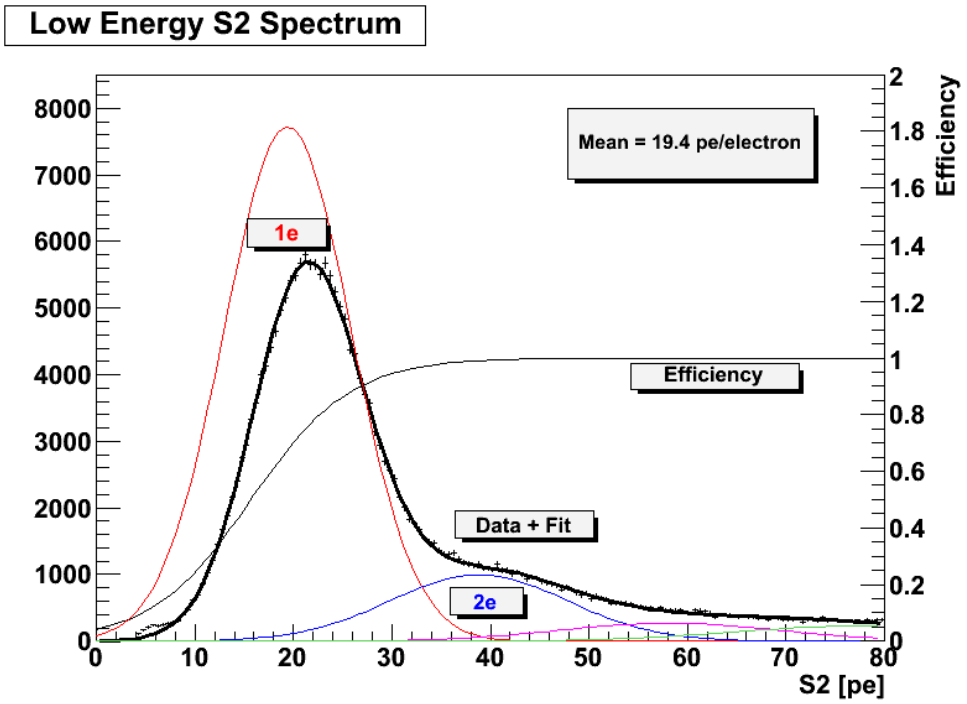

Figure 4.5: Low energy S2 spectrum showing the contribution of 1 and 2 electron events. The fitting algorithm includes the efficiency function that accounts for the raw data processors ability to identify small S2 signals.

the drift time. Figure 4.6(a) shows an S2 from near the top of the detector, while figure 4.6(b) shows one from the bottom portion. Both waveforms have a similar area, but the former is much narrower and higher than the latter, since it is less affected by diffusion.

Instead of using a standard definition for the width of an S2 of the full width at half maximum, a low width was defined as the width between 10% and 90% of the integrated waveform. This width is more sensitive to fluctuations due to diffusion than the full width at half maximum.

Figure 4.7 shows the width distribution for nuclear recoils from the ^{241}AmBe calibration as a function of detector depth for S2s of various sizes. The band is

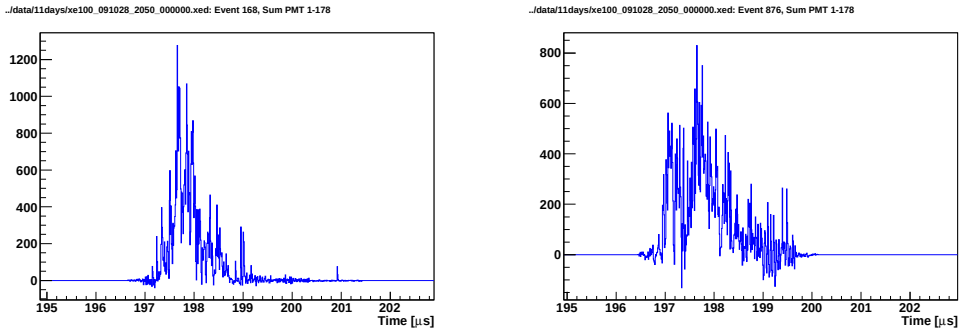

(a) S2 from the top of the detector (b) S2 from the bottom of the detector

Figure 4.6: Waveforms of S2s near threshold from the top and bottom of the detector, showing the difference in width.

tighter at higher energies, as expected, since the statistical fluctuations from the number of electons are reduced for larger S2s.

By defining a cut on the S2 width, an effective cut in Z can be made, although with poor resolution toward the bottom of the detector. Of course, there is an implicit energy dependence to the Z cut as well. Since the Z resolution is poor, around 10 cm at the bottom of the TPC, and is energy dependent, a fiducial volume can be defined by calculating the position and energy dependence of a width cut. The efficiency can then be integrated over the height of the detector and combined with the energy dependent efficiencies of the remaining cuts to determine the final sensitivity. By implementing a width cut between 1.2 and 1.6 μs, figure 4.8 was obtained, which shows the fraction of events that pass this cut as a function of Z for various energies in the range of interest.

Since the x-y position reconstruction is based soley on the S2 hit pattern, a radial cut can still be applied to events with only an S2 signal. Combining a radial cut which discards events outside the central 120 mm with an integration of the width cut efficiency over Z, an effective fiducial volume can be obtained. This was done to obtain a fiducial mass of 15.6 kg for 300 pe S2s, and 14.0 kg for

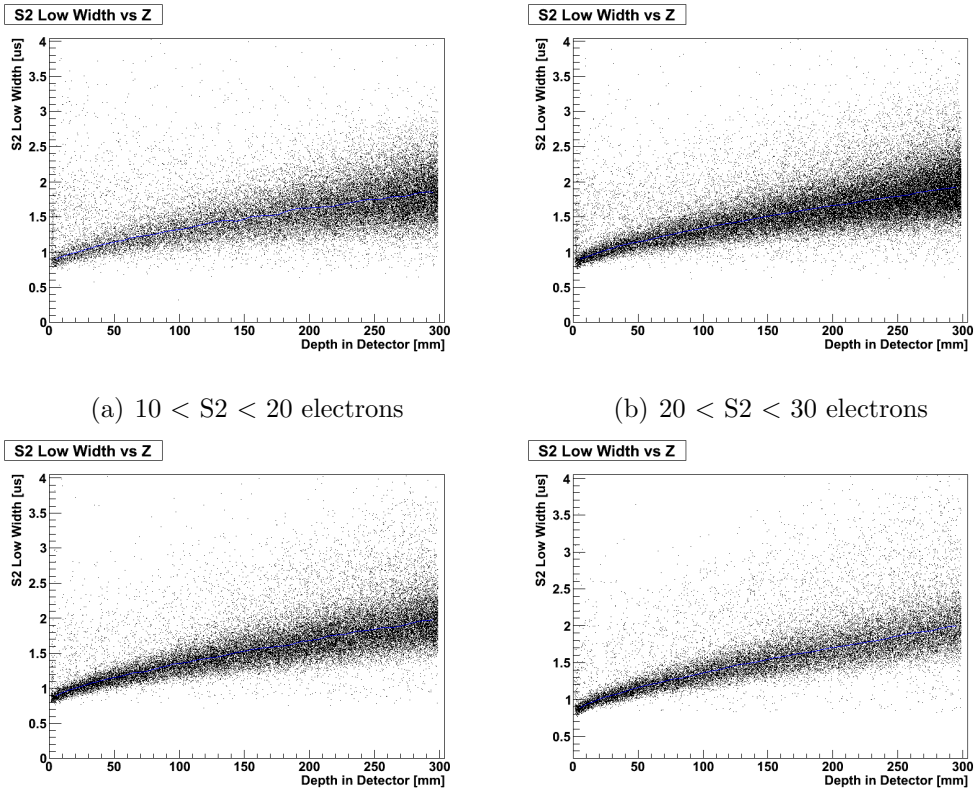

(a) $10 < S2 < 20$ electrons

(b) $20 < S2 < 30$ electrons

(c) $30 < S2 < 40$ electrons

(d) $40 < S2 < 50$ electrons

Figure 4.7: S2 width distributions as a function of detector depth for different energy ranges.

1600 pe S2s. Figure 4.9 shows the fiducial mass as a function of S2. The fiducial volume was intentionally chosen to be small to effectively cut events from both the top and bottom of the TPC, but since the low mass WIMPs that would produce the observed signals in the DAMA/Libra and CoGeNT data would yield a high rate in XENON100, this small volume is still sensitive to such interactions.

A linear conversion from drift time to Z is not entirely correct, as higher order corrections must be made. Additionally, the X-Y position, as found through the position reconstruction algorithms, is based on the position from which electrons are extracted from the liquid. Non-uniformities in the electric field inside the TPC

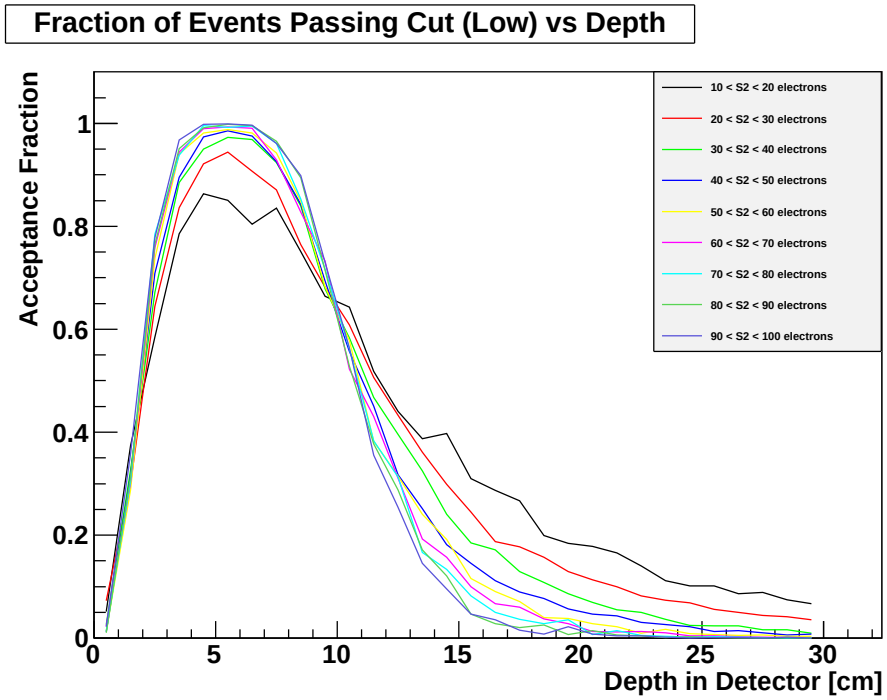

Figure 4.8: Width cut efficiency as a function of detector depth for various energy ranges.

cause electrons to drift along curved paths, which affect the measured values of X, Y and Z. For the standard analysis, a correction map was created that maps the measured location to the physical location of the interaction. Figure 4.10 shows a simulation of the trajectories of drifted electrons in XENON100 that was created for the standard analysis.

Events from the bottom corner of the TPC are reconstructed inward and downward, since they have a longer drift time. Since this is the region where the S2 only Z resolution becomes very poor, it is not possible to accurately create a map to correct these positions. This is the reason for the choise of 120 mm for the radial cut to define the fiducial volume. The S2 width cut used for fiducialization cuts even the lowest energy events by 65% at a depth of 150 mm

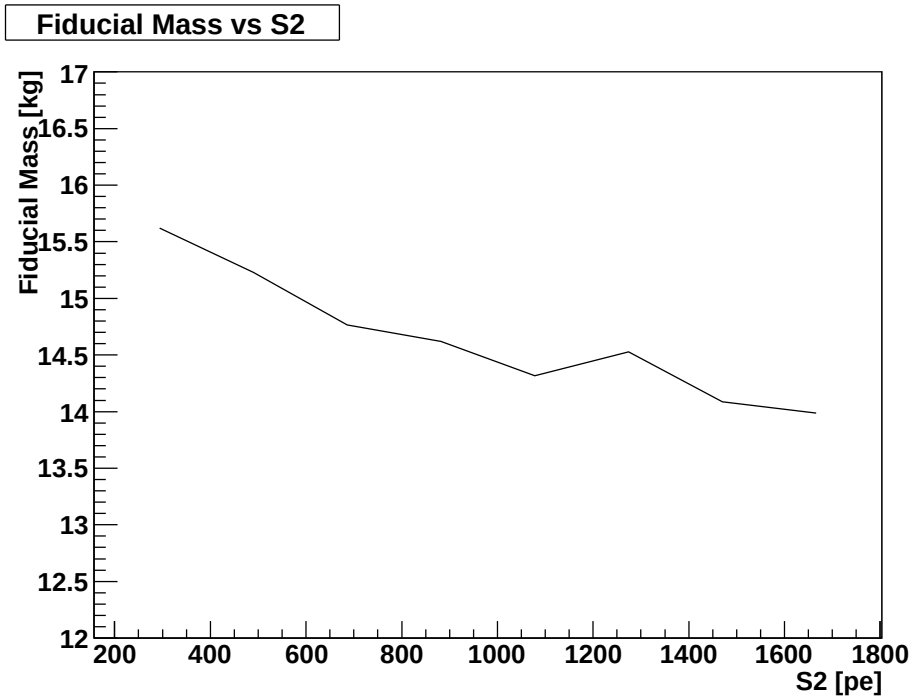

Figure 4.9: Fiducial mass as a function of S2.

4.2.3 Determination of the S2 Energy Scale

The energy scale for S2 signals is not independent of that for S1 signals. In fact, the S2 energy scale is determined by the S2 distribution as a function of S1 energy, so the uncertainty introduced by the choice of $\mathcal{L}_{eff}$ must be accounted for. This is done in section 4.2.4. The S2 energy scale is determined by the ionization yield Q_y, the number of electrons liberated per keV. This is related to the energy by,

$$E = \frac{S2}{Q_y \times LY_{S2}}, \tag{4.1}$$

where LY_{S2} is the S2 light yield determined in section 4.2.1. Unlike the quenching factor $\mathcal{L}_{eff}$, for which the field dependence has been removed, Q_y is a detector dependent quantity, and depends on the applied electric field. It must therefore be determined for each detector to account for the quenching due to the strength

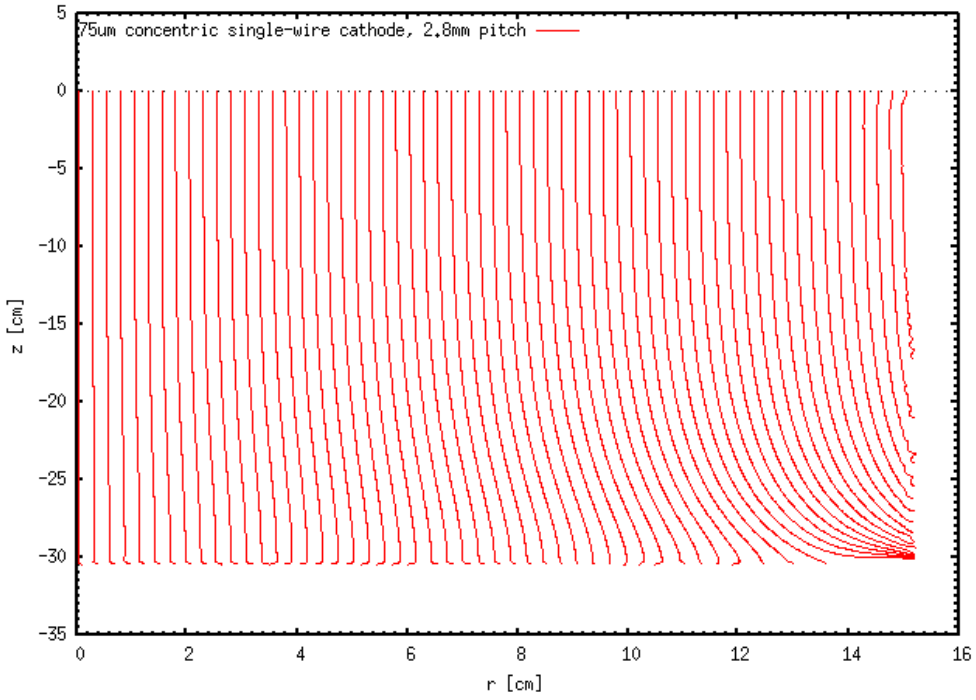

Figure 4.10: Simulated electron trajectories inside XENON100.

of the field of said detector.

The nuclear recoil energy scale, measured in keVr, is determined by the nuclear recoil calibration using an ^{241}AmBe source. At high energies, it is straightforward to calculate Q_y by fitting the S2 distribution at a given S1 energy. At low energies on the other hand, a significant portion of events are below the trigger threshold and the shape of the distribution becomes non-gaussian. Figure 4.11 shows the S2 distributions and fits for 4 and 20 keVr. At 20 keVr, the fit matches the distribution well and Q_y can be accurately determined, but at 4 keVr, even fitting just part of the distribution does not yield a good fit. The resultant values of Q_y as determined by fitting the S2 distributions are shown in figure 4.12. Also shown in this figure is the trigger threshold at the top and bottom of the detector. Events between the two curves are attenuated non-uniformly because

of the trigger threshold.

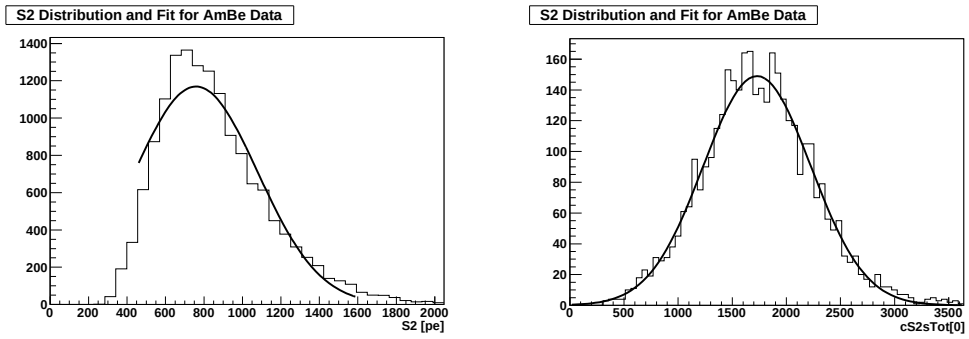

(a) Distribution and fit for 4 keVr.

(b) Distribution and fit for 20 keVr.

Figure 4.11: S2 distributions and fits for ^{241}AmBe data to determine Q_y. At low energy, a the distribution becomes non-Guassian due to the large number of events that are below threshold.

Characterization of the lowest energies for nuclear recoils requires a more sophisticated method that accounts for the signals lost below the trigger threshold. A Monte Carlo simulation was performed that generated S2s uniformly throughout the TPC, then drifted the charge signal to the gas phase, accounting for the attenuation due to electron capture with a random process according to a binomial distribution with a survival probability of $P = exp(-dt/\tau)$, where dt is the drift time and τ is the electron drift lifetime. The ionization signal was then converted into photoelectrons using LY_{S2} and a threshold of 300 pe was applied.

The mean and standard deviation of the generated S2 signal were varied, and the resulting S2 distributions, including the attenuation from the trigger threshold, were compared to the S2 distributions of nuclear recoils from the ^{241}AmBe calibration data, and a χ^2 value was calculated for each. By minimizing χ^2, the best fit for the initial ionization signal was obtained, and this in turn was used to calculate Q_y.

An example of the simulated distribution and the fit to the data is shown in

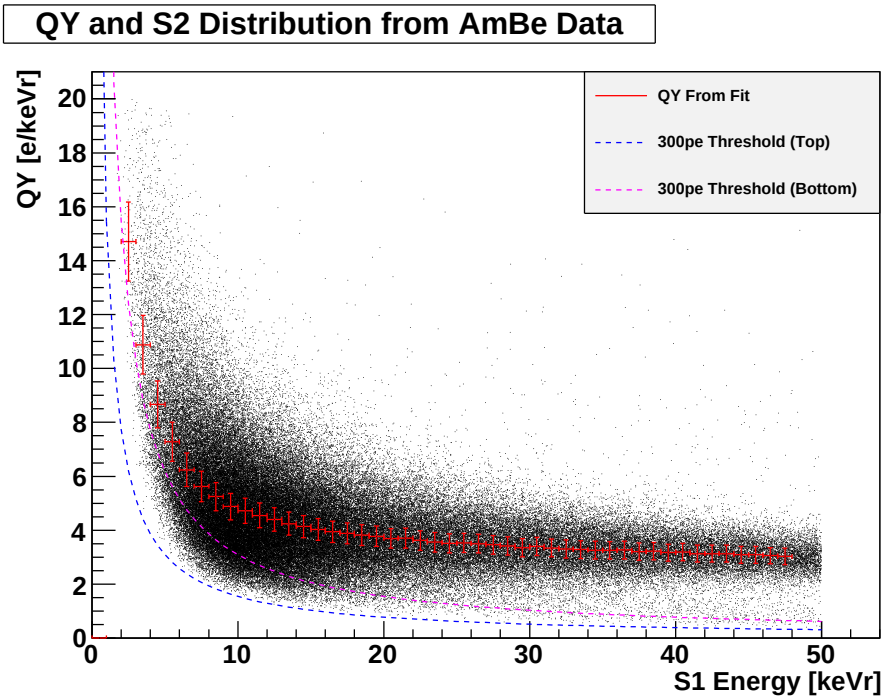

Figure 4.12: Charge yield vs energy for nuclear recoils, as determined from fitting the S2 distribution. The trigger threshold of 300 pe is shown for both the top and bottom of the detector

figure 4.13, which shows the electron lifetime corrected S2 distribution for events between 10 and 11 keVr from both the data and the simulation, as well as the original S2 distribution from the simulation, before the electron lifetime attenuation. Using this method, the left portion of the distribution can be correctly matched, without requiring a fitting function.

The agreement between the ^{241}AmBe neutron data and the Monte Carlo simulation has been explored further by slicing the detector at different depths. Figure 4.14 shows the electron lifetime corrected S2 distribution for two such slices for events with an S1 energy between 10 and 11 keVr. The agreement holds at different depths within the detector, thus validating the model of electron attenuation

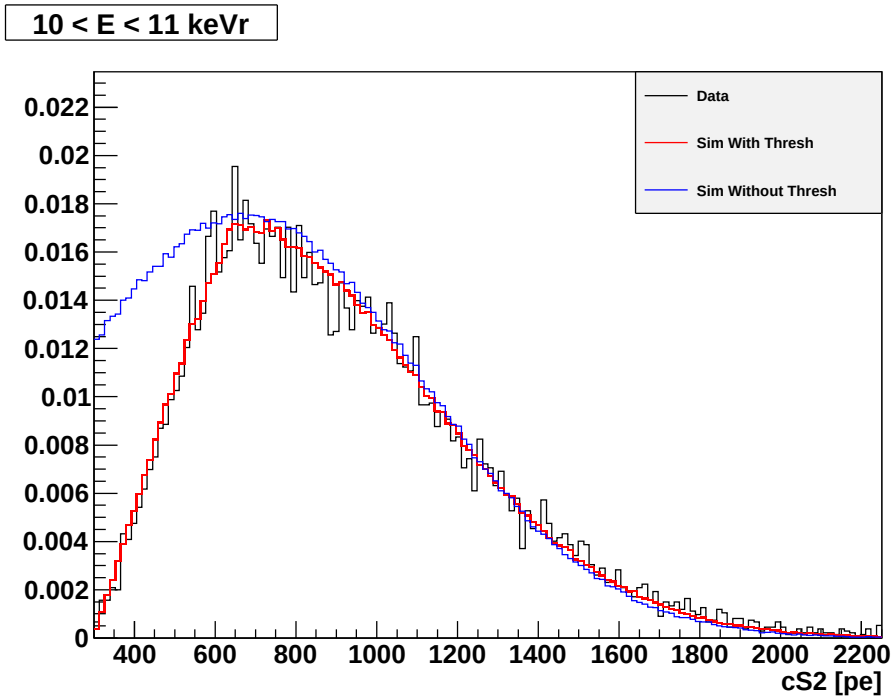

Figure 4.13: Electron lifetime corrected S2 (cS2) distribution from the ^{241}AmBe neutron data and the simulation, both with and without the trigger threshold.

as implemented in the simulation.

Using this method, Q_y can be accurately determined at low energy, where the trigger threshold becomes important. This was done to find Q_y down to 3 keVr. Figure 4.15 shows Q_y as a function of S1 energy as determined by the best fit to the Monte Carlo simulation. At 20 keVr, above which the trigger threshold is not important, both methods agree well, thus validating the behavior the simulation at the high energy limit. Below 20 keVr, Q_y remains flat until 10 keVr where it begins to increase. This is consistent with the fact that the local field is modified by large ionization signals and Q_y should decrease as the energy increases.

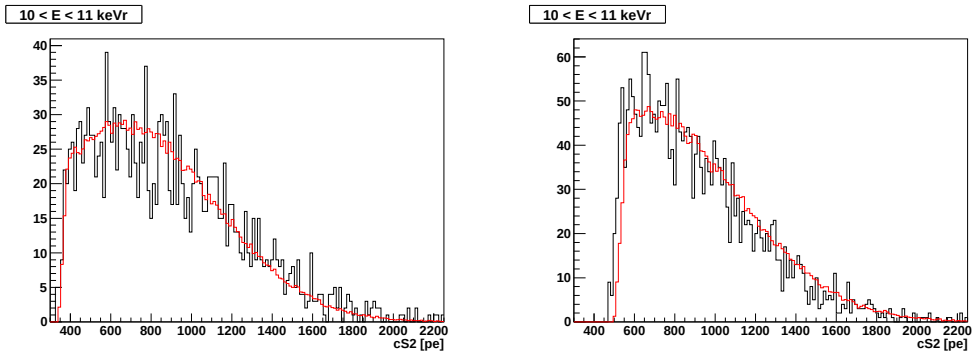

(a) $5 < Z < 10$ cm (b) $20 < Z < 25$ cm

Figure 4.14: Electron lifetime corrected S2 (cS2) distribution for ^{241}AmBe neutron data and the simulation at different depths in the TPC for events between 10 and 11 keVr.

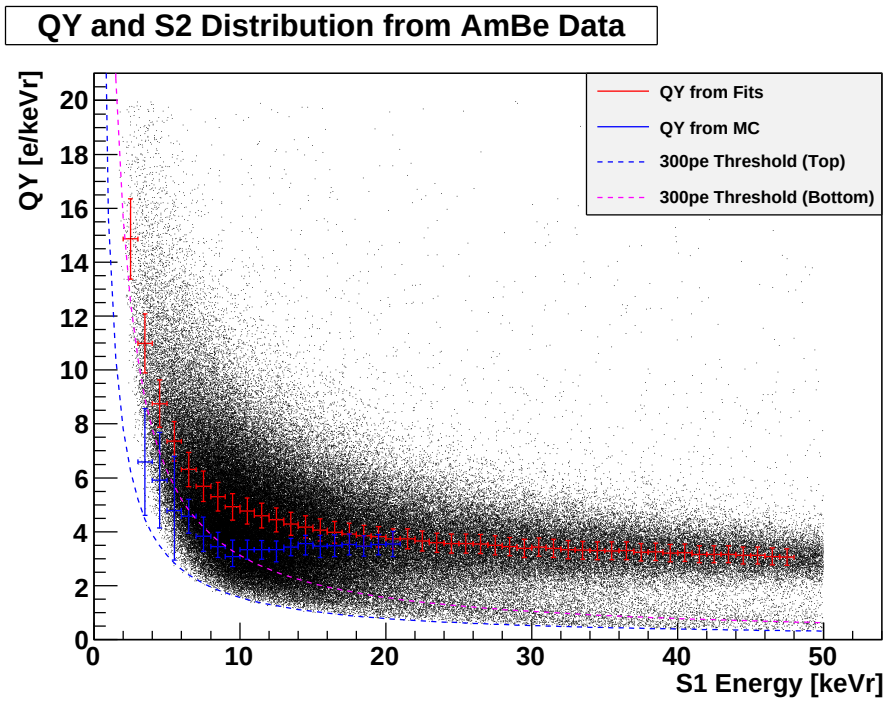

Figure 4.15: Q_y as a function of S1 nuclear recoil energy, determined by both the Gaussian fits to the S2 spectra and comparing to the Monte Carlo simulation.

4.2.4 Estimation of the Systematic Error for Q_y

Determination of the ionization yield Q_y below 3 keVr falls under the same scrutiny as $\mathcal{L}_{eff}$ does, since there is no measurement available. Knowledge of the energy response at the lowest nuclear recoil energy is therefore subject to large systematic uncertainty based on the extrapolation used for both the S1 and S2 energy scales. An estimation of this systematic uncertainty is made here, and is used hereafter in the dark matter search analysis.

The S1 energy scale used for the analysis presented in chapter 3 used a global fit to the measured data for $\mathcal{L}_{eff}$ and a constant extrapolation below 5 keVr. Other extrapolation methods have been suggested where $\mathcal{L}_{eff}$ goes to zero at or above 0 keVr [34] [15]. Three different fits for $\mathcal{L}_{eff}$ are considered here, the global fit with a constant extrapolation below 5 keVr used in the standard analysis, the global fit with a linear extrapolation to zero at 0 keVr, and the lower 90% CL contour from the global fit, with a logarithmic extrapolation to zero at 1 keVr. Figure 4.16 shows the different fits considered.

The same method for determining Q_y at low energies was implemented for the different fits to $\mathcal{L}_{eff}$. The same Monte Carlo was used, but the S2 spectra were different due to the different S1 energy scale. Figure 4.17 shows the resultant values of Q_y. The results are almost identical for the different extrapolataions of the global fit, and there is a slight difference for the lower 90% CL fit. Note that Q_y cannot be determined to as low a value for the different fits due to the decrease in statistics at low energy with the different S1 energy scale.

Since all of the fits give a very similar value for Q_y, the systematics of $\mathcal{L}_{eff}$ do not contribute significantly to the error in calculating the sensitivity of XENON100. However, the two extreme cases, the global fit and the lower 90% CL fit, are both considered in the analysis that follows, and the consistency of

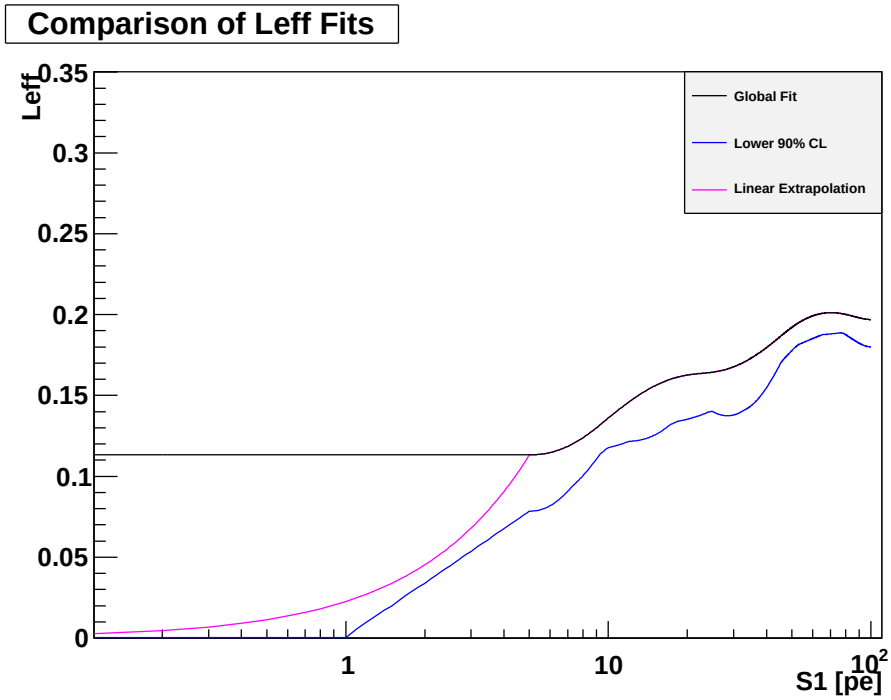

Figure 4.16: Different fits considered for $\mathcal{L}_{eff}$.

the results is checked.

4.2.5 Resolution of S2 Energy Scale

The resolution for the S2 energy scale comes from fluctuations in both the number of electrons extracted from the liquid and fluctuations in the number of photoelectrons collected per electron. An additional contribution to the resolution comes from the electron lifetime correction. The resolution can be estimated by the S2 distributions obtained by the Monte Carlo simulation used in the determination of Q_y, which contains all three processes. The width of the raw S2 signal is a good estimation of the fluctuation in the signal before the detector efficiency.

Figure 4.18 shows the resolution obtained by this method as a function of S2. Below 3 keVr, the S2 resolution is extrapolated based on a 1/E dependence. This

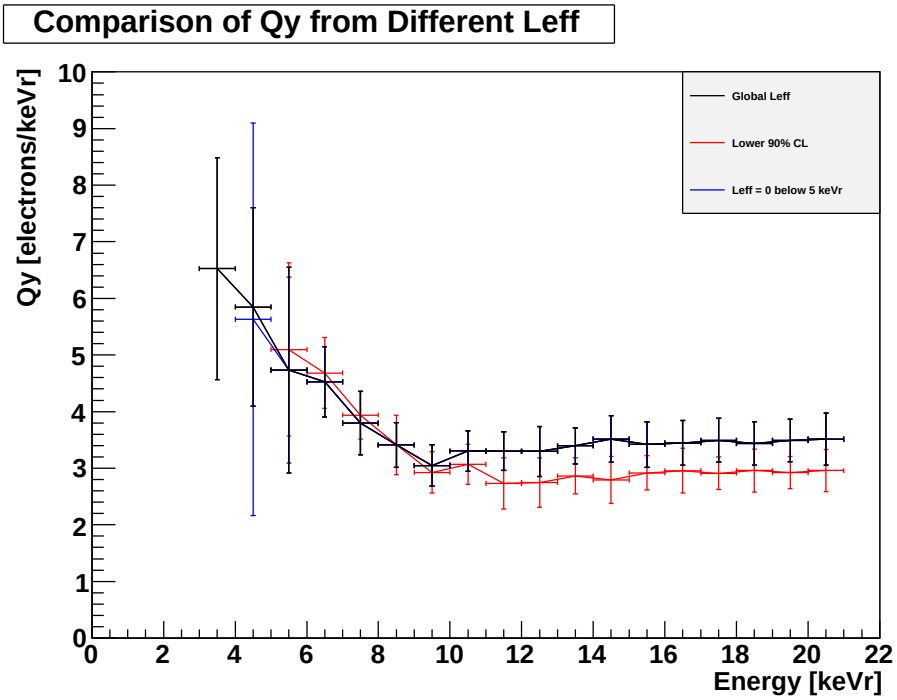

Figure 4.17: Q_y as determined by different fits for $\mathcal{L}_{eff}$.

resolution is used to determine the expected WIMP signal in the detector.

4.2.6 Detector Efficiency for S2 Only Analysis

4.2.6.1 Description of Cuts

The data quality cuts used for the S2 only analysis are similar to those used in the standard analysis. Events were separated into two categories, those with valid S1s and those with no valid S1.

Events were considered to have a valid S1 if they passed all of the cuts developed for the standard analysis presented in section 3.1.1, with the exception of the fiducial cut and the S2/S1 cut.

Most of the data quality cuts used for the standard analysis do not explicitly

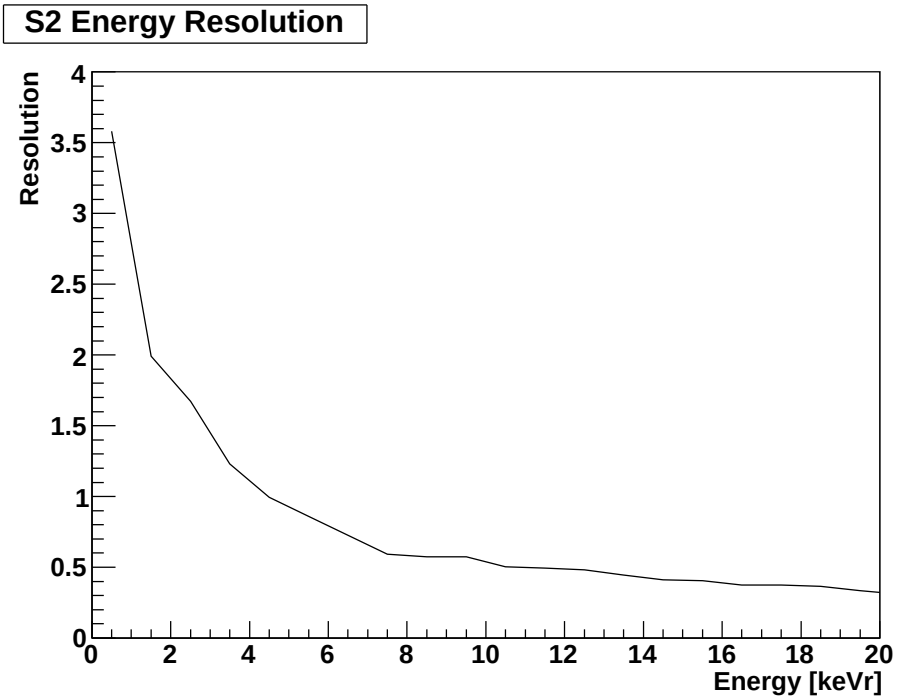

Figure 4.18: S2 energy resolution as a function of S2.

require an S1. For events without a valid S1, these cuts remained unchanged. The remaining cuts that do require an S1, such as the two-fold coincidence cut and the active veto cut, were removed. The effect on the efficiency is described in section 4.2.6.2.

The fiducial cut used for this analysis, as described in section 4.2.2, is a radial cut at 120 mm and a cut in the S2 width below 1.2 μs and above 1.6 μs. One additional cut was applied to events with an S1, for which the Z position can be well determined. A hard fiducial cut was applied 10 mm from the top and 50 mm from the bottom of the TPC. This was done to explicitly cut leakage events at the top and bottom of the detector that happen to have an S1. Since the acceptance of the S2 width cut in this region is low, and since the low energy spectrum is dominated by events without an S1, it should not have a large impact

on the fiducialization. But in this way, the leakage events from the surface of the detector can be minimized.

4.2.6.2 Cut Efficiencies

For the S2 only analysis, there are too few cuts to follow the procedure used in the standard analysis to estimate the cut efficiencies, making it difficult to define a set of good nuclear recoil scatter events. Instead of trying to explicitly estimate the cut efficiency for the S2 only analysis, the relaxation of the S1 requirement is assumed to leave the cut efficiency very high.

This assumption is justified by the comparison of the nuclear recoil spectrum with and without an S1 requirement. The nuclear recoil S2 spectrum was obtained from the ^{241}AmBe calibration data set, and is shown in figure 4.19. The sensitivity begins to increase at a few tens of keVr and remains high at low energy where the S1 sensitivity rolls off due to photo statistics. The rate goes to zero at 3 keVr due to the S2 trigger efficiency.

The S2 trigger probability was measured to be very near 100% above 280 pe, and decreases to zero below 160 pe. However, the volume averaged trigger efficiency is more complicated because the attenuation of S2s from the electron drift lifetime gives deeper parts of the TPC a higher threshold.

The mean behavior of the electron lifetime attenuation follows an exponential decay,

$$S2(t) = S2(0) \times exp(-t/\tau), \tag{4.2}$$

where t is the drift time and τ is the electron lifetime. Equation 4.2 can be used to model the affect of the electron lifetime on the trigger efficiency, namely by,

$$\epsilon(S2) = \int_0^{t_{max}} T\left(S2 \times exp(-t/\tau)\right) F(t)dt \Big/ \int_0^{t_{max}} T(S2)F(t)dt, \tag{4.3}$$

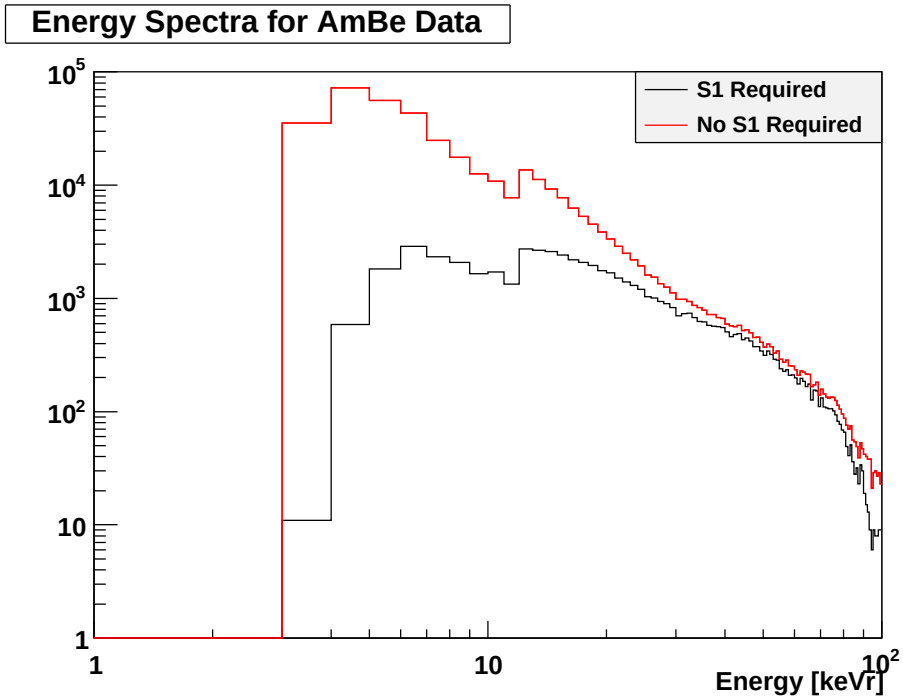

Figure 4.19: S2 spectrum for ^{241}AmBe calibration data, with and without an S1 required.

where $T(S2)$ is the S2 trigger probability, t is the drift time integrated from 0 to the maximum drift time, τ is the electron lifetime, and $F(t)$ is the fiducial volume acceptance as a function of drift time.

Figure 4.20 shows the resultant trigger efficiency as a function of S2. The efficiency rises steeply and reaches 100% at around 600 pe.

4.2.7 WIMP Signal for S2 Only Analysis

Combining the efficiency curve and the energy resolution with the differential rate from equation 1.3.1, the expected WIMP signal for the S2 only signal can be obtained. Figure 4.21 shows this signal for 7 and 10 GeV/c^2 WIMPs with a 10^{-40} cm^2 cross section, the same case considered for the S1 energy scale in section 4.1.

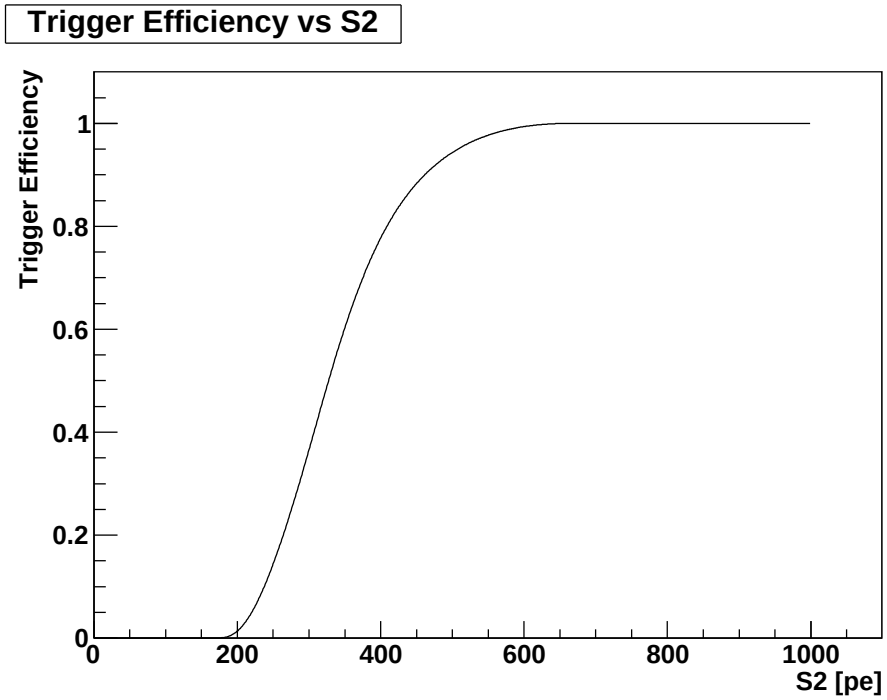

Figure 4.20: Trigger efficiency in the fidicual volume as a function of S2

4.3 Reduction of the S1 Energy Threshold

Another approach to the reduction of the energy threshold is to simply consider the S1 energy scale down to lower values. By properly accounting for the efficiency, this can similarly give an increased sensitivity to low mass WIMPs. This approach is also considered here as an independent approach to a search for low mass WIMPs that are compatible with the DAMA/Libra and CoGeNT claims.

4.3.1 Trigger Efficiency as a function of S1

The majority of the analysis was already developed, and presented in chapter 3. One important difference to that analysis is the effect of the trigger efficiency. The trigger efficiency presented in section 4.2.6.2 can be modified slightly to find

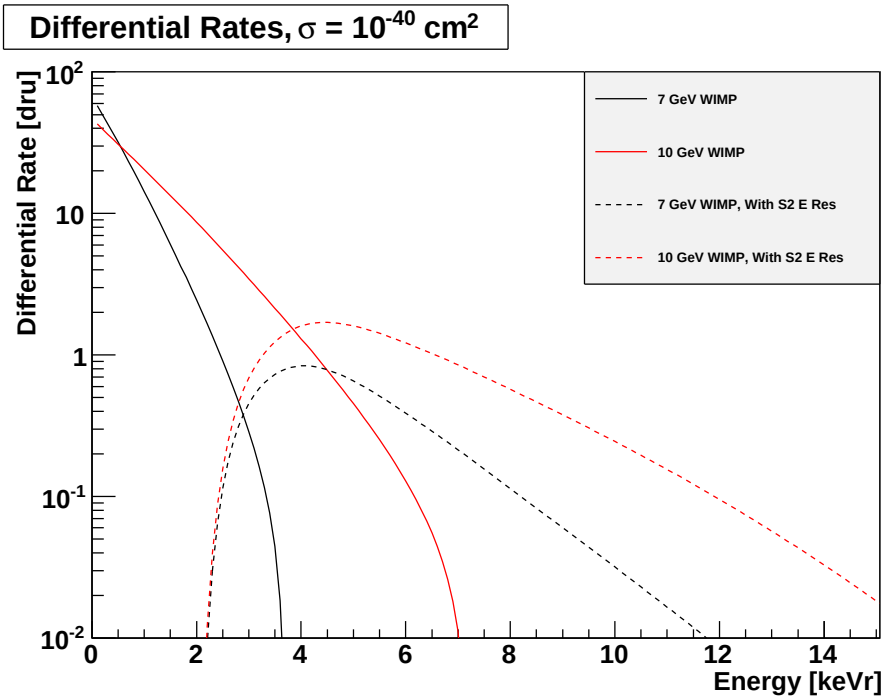

Figure 4.21: Differential rate for S2 only analysis including the energy resolution and efficiency.

the trigger efficiency as a function of S1. The efficiency at a given S2 value must be smeared to an S1 axis to account for the fluctuations in S1. The S2 distributions obtained from the Monte Carlo simulation for determining Q_y were used to smear the efficiency to an S1 axis, as shown in figure 4.22. The trigger efficiency implicitly includes the fiducial volume cut, so the 40 kg fiducial volume cut was used in this calculation. Additionally, the efficiency depends on the electron lifetime, as is shown in the figure.

The trigger efficiency has a non-negligible effect on the standard analysis, as it reaches 100% near the upper end of the energy range used, and is around 50% at the low energy threshold. In the following analysis, the sensitivity is calculated with the trigger efficiency included, as well as different energy thresholds.

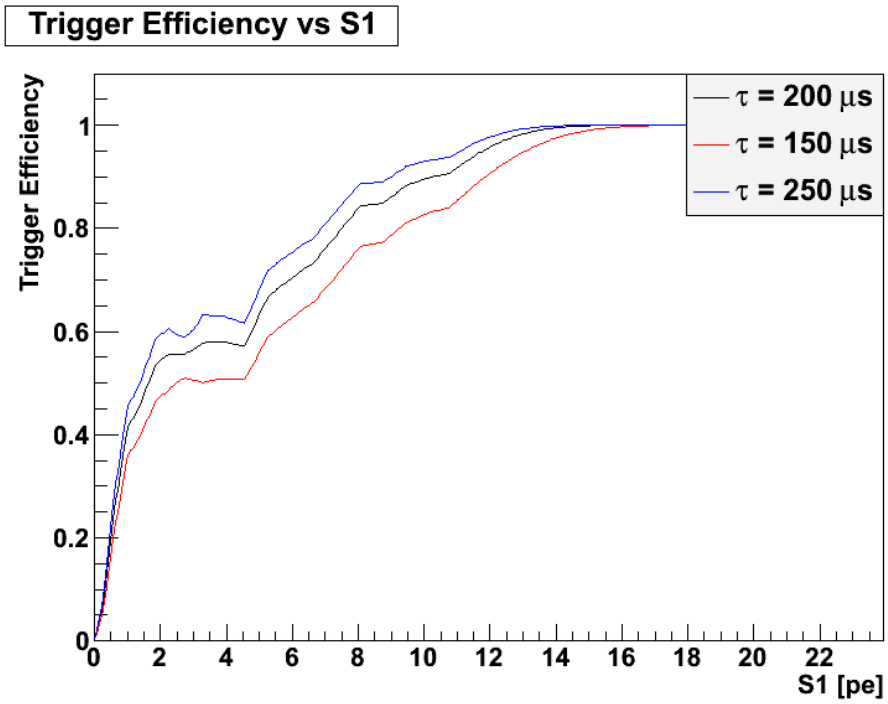

Figure 4.22: Trigger efficiency as a function of S1 for different electron lifetimes.

Since the trigger efficiency affects all data, including calibrations, the efficiencies estimated for the standard analysis are after the trigger efficiency. The total efficiency is then simply the product of the efficiency curve shown in figure 3.2 and the trigger efficiency.

4.3.2 Systematics of $\mathcal{L}_{eff}$

Like in the study of the systematics for Q_y, the systematics of different $\mathcal{L}_{eff}$ fits are studied for the standard analysis. The same three cases are considered, and the results of the analysis are compared for these cases.

4.3.3 WIMP Signal for the Standard Analysis

By incorporating the total efficiency, including the trigger efficiency, the expected WIMP spectra can be found. Figure 4.23 shows the spectra after the S1 resolution from Poisson fluctuations and the total efficiency have been applied for a 7 and 10 GeV/c^2 WIMP and a 10^{-40} cm^2 cross section.

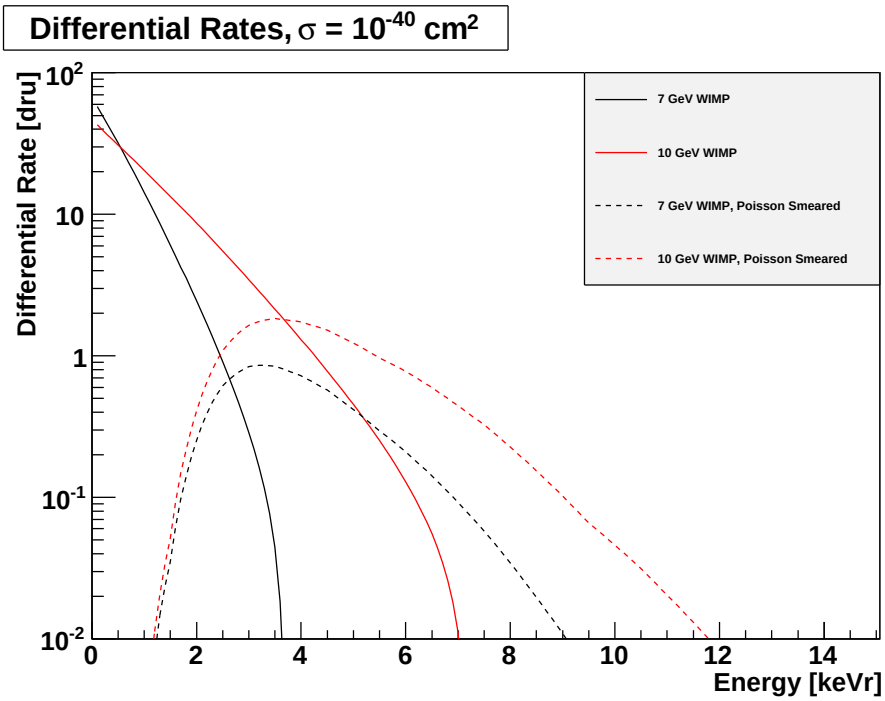

Figure 4.23: Expected spectra in S1 energy for 7 and 10 GeV/c^2 WIMPs with a 10^{-40} cm^2 cross section after the detector S1 resolution and efficiency have been applied.

4.4 Limits on Low Mass Dark Matter

An analysis was performed on the 11.17 days data set used for the first results of the standard analysis in order to improve the sensitivity to low mass WIMPs.

Two analysis methods were employed to reduce the energy threshold. The first is based on an analysis of only the S2 signal, and the second is based on the standard analysis with a more accurate estimation of the efficiency and a reduced energy threshold. The results of the two analyses are each compared to the CoGeNT and DAMA signals and to one another for consistency.

4.4.1 Energy Window

In the case of a background limited search, such as the S2 only analysis, a better sensitivity can be obtained by optimizing the energy window to maximize the signal to noise. For the S2 only analysis, the definition of the energy window for the WIMP search was selected as a function of WIMP mass. Instead of using a fixed window for all WIMP masses, a different optimized window was found for each mass separately. The upper bound was selected based on where the WIMP rate for a given WIMP mass decreased by an order of magnitude relative to the maximum rate. Figure 4.24 shows the upper bound selected as a function of WIMP mass, with an upper bound of 3.8 keVr for a WIMP mass of 5 GeV/c^2 and an upper bound of 14 keVr at 15 GeV/c^2. Since this analysis is primarily sensitive to low mass WIMPs, the optimization was only caried out for WIMP masses below 15 GeV/c^2. For heavier WIMPs, the upper energy bound was set to 14 keVr.

Instead of introducing a low energy bound, all signals are used, and the trigger efficiency attenuates the expected signal to zero at around 3 keVr. Thus, the low energy bound is effectively at 3 keVr, although it is not explicitly implemented.

For the standard analysis, this is not necessary, since there are no backgrounds present. For this analysis, the upper bound of the energy window was fixed to 20 pe, or 32.6 keVr. Three different lower bounds were considered. The first is

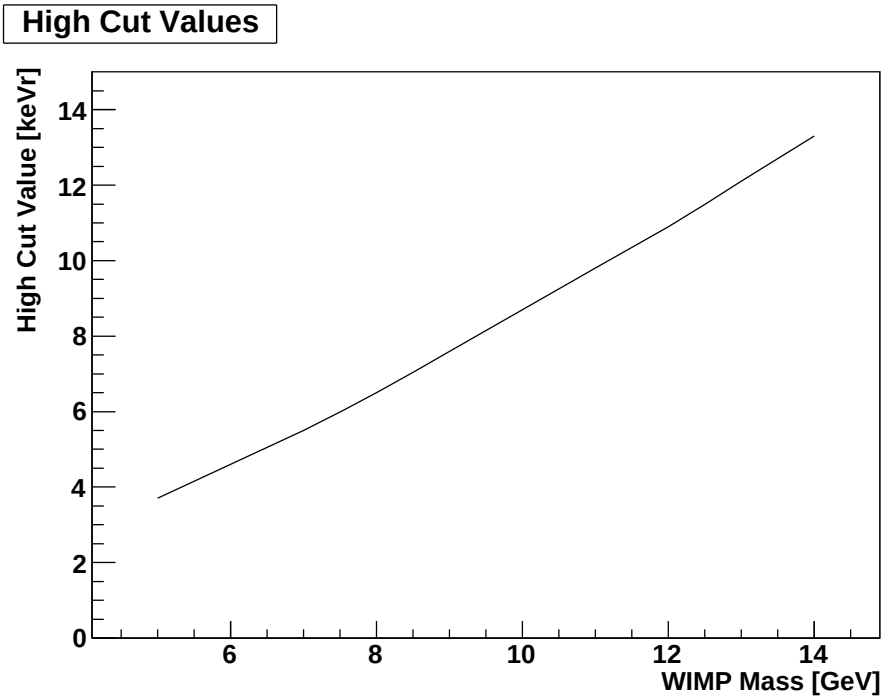

Figure 4.24: Upper energy bound as a function of WIMP mass for different lower energy bounds.

at 4 pe, or 8.67 keVr, to compare the results with those from the first analysis that does not include the trigger efficiency. The other two lower bounds are at 3 pe and 2 pe, or 7.02 and 4.90 keVr.

4.4.2 Event Distribution for WIMP Search

The data for the 11.17 day WIMP search were used to find the S2 energy spectrum, as shown in figure 4.25. Within the fiducial volume, there are 90 events below 14 keVr, but only 5 in the smallest energy window below 3.8 keVr.

The spatial distribution of the events for the S2 only analysis is shown in figure 4.26. The fiducial volume is marked by the blue box. For events with an S1, Z is determined by the drift time, while those without an S1 have a Z determined

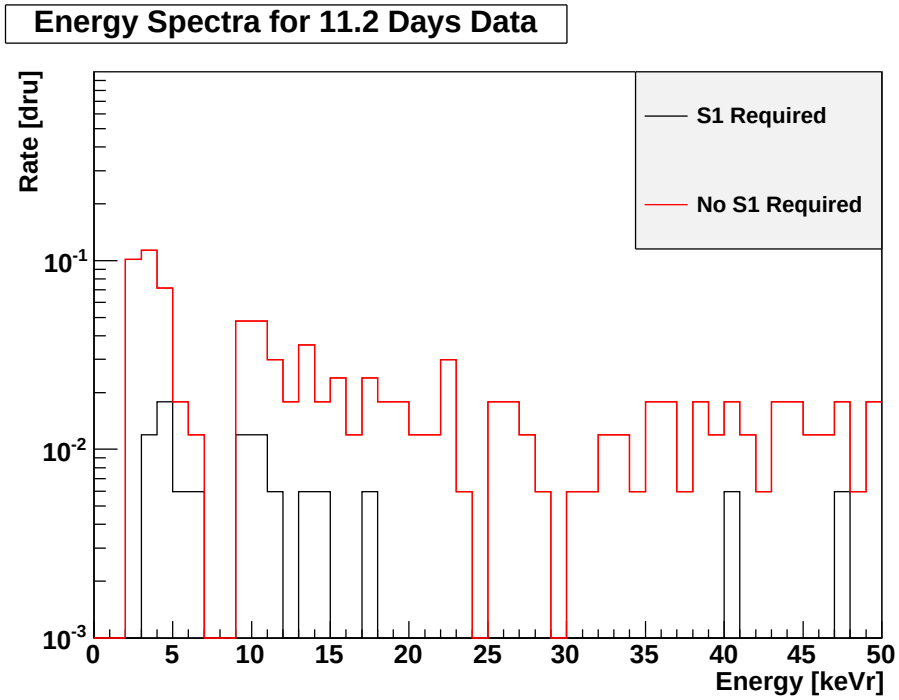

Figure 4.25: S2 energy spectrum for the 11.2 day WIMP search.

from the S2 width. Although there are a rather large number of events in the S2 only analysis, at least a portion is likely due to the electron recoil background, and will be addressed in section 4.4.3.

For the standard analysis, the only change is the efficiency and the energy threshold, so the event distribution is the same as that shown in figures 3.3 and 3.4. There are still no WIMP candidate events below the nuclear recoil median, so only an upper limit on the WIMP cross section can be set in the following analysis based on a background free search.

4.4.3 Background Subtraction for the S2 Only Analysis

Since electron recoil events with an S1 can be discriminated by the $\log_{10}(S2/S1)$, this information can be used to estimate the electron recoil background for the

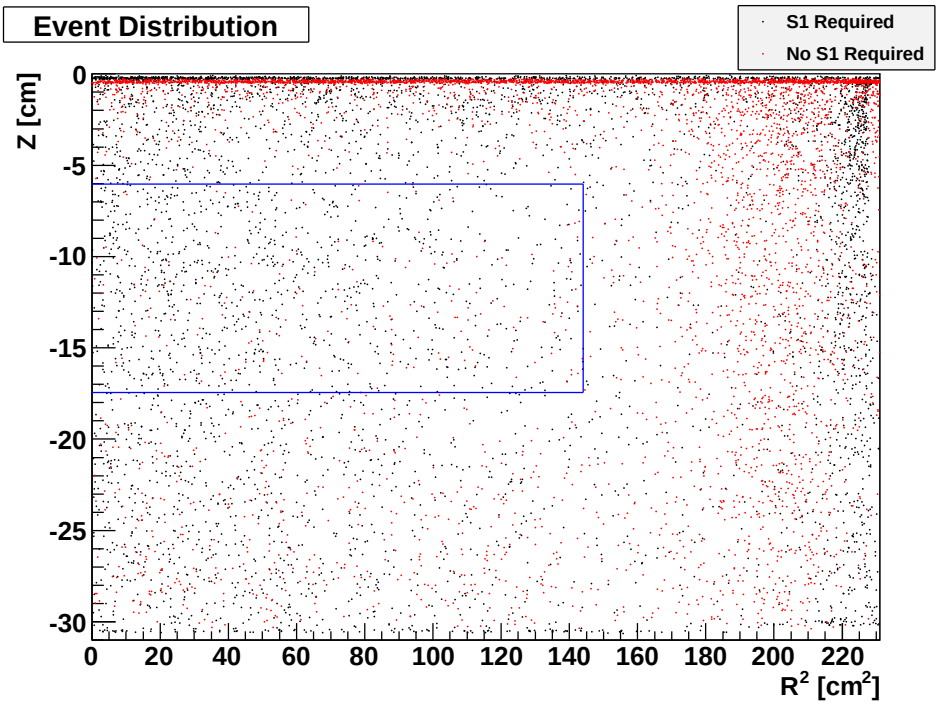

Figure 4.26: Spatial distribution of the events in the 11.2 day WIMP search.

S2 only signal. Using the electron recoil calibration with ^{60}Co, the ratio of the rate of events with an S1 and without an S1 can be used in combination with the observed rate of events with an S1 in the dark matter search data set to estimate the electron recoil rate for events without an S1.

Figure 4.27 shows the S2 spectrum for electron recoils as a function of nuclear recoil energy from the ^{60}Co calibration for all events and those with an S1. The ratio of all events to those with an S1 is shown as a function of energy in figure 4.28. The binning in these histograms is large because of the low statistics both in the ^{60}Co calibration and in the dark matter search data.

The expected event rate for all events can be estimated by multiplying the rate of events with an S1 by the ratio from the ^{60}Co calibration. This has been done to obtain figure 4.29. Below 15 keVr, in the energy range of interest, the expected

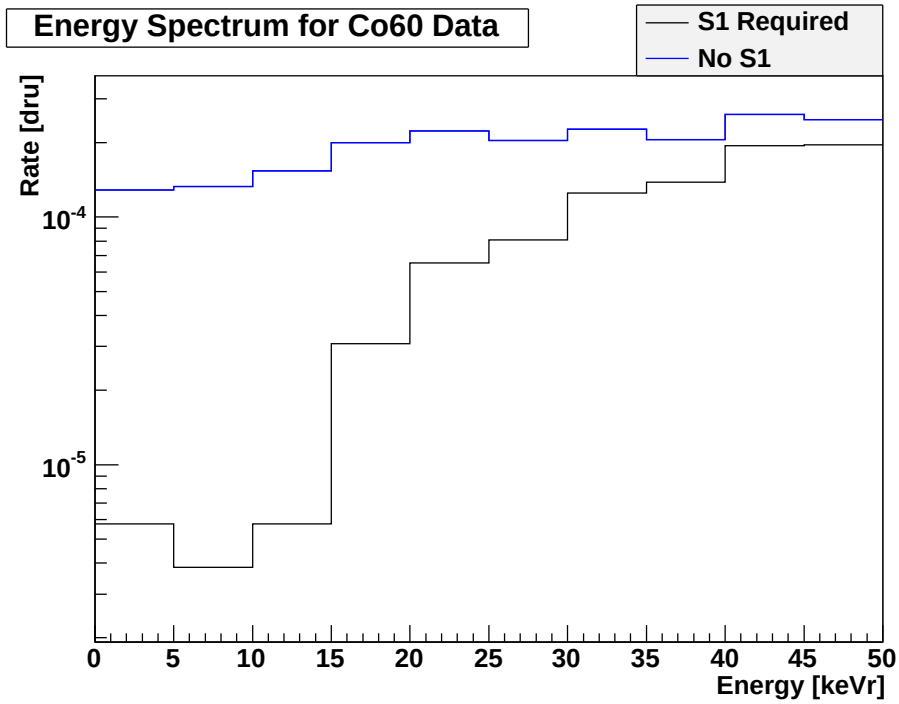

Figure 4.27: Electron recoil spectrum for all events and those with an S1 for the ^{60}Co spectrum.

electron recoil rate exceeds the observed rate. Thus, the 90 events observed are consistent with an electron recoil background.

A background subtraction was implemented by considering all observed events to be consistent with background. Since the variable energy window has much finer resolution than the histogram for the expected number of backgrounds, the expected background was set to the number of observed events. This is a conservative estimate, because the actual background rate is higher, so this will in turn lead to a conservative calculation for the cross section upper limit.

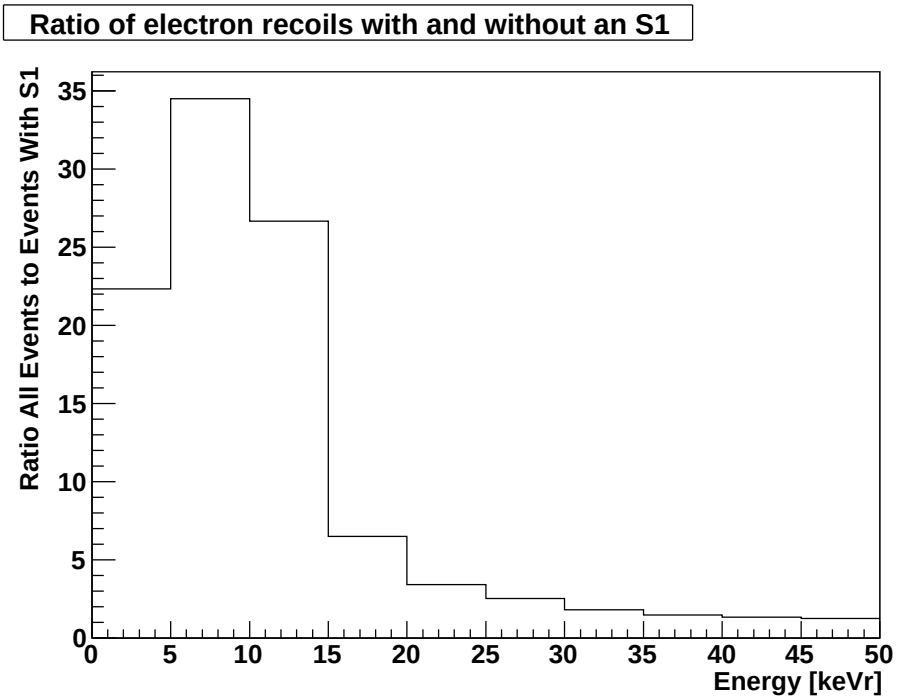

Figure 4.28: Ratio of all electron recoil events to those with an S1 for the ^{60}Co calibration.

4.4.4 Limits on WIMP Cross Section

Since the observed events in the S2 only analysis are consistent with background events, and since no events were observed for the standard analysis, no discovery claim can be made. However, an upper limit can be set on the WIMP-nucleon cross section for each analysis. Of particular interest is the comparison of these upper limits with the signals observed in the DAMA/Libra and CoGeNT experiments.

For the S2 only analysis, the limit is derived for two cases. The first considers all events as WIMP candidates, but is very conservative, since the observed events are consistent with an electron recoil background. The second implements background subtraction. For both cases, the two extreme fits for Q_y are used,

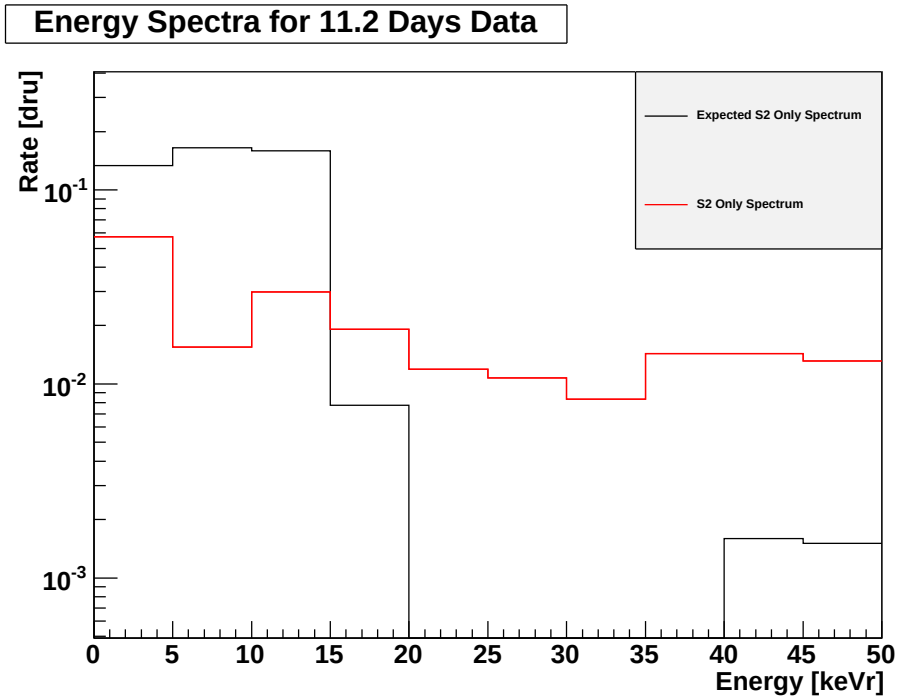

Figure 4.29: Expected electron recoil rate and observed rate as a function of nuclear recoil energy for the dark matter data.

both the global fit and the lower 90% CL fit. Figure 4.30 shows the derived limits for these cases as a function of WIMP mass. Also shown are the published limit from the XENON100 first results [14], and the recent results from a low mass WIMP analysis by CDMS [2].

A zoomed view of the low mass portion of the exclusion curves is shown in figure 4.31.

The limits from the S2 only analysis completely exclude the allowed regions from DAMA/Libra and CoGeNT, even for the most conservative case.

For the standard analysis with reduced energy threshold, the upper limit on the WIMP-nucleon cross section was calculated for the three fits to $\mathcal{L}_{eff}$, and for an energy threshold at 4, 3, and 2 pe. Figure 4.32 shows these limits, along with

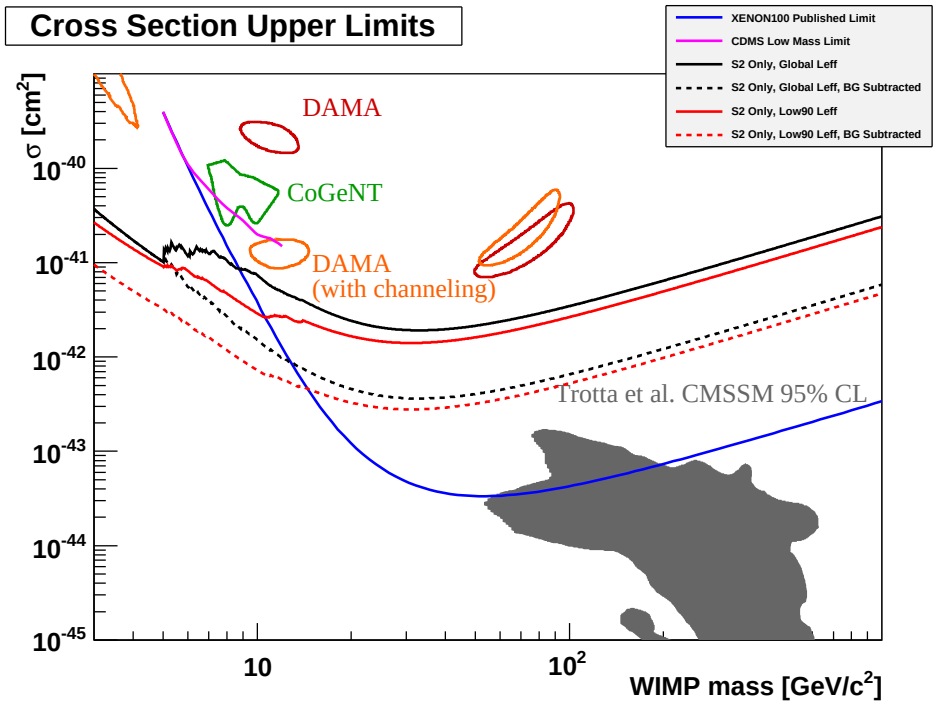

Figure 4.30: Upper limits on the WIMP-nucleon cross section for the S2 only analysis, along with results from CDMS and the acceptance regions for DAMA/Libra and CoGeNT.

the published results from XENON100 and the CDMS low energy analysis, the contours for DAMA/Libra and CoGeNT, and the theoretically predicted region. A zoomed view of the low mass portion is shown in figure 4.33. The 4 pe threshold is shown to demonstrate the shift in the limit due to consideration of the trigger efficiency. Accounting for the trigger efficiency raises the upper limit slightly at all WIMP masses.

At a threshold of 2 pe, the entire phase space of DAMA/Libra and CoGeNT is excluded for the global fit and constant extrapolation of $\mathcal{L}_{eff}$. For all choices of $\mathcal{L}_{eff}$, all but the lowest mass region for DAMA/Libra including ion channeling is excluded.

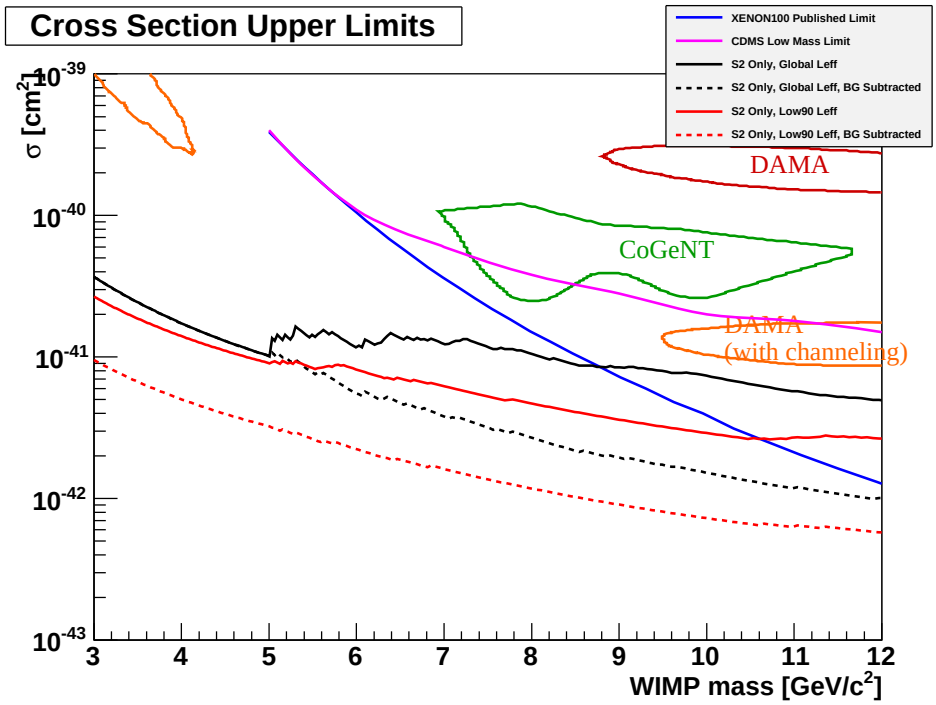

Figure 4.31: Zoomed view of the low mass region for the limit curves from the S2 only analysis.

4.5 Summary and Discussion

In conclusion, both analyses are in agreement with one another, and with the results of the CDMS low energy analysis. However, they are not consistent with the interpretation of the DAMA/Libra and CoGeNT signals as WIMP interactions. The case of no ion channeling in DAMA/Libra is ruled out by both the S2 only analysis and the 2 pe threshold in the standard analysis with all considerations of Q_y and $\mathcal{L}_{eff}$. When ion channeling is allowed in DAMA/Libra, the regions consistent with a WIMP interaction are still excluded by the S2 only analysis and the standard analysis with a 2 pe threshold and the global fit with constant extrapolation for $\mathcal{L}_{eff}$. The results of this analysis suggest that the signals in DAMA/Libra and CoGeNT are not due to WIMP interactions.

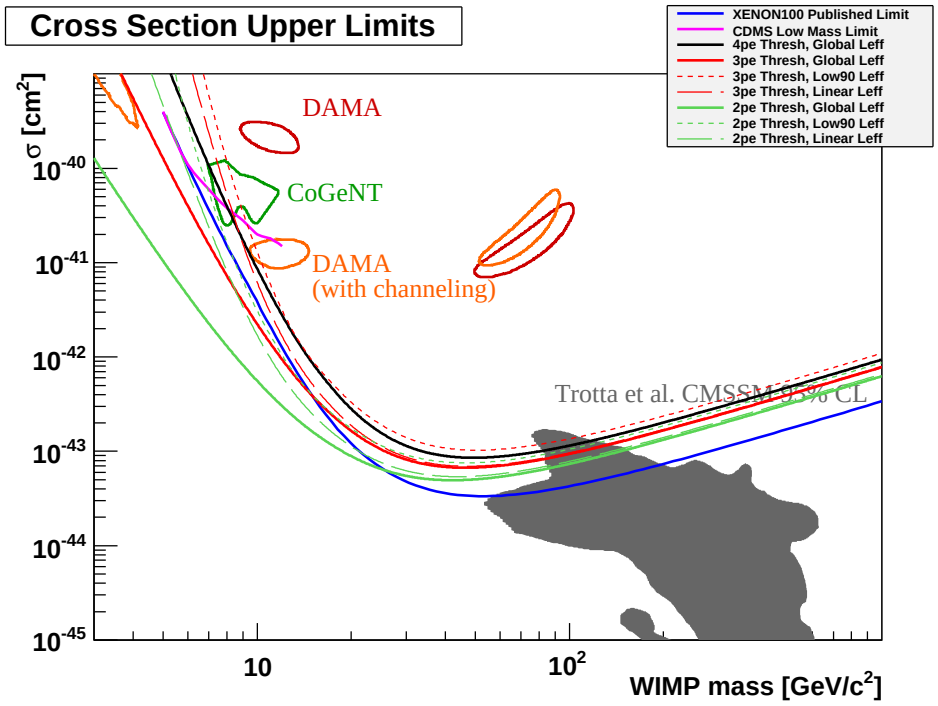

Figure 4.32: Upper limits on the WIMP-nucleon cross section for the standard analysis with reduced energy threshold. Also shown are the DAMA/Libra and CoGeNT contours and the theoretically predicted region.

Since XENON100 is still taking data, this analysis has great potential in establishing an increased sensitivity to low mass WIMP scattering. As the current and future data sets, which have significantly more exposure than the 11.17 day data set, are released, the S2 only analysis can be used to probe the cross section for low mass WIMPs to much smaller values, providing both a potential for the discovery of a low mass WIMP, and a consistency check for the standard analysis. Additionally, the correct implementation of the trigger threshold in the standard analysis will allow for a more robust calculation of the sensitivity in the standard analysis.

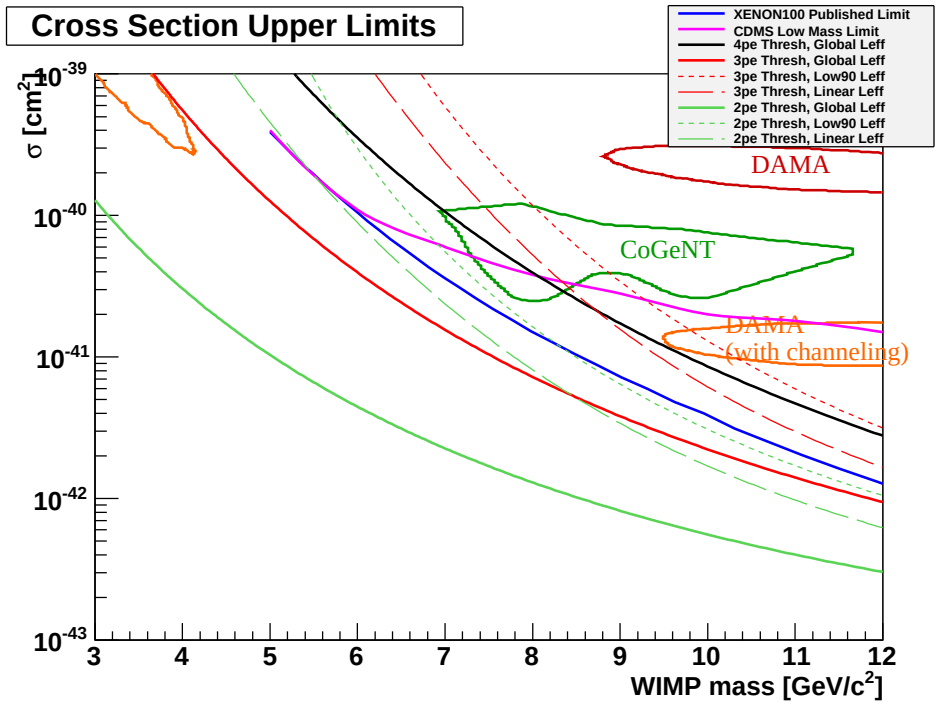

Figure 4.33: Zoomed view of the low mass region for the upper limits on the WIMP-nucleon cross section for the standard analysis with reduced energy threshold, along with the DAMA/Libra and CoGeNT contours.

CHAPTER 5

PMT Gain Calibrations for XENON100

All of the information about an event in XENON100 comes from the signals on the 242 PMT channels. To extract the information from these signals, it is necessary to convert the signals from ADC counts to photoelectrons, from which the energy can be determined by calibrations with radioactive sources. The conversion from ADC counts to the number of photoelectrons, which is parametrized by the gain, is then necessary for each PMT. This chapter outlines the gain calibration procedure and results for the XENON100 experiment.

5.1 Gain Calibration Setup

The principle of a gain calibration is quite simple for a setup with one PMT. The gain of a PMT is the ratio of the charge output from the PMT to the charge coming off of the photocathode. To measure the gain, one simply needs to measure this ratio.

The standard way to measure the gain of a PMT is to expose the tube to a very low intensity light source, such as an LED. The light source is pulsed so that the LED is only on for a small time interval on the order of nanoseconds, and an external trigger is set on this pulse, indepenent of whether the PMT receives a photon. The intensity is set low enough that on 95% of the triggers, the PMT does not collect a photon and only the pedestal is measured. Then, by

Poisson statistics, roughly 5% of the triggers will be single photoelectron events, and only a fraction of a percent of the triggers will be events with two or more photoelectrons. In this way, the charge input to the PMT is known.

The charge output of the PMT is then measured by integrating over the pulse duration. After rescaling by the electron charge, the spectrum can be fit to obtain the single electron response (SER) function. The SER function typically has a component for the pedestal, another for the single photoelectron contribution, and, in the presence of sufficient statistics, an additional component for the two photoelectron contribution. The gain is then determined by the mean value of the single photoelectron component of the SER function.

In XENON100, it was desirable to measure the gains of all 242 PMTs in situ, both to avoid systematic errors due to temperature and cabling differences and to be able to monitor the gains of the PMTs over the course of the experiment. To achieve this, a method had to be developed to measure the gains of all 242 PMTs simultaneously so the weekly calibrations could be performed without significantly affecting the runtime of the experiment.

A common light source was created by using external LEDs and optical fibers to route the light inside of the detector. Two blue LEDs were used, one for the TPC and another for the veto region. For the TPC, a one to four splitter was used to introduce the light at four points around the side of the TPC. In the veto, a one to six splitter was used to illuminate the top veto, the bottom veto, and four points around the side veto. The fibers were aimed such that they did not point at any PMTs, but the light could rather scatter and be collected from all PMTs. A schematic of the gain calibration setup is shown in figure 5.1.

While great effort was made to create a uniform light distribution, this was far from reality in practice. First, due to the total internal reflection at the

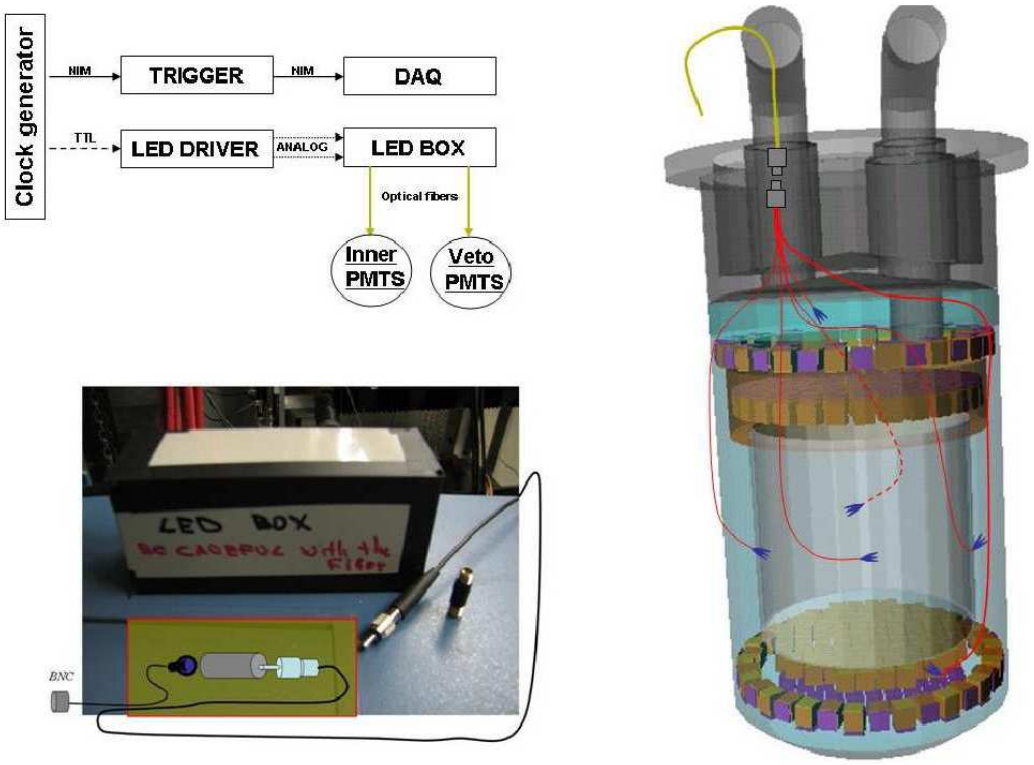

Figure 5.1: Schematic of the gain calibration setup for XENON100

liquid gas interface, the bottom PMT array was received much more light than the top array. Second, because of the strong geometrical dependence of the light collection in the veto, some veto PMTs were brightly illuminated and others were only dimly illuminated. Finally, the PMTs closest to the fibers also tended to receive more light than those farther away.

Both because of the non-uniformities in the light source and because there were so many PMTs to illuminate simultaneously, it was not possible to create a short LED pulse that would produce a single photoelectron for 5% of the triggers on all PMTs. Instead, another method was developed that is effectively equivalent. A long low intensity LED pulse, on the order of a few μs, was created that would flood the detector with single photons over the duration of the pulse.

The light level was set so that the most dimly illuminated PMTs would measure the pedestal on 95% of the triggers. The most brightly illuminated PMTs would then have many photoelectron events on each trigger, but this is handled by adjusting the search window for photoelectrons to each PMT. For the dimly illuminated tubes, the entire pulse duration is used to search for photoelectron signals, while for the brightly illuminated PMTs, only a short interval just after the LED is turned on is used. The search window is adjusted for each channel so that on each PMT there is no photoelectron signal for 95% of the triggers.

Rather than integrating over the entire pulse duration, a peak finding algorithm was developed that would identify photoelectron pulses. The charge was then integrated for a 50 ns window centered at the peak of the photoelectron pulse. Using this algorithm, it is possible to count the number of photoelectron pulses within a given search window size, and for each channel, the search window was reduced until there was only one pulse in 5% of the triggers. Since many conditions can change between calibrations and there is no guarantee that the light level is precicely the same on all 242 PMTs, an automatic procedure was developed to set the search window to the correct length on each calibration.

One artifact of the pulse finding algorithm is that the signal when there is no photoelectron is no longer the pedestal. Instead, since the search algorithm finds the peak in the noise, it is a biased distribution of the noise. This is not a problem, however, because the pedestal is not used to calculate the gain. The DAQ is set with a pretrigger of 100 samples before the LED is turned on, and this is used to calculate the baseline. The baseline is then subtracted from the entire waveform before the peak finding search is performed so that the peak integration is the actual charge relative to the baseline. This is important to note because the noise peaks in the gain spectra are shifted slightly from zero, yet the

single photoelectron portion of the SER function is indeed scaled correctly.

5.2 Gain Calibration Results

5.2.1 SER Functions for Gain Spectra Analysis

Although great care was taken to create a uniform light level on each PMT, slight differences still existed. In addition to this, some PMTs exhibited a different response, particularly in the amplification of the first dynode, yielding a different spectral shape. Thus, a universal SER function was not optimal, and instead several fitting functions were considered, and the analysis software was designed to choose the function that minimized χ^2 per degrees of freedom.

The SER functions considered follow two general forms. The first assumes a gaussian for the noise, and gaussians for the one and two photoelectron contributions,

$$S = A_N exp(-\frac{(x-x_N)^2}{2\sigma_N^2}) + A_1 exp(-\frac{(x-x_1)^2}{2\sigma_1^2}) + A_2 exp(-\frac{(x-x_2)^2}{2\sigma_2^2}) \quad (5.1)$$

where A_i is the amplitude, σ_i is the width, and x_i is the peak position for the noise, one and two photoelectron contributions.

Equation 5.1 can be used unconstrained, with 9 free parameters, or there are several constraints that can be imposed. The first constraint is when the statistics are low enough that the two photoelectron contribution is negligible. In this case, A_2 is set to zero and there are only six free parameters for the fit.

When there are sufficient statistics that the second photoelectron peak is clearly visible, equation 5.1 can either be used unconstrained, or any of the parameters for the second photoelectron peak can be constrained based on the

linearity of the PMT,

$$x_2 = 2x_1 \tag{5.2}$$

or based on Poisson statistics,

$$\sigma_2 = \sqrt{2}\sigma_1 \tag{5.3}$$

$$A_2 = \frac{A_1\sigma_1}{\mu\sigma_2} \tag{5.4}$$

where μ is the mean value of the poisson distribution. The selection of which parameters are fixed and which are left free is determined by minimizing χ^2.

In the event that a spectrum does not match a gaussian distribution, a Poisson function can be used for the SER function,

$$S = A_N exp(-\frac{(x - x_N)^2}{2\sigma_N^2}) + A_1 \frac{x_1^{x/b} e^{-x_1}}{\Gamma(\frac{x}{b} + 1)} \tag{5.5}$$

This function, with only six free parameters, is ideal when there is poor amplification on the first dynode in the PMT.

Figure 5.2 compares the fits for the SER function using equations 5.1 and 5.5. In this particular example, the both fits are similar and the gain differs only by 2%, but since χ^2 is reduced by 5% by using the Poisson function this fit was automatically selected for this measurement.

5.2.2 Results of Gain Measurements

Gain calibrations are performed weekly, and the resulting SER function is found for all PMTs, such as shown in figure 5.3. From the SER function, several important PMT parameters can be extracted. In addition to the gain, the peak to valley ratio, the signal to noise ratio, and the spread in the single photoelectron and noise peaks are calculated for each measurement. All of these parameters are monitored over time to ensure that the PMTs' functionality is not deteriorating with time.

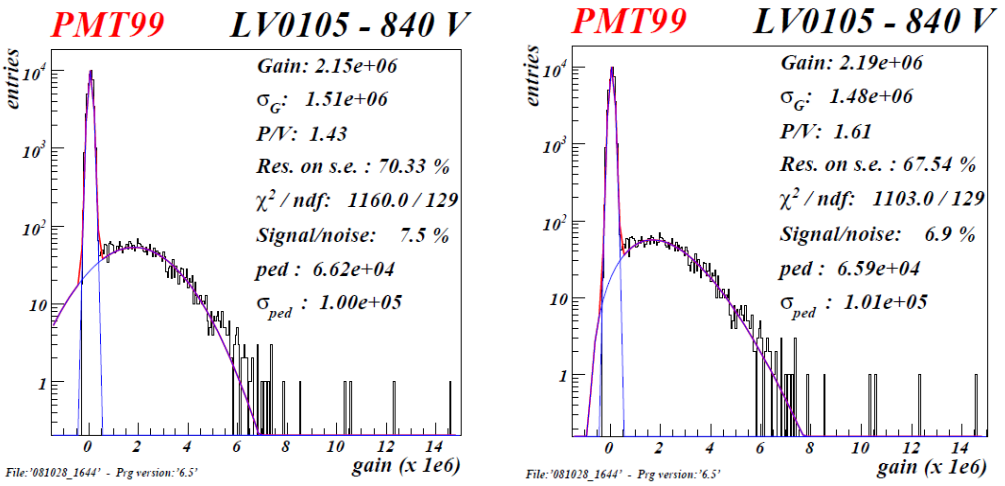

(a) Equation 5.1 with $A_2 = 0$ (b) Equation 5.5

Figure 5.2: Comparison of different fits for the SER function for PMT 99.

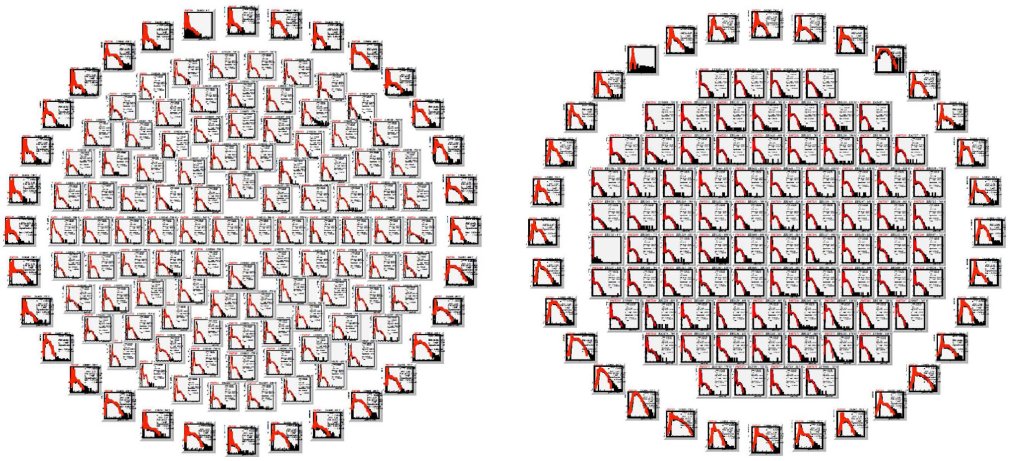

(a) Top (b) Bottom

Figure 5.3: Map of gain calibration spectra for all 242 PMTs in the detector.

5.2.3 Gain Equalization

In principle, as long as the value of the gain is known, the ADC counts can be converted into photoelectrons for each PMT, but in practice, it is desirable to fix the gains of each PMT to a common value. Doing so ensures that all PMTs

will have a similar dynamic range, being bounded below by the need to resolve single photoelectrons and bounded above by non-linearity and saturation. Thus, the gains of all 242 PMTs in XENON100 were equalized to a common value of 2×10^6.

To equalize the gains, a high voltage response function is found for each PMT by measuring the gain vs high voltage supply. An example of this is shown in figure 5.4. The response for each PMT was fit with a power law, and the resulting function was used to calculate the high voltage necessary for the equalized gain value. The distribution for the gains after equalization is shown in figure 5.5. There is a peak around the desired value of 2×10^6. The spread in the peak is due to the 5 volt resolution of the high voltage supply. Additionally, the tail at lower gain values is due to the fact that no PMT was supplied with greater than 900 V.

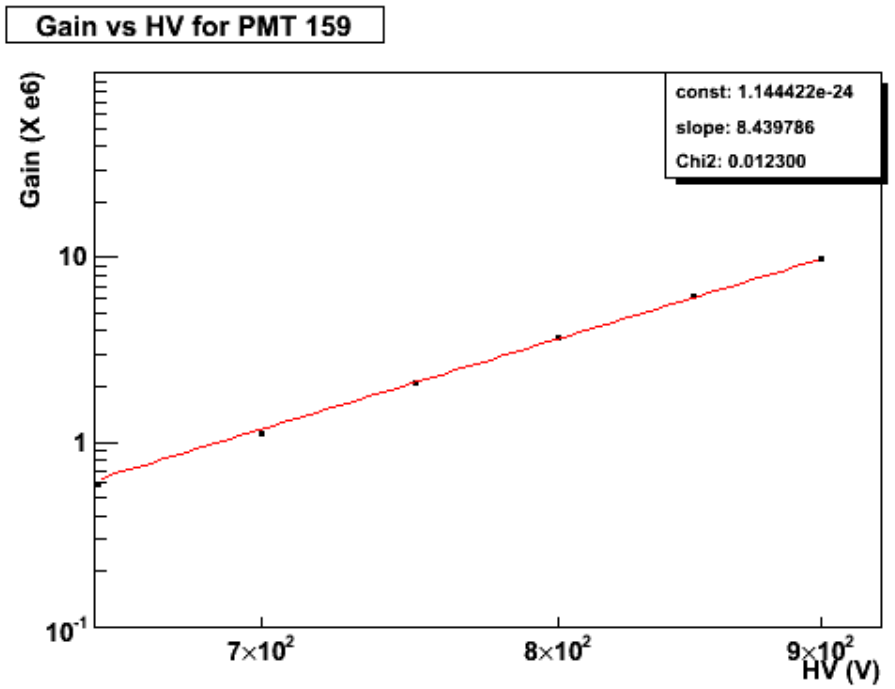

Figure 5.4: Gain Vs High Voltage measurement for PMT 159 and power law fit.

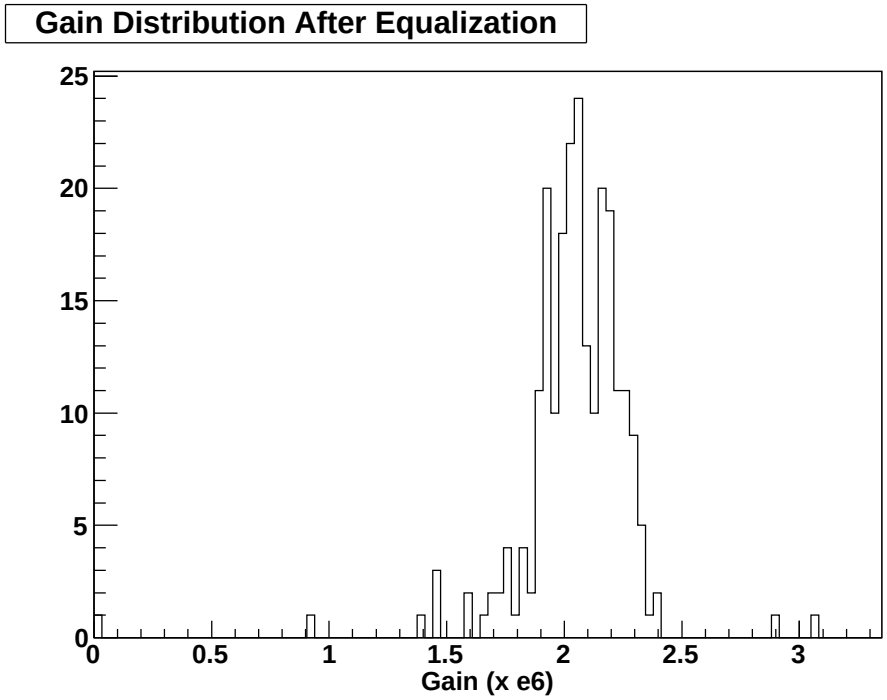

Figure 5.5: Distribution of gains after equalization, showing a peak at the desired gain of 2×10^6.

CHAPTER 6

Field Simulations and Radioactivity Screening for the QUPID Photo Sensor

6.1 The QUPID Photo Sensor

As low background detectors, such as those for dark matter and neutrinoless double beta decay searches, become larger and more sensitive, the backgrounds must correspondingly be reduced significantly. External backgrounds can be reduced by larger and more efficient shielding structures, and internal backgrounds can be reduced to some extent by fiducializing the target volume, but ultimately, to achieve ton scale and multi-ton scale detectors, the materials used for construction must be extremely radio-pure.

Liquid noble detectors, as well as others that use photo sensors, suffer from the fact that PMTs have an intrinsically high radioactivity compared to the other materials used. Since the PMTs must be placed near the active volume, and used in sufficient quantity to obtain a high light yield for low energy sensitivity, they contribute a substantial amount of the background.

To address this issue, a new photo sensor has been developed with an extremely low radioactivity. The QUartz Photon Intensifying Detector (QUPID), shown in figure 6.1 is made entirely from low activity quartz, and accelerates photoelectrons from a photocathode to a tiny avalanche photo diode (APD) at

the center. Conventional PMTs use a dynode chain made of materials with a high radioactivity, so the QUPID, which has designed without these components, has the potential to be dramatically less radioactive. Additionally, to supply the voltage on the dynode chain in a conventional PMT, a resistor chain is necessary, which adds additional radioactive components.

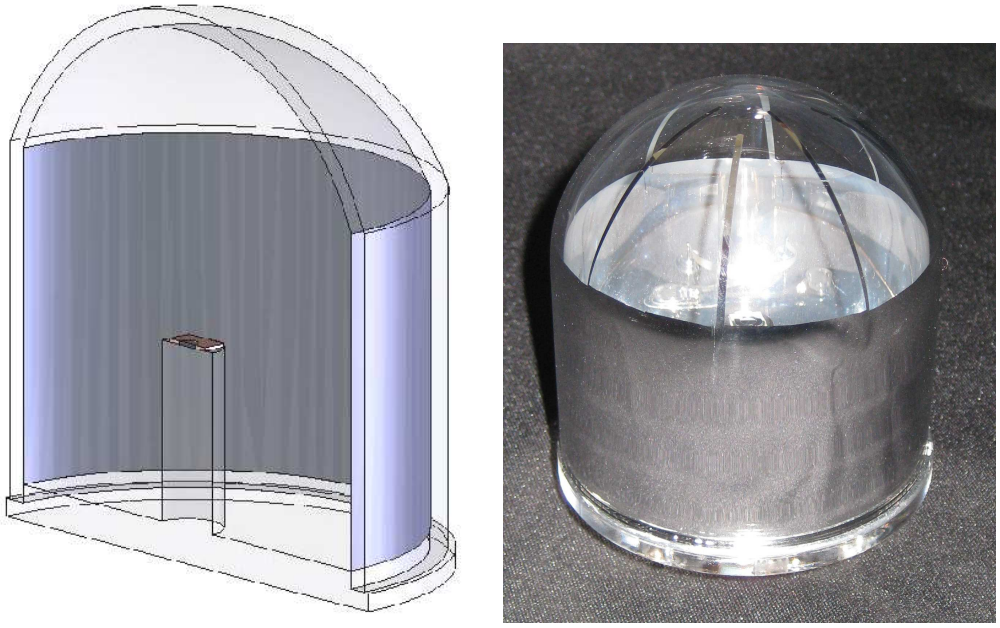

(a) (b)

Figure 6.1: The QUPID photo sensor

An APD is a diode made of a p-n junction. When a reverse bias voltage is applied, small excitations create an avalanche breakdown. The strong field inside the device accelerates an electron hole pair, causing the creation of more electron hole pairs. Thus, a small disturbance can cause a large current to flow in the avalanche process. Typically, an electron hole pair is created by the photoelectric effect when a photon is incident on the APD, but in the case of the QUPID, an electron from the photocathode penetrates the APD and triggers the avalanche.

The size of the avalanche in the APD inside a QUPID is governed by two

parameters, the bias voltage on the APD and the energy of the incident electron. At low bias voltage, the field inside the APD is too low to create a breakdown across the p-n junction, and the incident charge flows without an avalanche gain. However, at higher bias voltage, the avalanche increases, giving a gain of around 200 near breakdown voltage. The dependence of the bias voltage on the avalanche gain is shown in figure 6.2.

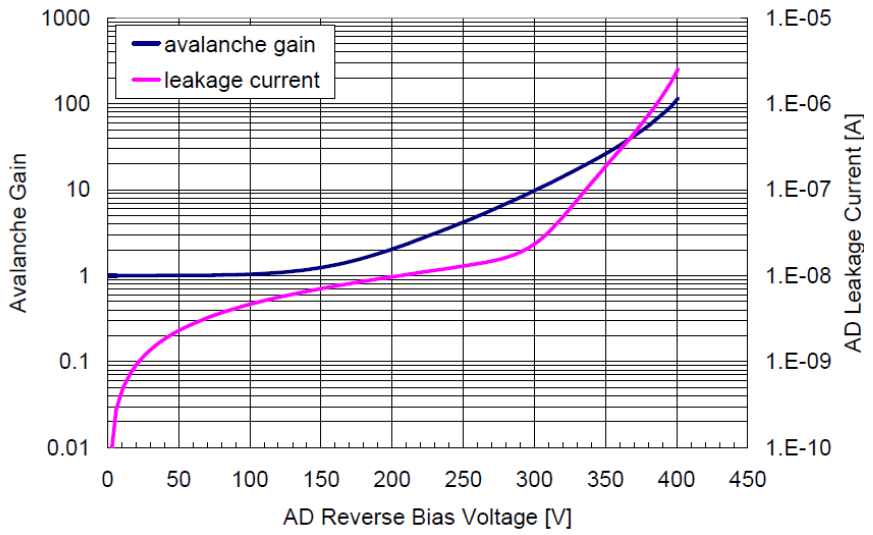

Figure 6.2: Avalanche gain as a function of bias voltage for the QUPID

The other factor governing the gain of the QUPID is the energy of the incident photoelectron, which is proportional to the voltage applied to the photocathode. This portion of the amplification is called bombardment gain. At low energy, the electron simply penetrates the APD and triggers an avalanche, in which case the gain is entirely due to the avalanche gain, and the bombardment gain is 1. However, at higher energy, the incident electron creates multiple electron hole pairs, each of which can then contribute to the avalanche breakdown. Figure 6.3 shows the bombardment gain of the QUPID as a function of photocathode high voltage.

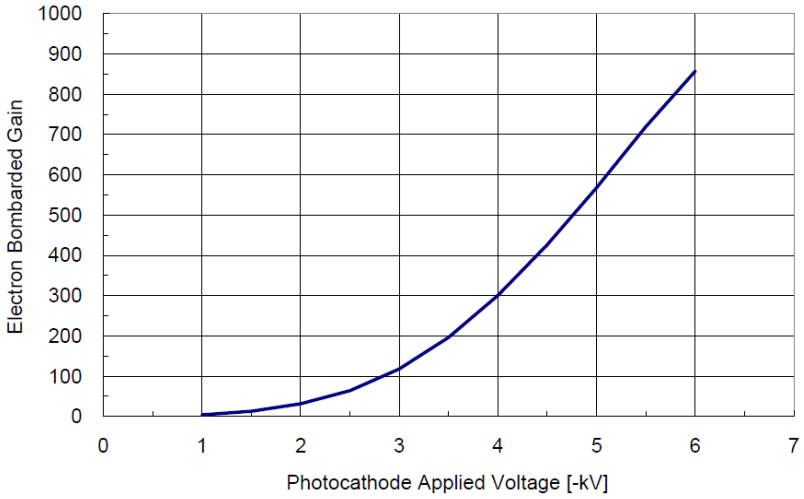

Figure 6.3: Bombardment gain for the QUPID as a function of photocathode high voltage

Conventional PMTs in low energy experiments are typically operated at a gain of $10^5 - 10^6$, which is sufficient to count individual photoelectrons. This is a mandatory requirement to obtain a good energy resolution for low energy recoils. For the QUPID to replace conventional PMTs, it must also satisfy this requirement. By combining the bombardment gain with the avalanche gain, and using an external amplifier, one, two and three photoelectrons are clearly visible in the QUPID, as shown in figure 6.4, demonstrating the QUPID's ability to be used as a photon counting device.

6.2 Field Simulations for the QUPID

In order to understand and optimize the QUPID operation, several field simulations were conducted to calculate the electric field inside the device and to find the trajectories of photoelectrons emitted from the photocathode. The calculations were greatly simplified due to the nearly perfect cylindrical symmetry of

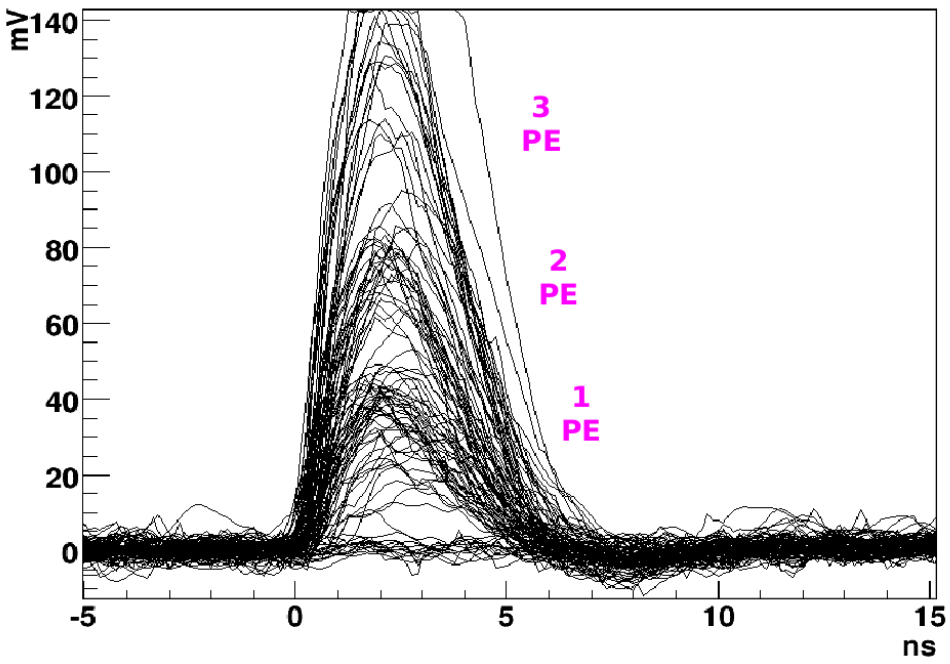

Figure 6.4: Response of QUPID to photoelectrons, clearly showing that one, two and three photoelectrons are clearly visible.

the QUPID, allowing the simulations to be performed in two dimensions.

6.2.1 Original QUPID Design

The first simulations conducted were for the original design of the QUPID shown in figure 6.1. Using this design, the electric potential was calculated inside the QUPID and the electron trajectories were obtained. Figure 6.5 shows the equipotential lines and the electron trajectories for operation with the photocathode at -6 kV and the APD at ground. One can see that the device is designed so that electrons ejected from all points on the photocathode are focused to the center of the APD, minimizing charge collection loss due to geometrical effects.

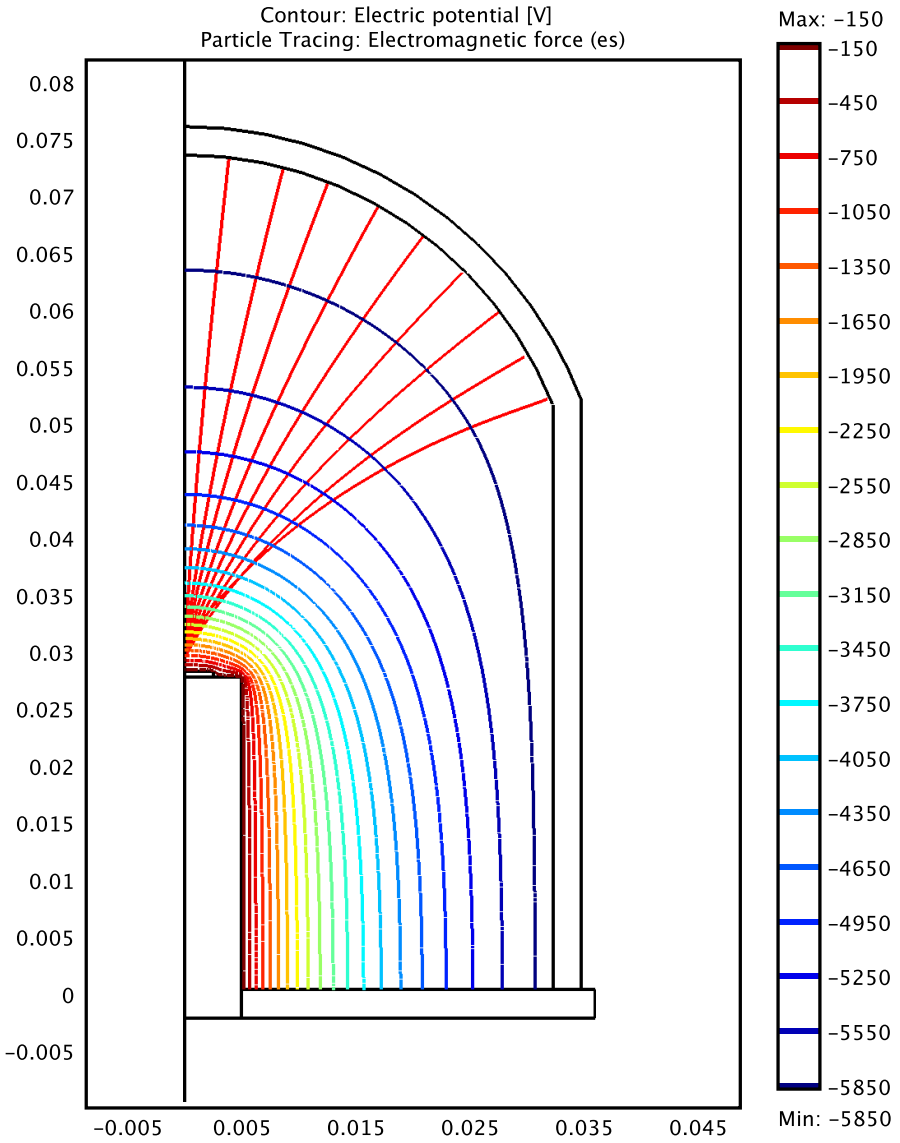

Figure 6.5: Electron Trajectories for the QUPID Photo Sensor

6.2.2 Sparking Inside the QUPID

One unforseen problem that arose in the development of the QUPID was sparking inside the device. Because quartz is such a strong electric insulator, a large amount of charge can easily build up on the surfaces inside the QUPID. Indeed,

it proved very difficult to make a functional QUPID that would operate at −6 kV without sparking.

In order to resolve this problem, the design was changed so that the exposed quartz on the inside of the QUPID was covered with resistive and conducting coatings, thus eliminating the build up of charge. The final design holds the bottom plate of the QUPID at ground and has a resistive layer partway up the outer edge. A new simulation was performed with this design, shown in figure 6.6, and it was found that the device could still function as in the original design, with all electron trajectories well focused at the center of the APD, without the charge buildup problem.

6.2.3 Simulations for different sized QUPIDs

Since xenon and purified argon are quite expensive, large scale liquid noble detectors are designed to waste as little of the target material as possible. The liquified noble gases seep into every gap between detector materials inside the cryostat, so there is always some waste, but great effort is made to minimize this. The gaps between PMTs, therefore, introduces plenty of spaces for wasted target material to accumulate. Because of this, it is desirable to consider constructing different sized QUPIDs that will help minimize wasted target material.

The first approach is to make a shorter version of the standard 3 inch QUPID, which would have less gap space around the device for the same photocathode coverage. Electron trajectory simulations were performed for QUPIDs that were shortened by 5, 10 and 15 mm, as shown in figure 6.7. No effect was seen in the electron focusing for the 5 and 10 mm shortened versions, but at 15 mm the focus point began to spread, as shown in figure 6.8. It was determined that the QUPID can be made 10 mm shorter without changing the operation of the device.

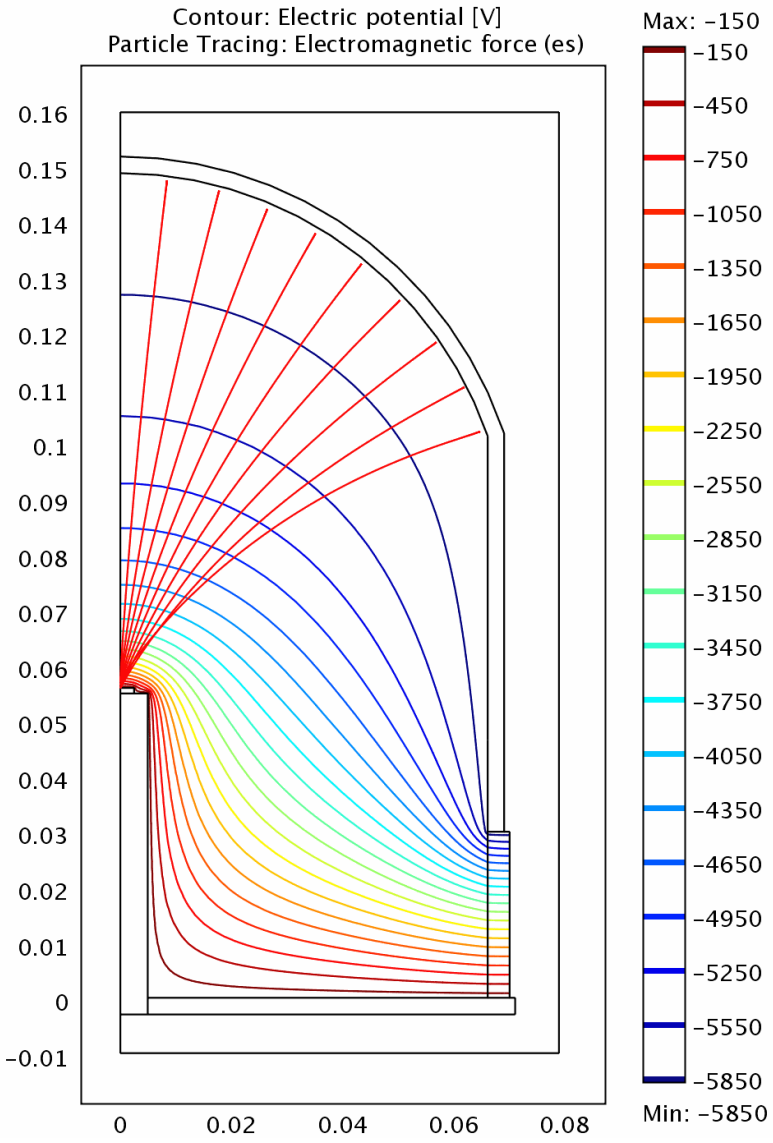

Figure 6.6: Trajectories of photoelectrons for the new QUPID design

Another approach to reduce dead regions is to make larger versions of the QUPID so that there is more photocathode coverage per PMT. This has the added feature that large detectors can be built with fewer channels as well. A 6 inch version of the QUPID is also being developed for this purpose. Simulations for this version have also been performed to obtain the electron trajectories for

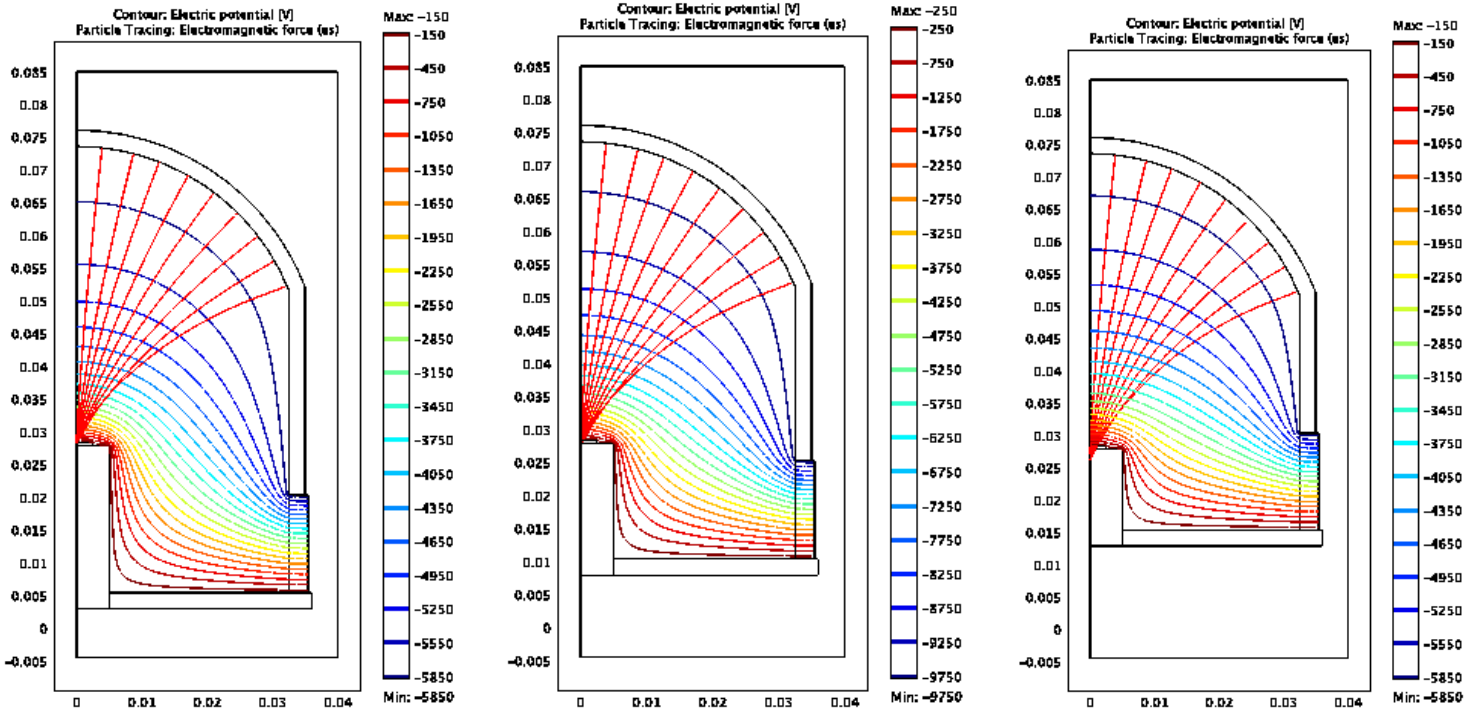

(a) Shortened by 5 mm (b) Shortened by 10 mm (c) Shortened by 15 mm

Figure 6.7: Electron trajectories for shortened versions of the standard 3 inch QUPID.

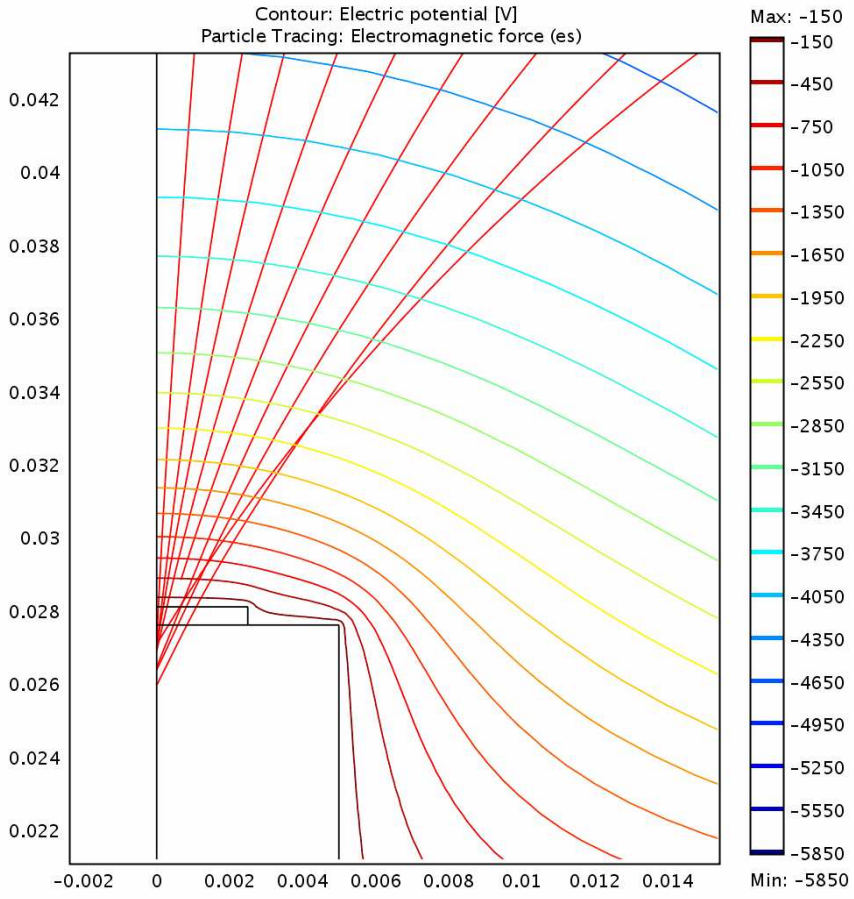

Figure 6.8: Zoom of the focus point of the electron trajectories for the 15 mm shortened version of the QUPID

operation at −6 kV. Figure 6.9 shows how the electron trajectories for this model are well focused on the APD, thus validating the optimal operation of this larger model.

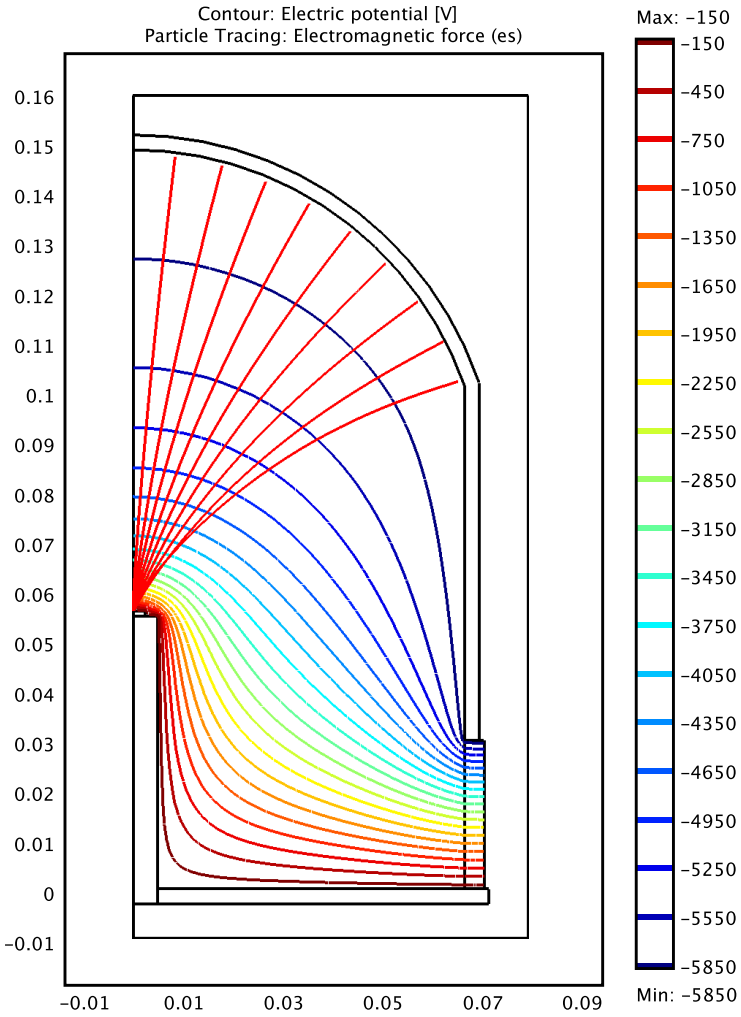

Figure 6.9: Electron trajectories for a 6 inch version of the QUPID

6.2.4 QUPID Operation in an External Magnetic Field

It is well known that operation of PMTs in an external magnetic field, such as that of the earth, can alter the electron trajectories, and hence the performance of

the tube [32]. Simulations were thus performed to determine whether this effect would also be present in the QUPID. The electron trajectories inside the QUPID were recalculated under the maximal condition that the QUPID is oriented such that the external magnetic field from the earth (with a strength of 0.5 Gauss) is perpendicular to the electron paths. The photocathode high voltage was also varied from -1 kV to -6 kV.

In all cases, the effect of introducing the magnetic field term was negligible, indicating that the QUPID should not be sensitive to this effect, even under operation at low photocathode voltages.

6.3 Uniformity Measurements

The uniformity of a PMT's response to light incident across the surface of the photocathode is affected by two processes. First, nonuniformities in the photocathode create a variance in the photocathode current as a function of position. The second contribution comes from nonuniformities in the electron collection of photoelectrons.

To disentangle the two effects, two uniformity measurements are made. First, the photocathode current is measured, which only depends on the nonuniformities of the photocathode and is independent of photoelectron collection. Second, the anode current is measured, which depends on both the photocathode nonuniformities and the electron collection efficiency. To extract the collection efficiency, the ratio of the two measurements can be used to cancel the contribution of the photocathode nonuniformity.

A two dimensional scanner was constructed to perform uniformity measurements on the QUPID, as shown in figure 6.10. The light is provided by a DC

LED, which is routed through an optical fiber and focused by a lens to a point on the QUPID surface. The lens is attached to an arm that can rotate along the polar angle of the QUPID surface across both edges of the photocathode. The QUPID is mounted such that it can be rotated 180° in azimuth, thus allowing a scan of the entire face of the device. The glass tube on the base of the QUPID, the only feature that breaks the azimuthal symmetry, is set to zero azimuth.

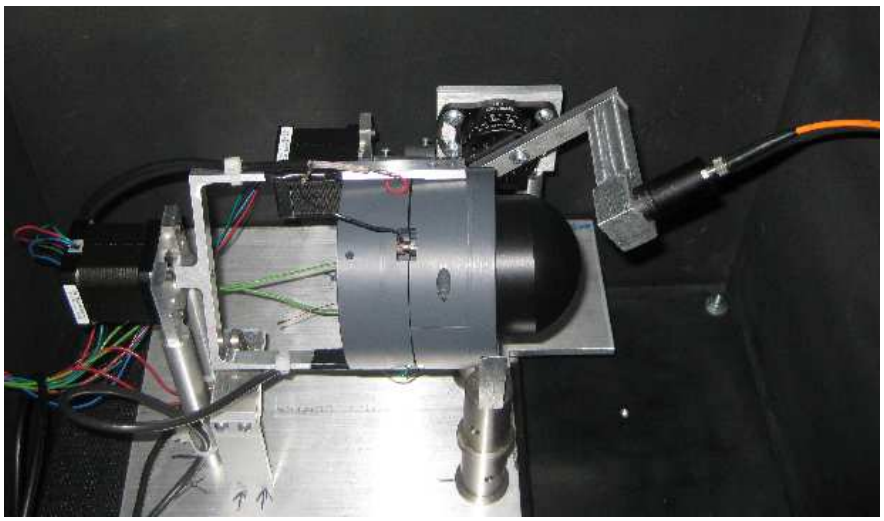

Figure 6.10: Picture of the 2D uniformity scanner for the QUPID

6.3.1 Cathode Uniformity Measurements for the QUPID

The cathode uniformity is obtained by measuring the photocathode current as a function of position on the surface of the QUPID. To measure the photocathode current, a positive voltage is applied to both the anode and cathode of the APD and to the grounding ring at the base of the QUPID. The photocathode is connected to ground through a picoammeter. This way, the entire base of the QUPID and the APD act as the anode, collecting all photoelectrons that are ejected from the photocathode, independent of the collection efficiency.

There are two free input parameters for the uniformity scan, the light intensity and the anode voltage. The photocathode current should be proportional to the light intensity, and all nonuniformities should also scale linearly with intensity, up to the point where the photocathode begins to saturate. There should be very little dependence on the anode voltage, since only a weak field is necessary to collect photoelectrons.

A uniformity measurement was performed on a developmental version of the QUPID, serial number QHA34. Figure 6.11 shows the uniformity along a slice at $\phi = 0°$ for various anode voltages ranging from 25 V to 200 V. As expected, there is no dependence on the anode voltage, however, nonuniformies are clearly visible at the level of 20%.

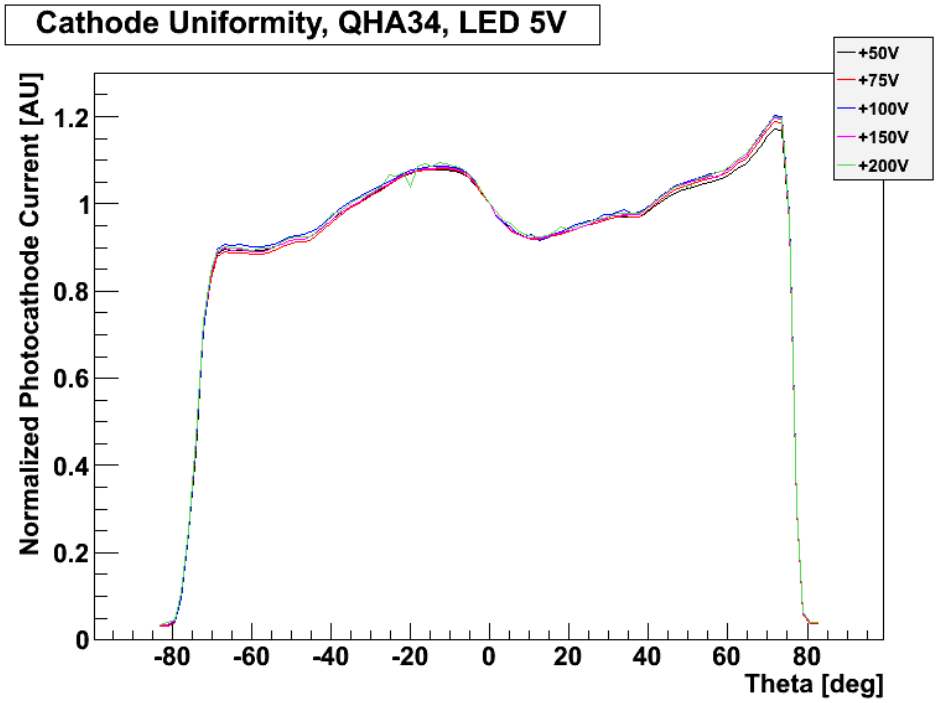

Figure 6.11: Normalized photocathode current along a slice at $\phi = 0°$ for anode voltages ranging from 25 V to 200 V.

For the light intensity dependence, the LED driver was varied from 4 V to 9 V, but the luminosity was not known, so the light intensity was instead parametrized by the maximum photocathode current. The dependence of the light intensity on the cathode uniformity for a slice at $\phi = 0°$ is shown in figures 6.12 and 6.13, which show the photocathode current in absolute and normalized scales respectively. In both figures, the same nonuniformity is seen as in the scan of anode voltages. At the brightest LED settings, the peak portions of the curves are flattened, which is evidence of photocathode saturation at around 150 to 175 nA, but otherwise there is no dependence on the luminosity.

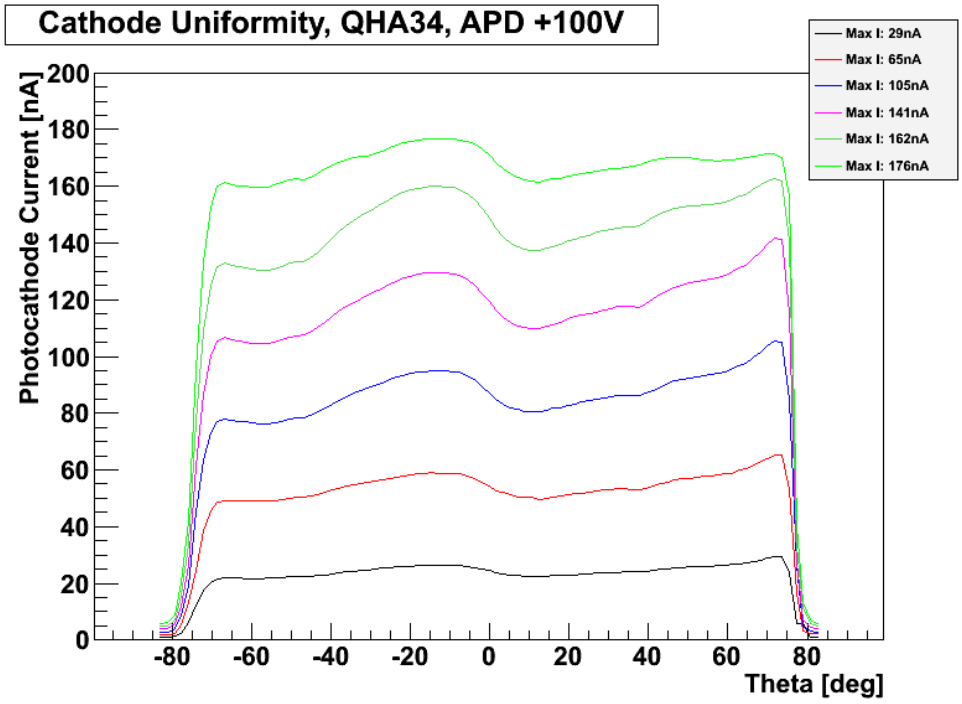

Figure 6.12: Photocathode current along a slice at $\phi = 0°$ for different light intensities

Figure 6.14 shows a contour plot of a full two dimensional scan with an anode voltage of +100 V and a light intensity equivalent to a maximum photocathode

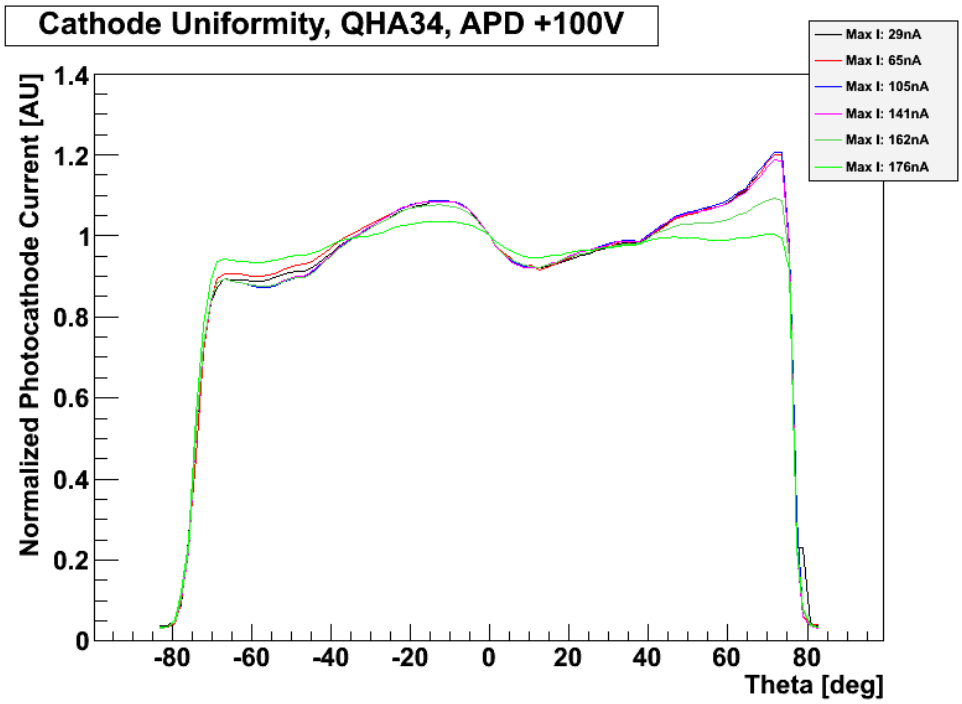

Figure 6.13: Normalized photocathode current along a slice at $\phi = 0°$ for different light intensities

current of 65 μA. The location of the edge of the photocathode and the glass tube are marked with black circles. Here the features of the nonuniformity are more clearly recognizable. In particular, there is a decreased photocathode current on the left side of the figure due to the fact that the post for the APD lies directly between this region of the photocathode and the glass tube. Since the photocathode material is sprayed in through the tube, there is a shadowing effect that results in a diminished photocathode application in that region, and hence a lower quantum efficiency. However, with the exception of a small region in the upper left of the figure, the fluctuations are only around 20%. Figure 6.15 shows slices along $\phi = 0°$ and $\phi = 90°$ for the cathode uniformity at these settings.

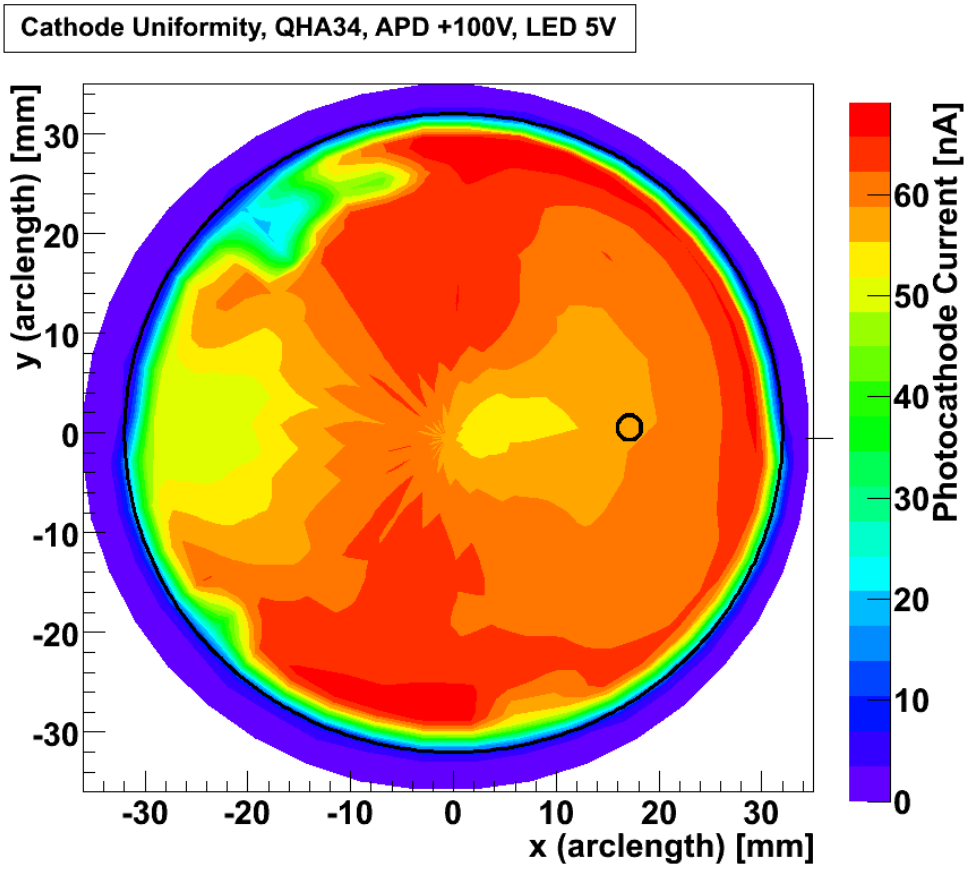

Figure 6.14: Photocathode current for a two dimensional scan of the QUPID surface, with the location of the edge of the photocathode and the glass tube marked with black circles

6.3.2 Anode Uniformity Measurements for the QUPID

Anode uniformity measurements for the QUPID are obtained by measuring the anode current with the QUPID operating in normal conditions. A high voltage is applied to the photocathode to obtain an electron bombardment gain, and a reverse bias voltage is applied to the APD for an avalanche gain. The anode current then contains the photocathode nonuniformities, the electron collection efficiency and the gain.

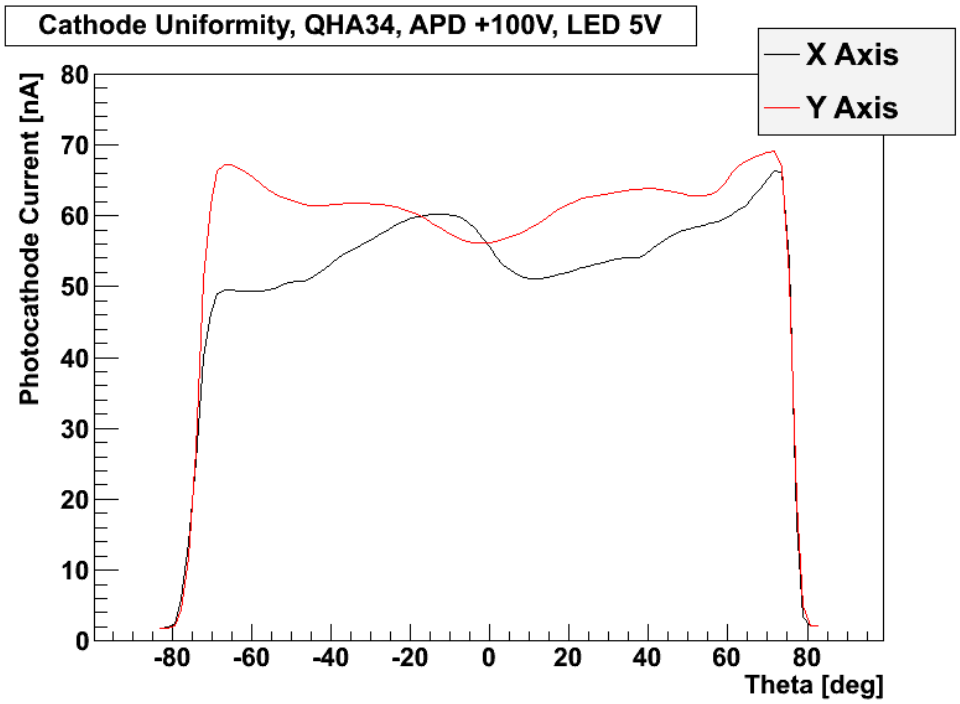

Figure 6.15: Photocathode current along slices at $\phi = 0°$ and $\phi = 90°$

For anode uniformity, there are three input parameters that can be varied, the APD bias voltage, the light intensity and the photocathode high voltage. While the cathode nonuniformities should not depend on any of these parameters, the electron collection efficiency is expected to depend on the photocathode high voltage, since at higher field the fluctuations in initial photoelectron directions become negligible and they are more uniformly focused to the APD.

The anode uniformity was measured for the same QUPID, QHA34. The APD bias voltage was varied from -100 to -200 V. The breakdown voltage of the APD is just below -400 V, however, a large noise appeared when operation above -200 V was attempted. Therefore, this QUPID was not tested above -200 V. Figure 6.16 shows the normalized anode current along a slice at $\phi = 0°$ for APD bias voltages ranging from -100 to -200 V. No dependence on the bias voltage was

observed in this range of operation. The features from the cathode uniformity measurement are still present, but with a decrease in anode current at the edges of the QUPID.

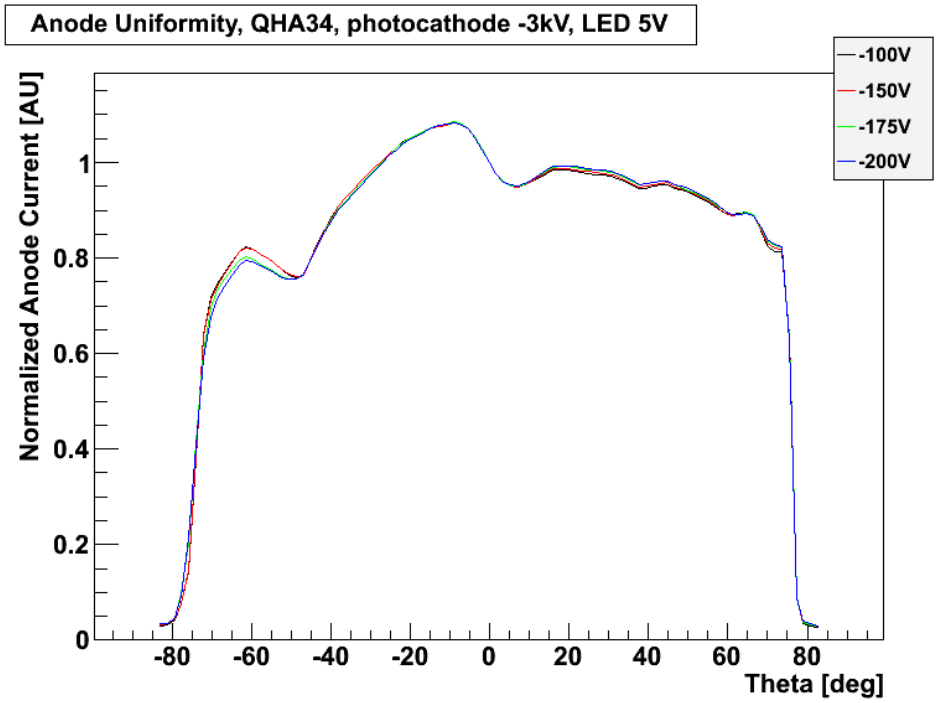

Figure 6.16: Normalized anode current along a slice at $\phi = 0°$ for different APD bias voltages

For the variation of the light intensity, a similar measure of the intensity as was used in the cathode uniformity was used for the anode uniformity, with the exception that the photocathode current was not explicitly measured. Thus, it was estimated by dividing the anode current by the gain. The scans were conducted at a photocathode high voltage of -3 kV and an APD bias voltage of -175 V, which corresponds to a bombardment gain of 120 and an avalanche gain of 1.25 for a total gain of 150.

Figure 6.17 shows the normalized anode current along a slice at $\phi = 0°$ at

different light intensities. The anode uniformity does not exhibit any dependence on the light intensity, and the same features are seen as in the previous anode scans. However, unlike the cathode uniformity measurement where saturation was observed at the brightest luminosities, there is no evidence of saturation in the anode scans. Indeed, the maximum photocathode current for the brightest LED setting is 35 nA, compared to 175 nA at the same light intensity in the cathode scans.

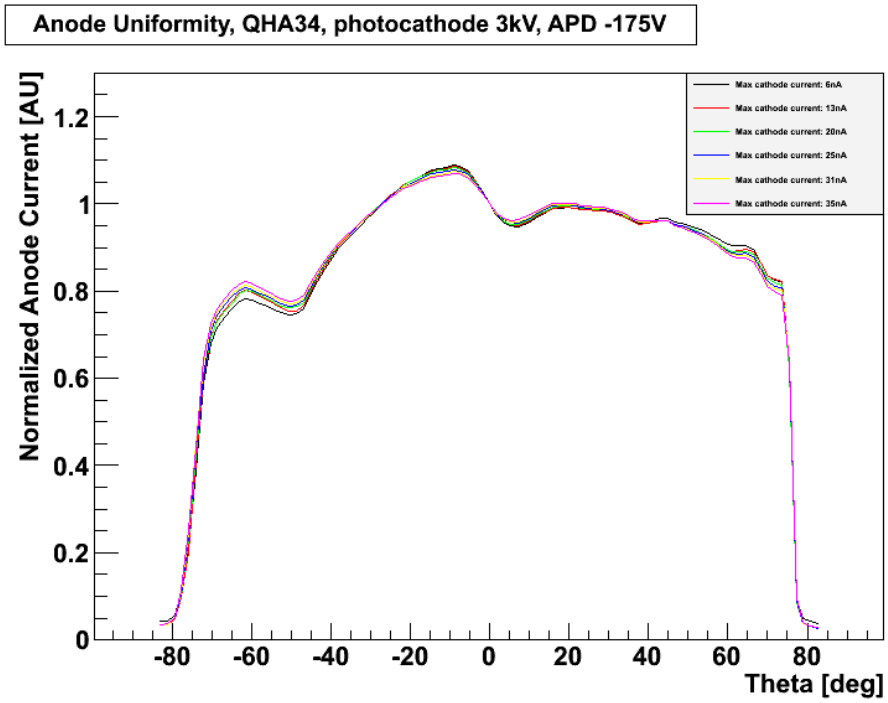

Figure 6.17: Normalized anode current along a slice at $\phi = 0°$ for different light intensities

While the scans used the same LED driver settings, and therefore the same light intensity, the circuit for the photocathode was changed slightly. In the cathode scans, the photocathode was connected through the picoammeter to ground, with a current limitting resistor of 500 MΩ in series. For the anode

scan, the picoammeter was replaced with a high voltage supply. This changed the impedance of the circuit sufficiently to reduce the photocathode current by a factor of 5, and therefore the anode scans never reached a photocathode current where saturation occurred.

The photocathode high voltage was varied between -1 kV and -6 kV. The dependence on this parameter is shown for a slice at $\phi = 0°$ in figure 6.18. While the variation in normalized anode current is much greater vs photocathode high voltage than for any other input parameter, there is no clear trend as a function of high voltage. Even with these fluctuations, the shape of the nonuniformities is still clearly visible.

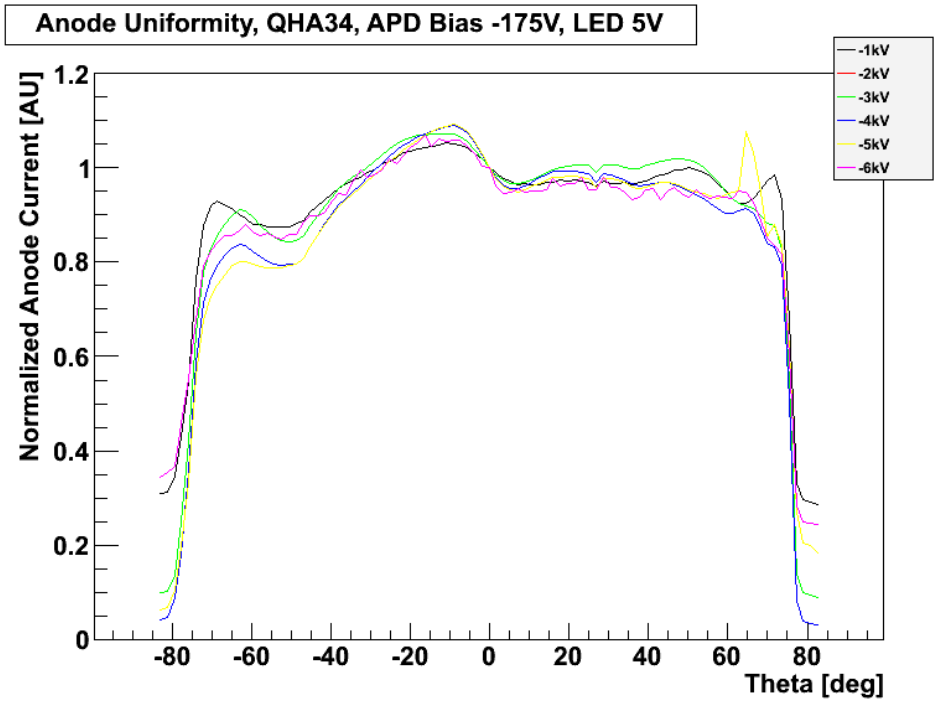

Figure 6.18: Normalized anode current along a slice at $\phi = 0°$ for different photocathode high voltages

A contour plot of a two dimensional scan of the anode uniformity is shown in

figure 6.19 with a black circle marking the edge of the photocathode. The features present in the cathode uniformity two dimensional scan are present, with the addition of a decreased anode current toward the edge of the photocathode. This is due to a lower electron collection efficiency in this region caused by imperfections in the field, and hence poor focusing of the photoelectrons on the APD. Slices along $\phi = 0°$ and $\phi = 90°$ are shown in figure 6.20.

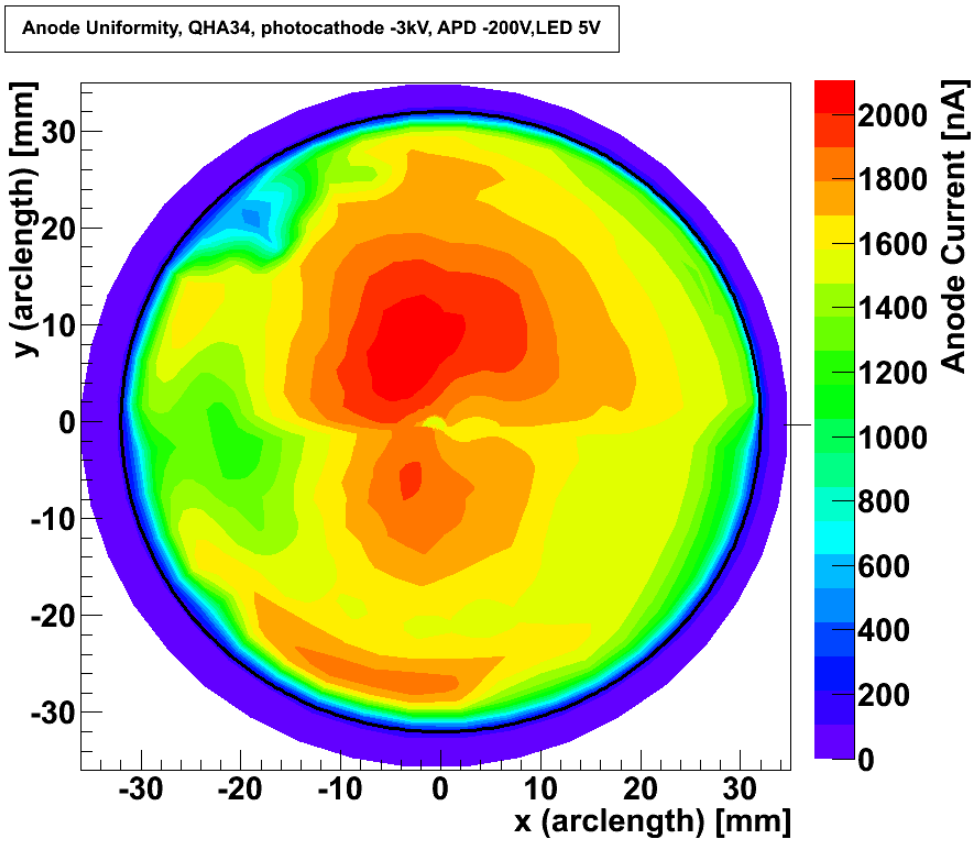

Figure 6.19: Contour plot of the anode current on the surface of the photocathode, with a black circle marking the edge of the photocathode

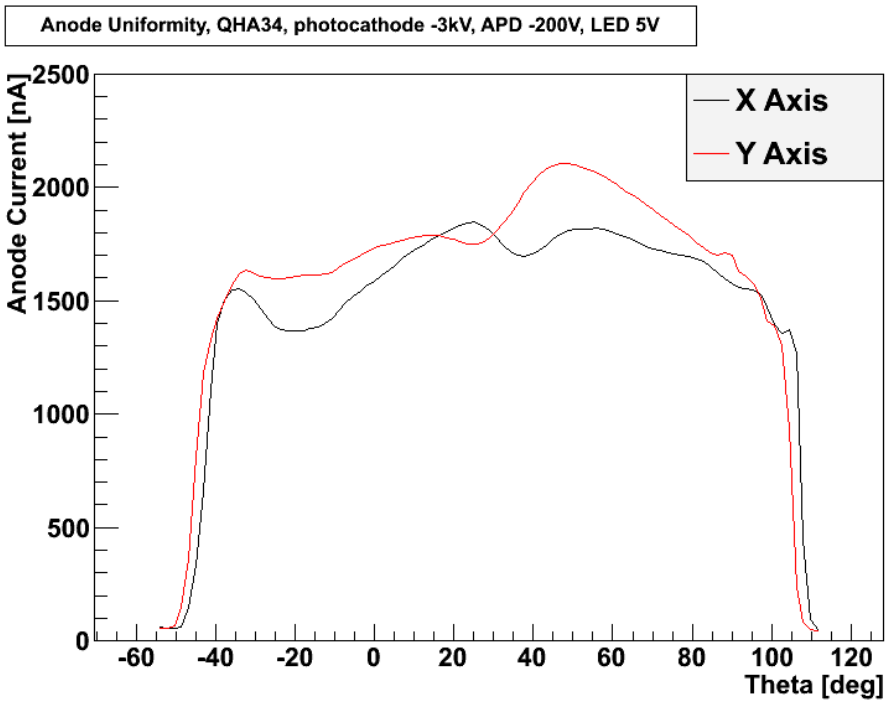

Figure 6.20: Anode current

6.3.3 Collection Efficiency of the QUPID

Once the cathode and anode uniformities have been measured, it is possible to decouple the photocathode nonuniformities from the electron collection efficiency by taking the ratio of the anode to cathode current. Figure 6.21 shows the collection efficiency obtained from the cathode uniformity taken with an anode voltage of +100 V and the LED driver set at 5 V and from the anode uniformity taken with an APD bias voltage of -175 V, a photocathode high voltage of -3 kV and the LED driver set at 5 V. The collection efficiency is fairly flat across the surface of the QUPID, but indeed tends to decrease toward the edge by around 20%. Orthoganal slices at $\phi = 0°$ and $\phi = 90°$ are shown for the collection efficiency in figure 6.22.

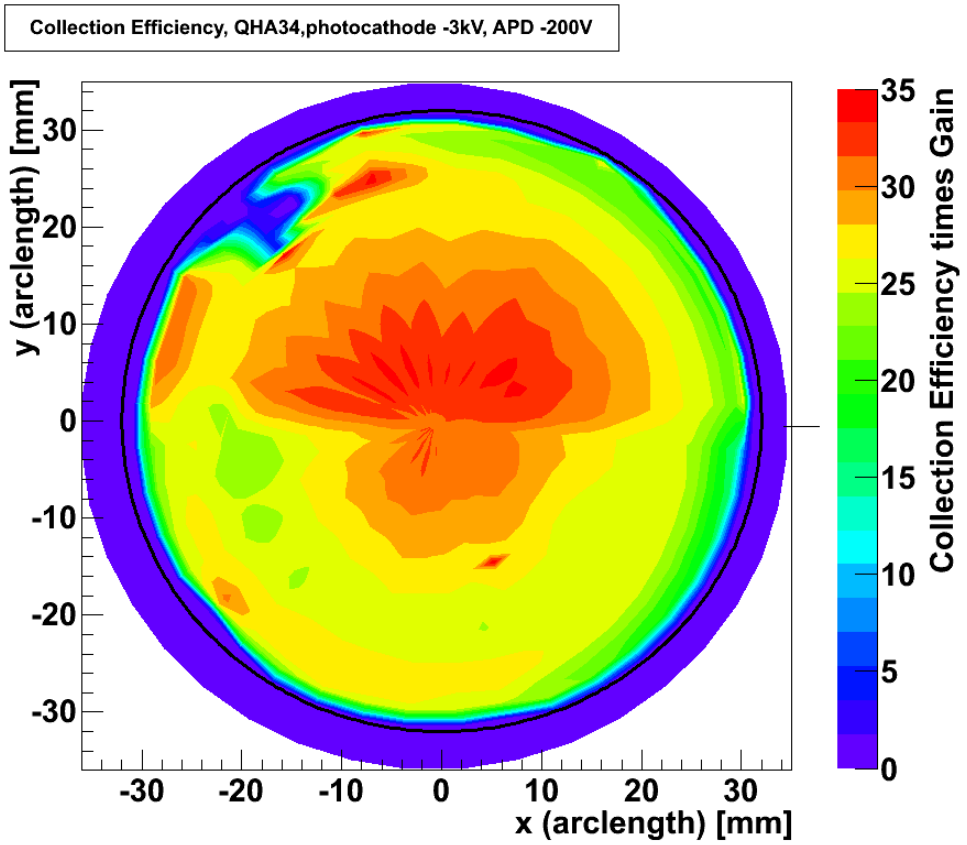

Figure 6.21: Contour plot of the 2 dimensional scan for the collection efficiency times gain

6.3.4 Uniformity of Deformed Developmental QUPID

The first working QUPID that was produced and shipped for testing, model QHP26, was unfortunately not built to specification. The device was shorter than designed and the hemispherical top portion was flattened, the combination of which yielded a very non-uniform charge collection across the photocathode. In figure 6.23, which shows this phototube next to a mechanical sample that was built to specification, it can be seen that it is both shorter and has a more flattened top.

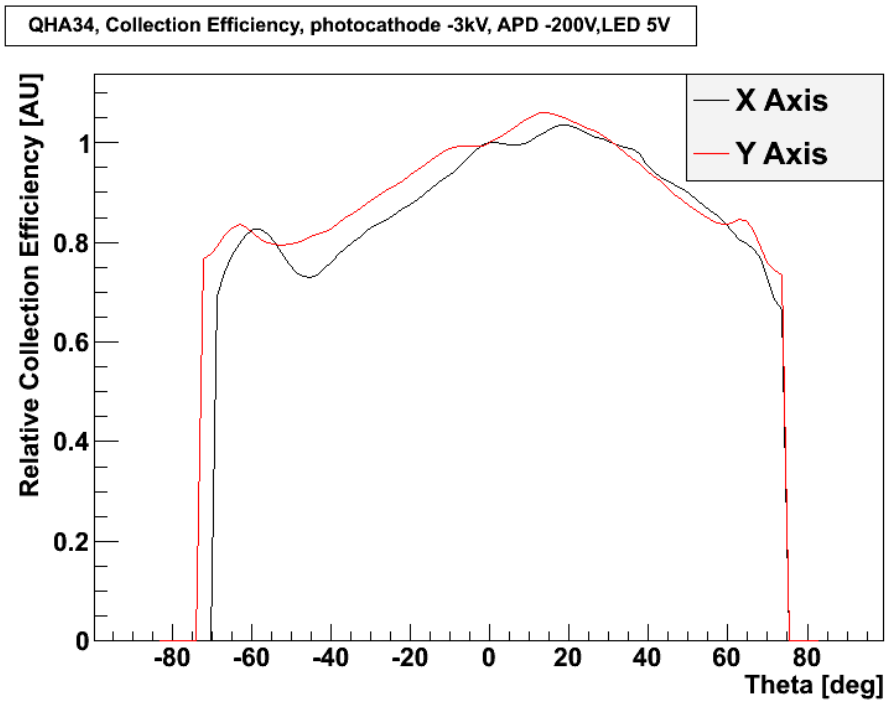

Figure 6.22: Collection efficiency times gain along slices at $\phi = 0°$ and $\phi = 90°$

QHP26 exhibited a very strong nonuniformity when an anode uniformity scan was performed. Figure 6.24 shows the anode current as a function of polar angle along one slice in azimuth, which clearly shows the nonuniformity. The symmetric pattern of the nonuniformity, combined with the obvious deformation of the device, are indicative that poor electron collection efficiency dominates the nonuniformity.

To test whether the nonuniformity of the anode current was due to the deformed geometry or some other effect, a simulation was performed to obtain the electron trajectories for this tube. As the deformation was roughly cylindrically symmetric, this symmetry was still used for the simulation, modelling the main features of the deformation. Figure 6.25 shows how the focusing of the photoelectrons is deteriorated compared to the design shown in 6.5. There is indeed

Figure 6.23: Comparison of a normal mechanical sample (left) and the first working version of the QUPID (right) that was not constructed to specification

a focus point for electrons emitted from the edge of the photocathode well away from the APD, and the trajectories are spread across the surface of the APD, indicating a high likelihood that not all electrons will be collected.

To determine more precicely the collection efficiency as a function of photocathode position, the spread in initial velocity direction distribution was introduced. Since photoelectrons emerge from the photocathode isotropically, a random velocity corresponding to the photon energy (in this case, $3eV$ from the blue LED used in the experiment) minus the work function of the photocathode, and a random direction were assigned in the simulation. The electron trajectories were then calculated for various points on the photocathode. For each point, the fraction of electron paths that entered the APD was found to obtain figure 6.26, which can be compared to the real case shown in figure 6.24.

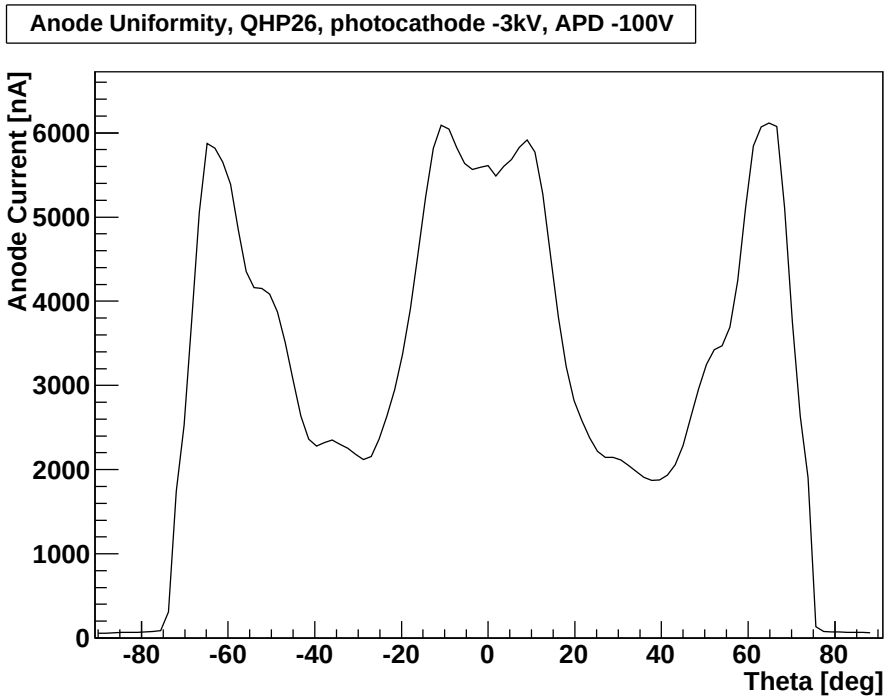

Figure 6.24: Anode current vs polar angle for QHP26 at fixed azimuth showing strong nonuniformity.

6.4 Radioactivity Screening of the QUPID

The entire premise of the QUPID is that it can replace conventional PMTs in low background experiments with significantly less contribution to the background. It was designed on the principle of using ultra clean materials and removing the complicated interiors of a conventional photo tube, but ultimately, the activity must be measured, both to ensure that the device is as radiopure as designed and to find the exact level of the radioactivity.

To measure the activity of the QUPID, four mechanical samples were screened in the GATOR screening facility located in LNGS. The counting facility consists of a germanium gamma detector inside of a cavity measuring $25 \times 25 \times 33$ cm

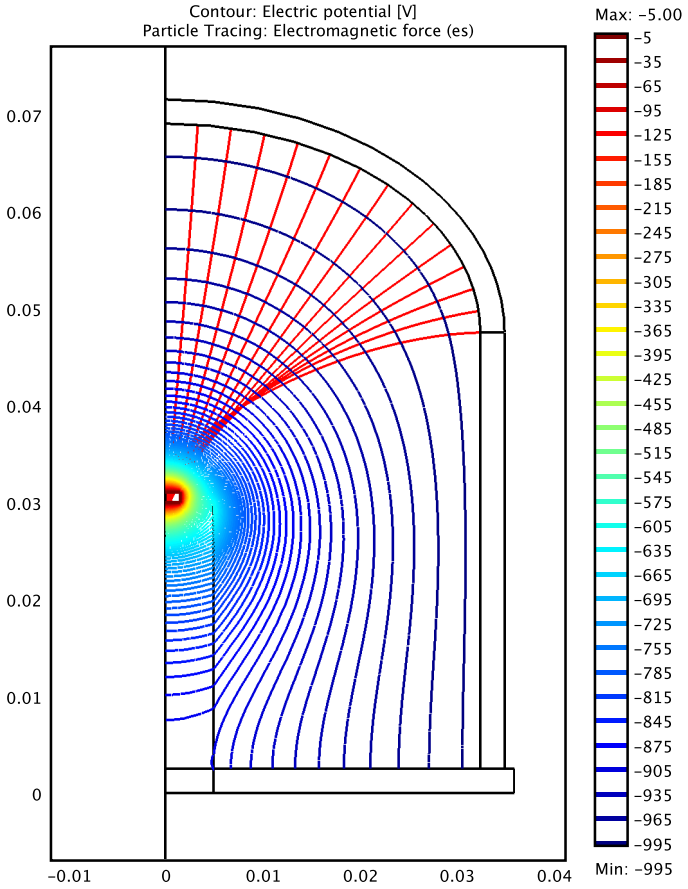

Figure 6.25: Simulation of electron trajectories inside the deformed QUPID QHP26.

surrounded by passive shielding. The shield is composed of 5 cm of copper, then 20 cm of lead. A continuous purge of dry nitrogen gas is blown into the cavity to prevent radon from entering.

To perform a radioactivity screening, the entire gamma spectrum is measured with and without the sample present. The counts at energies corresponding to the lines of decays of the isotopes of interest are obtained, and the activity of each isotope is then derived. The activity A is related to the net number of counts N

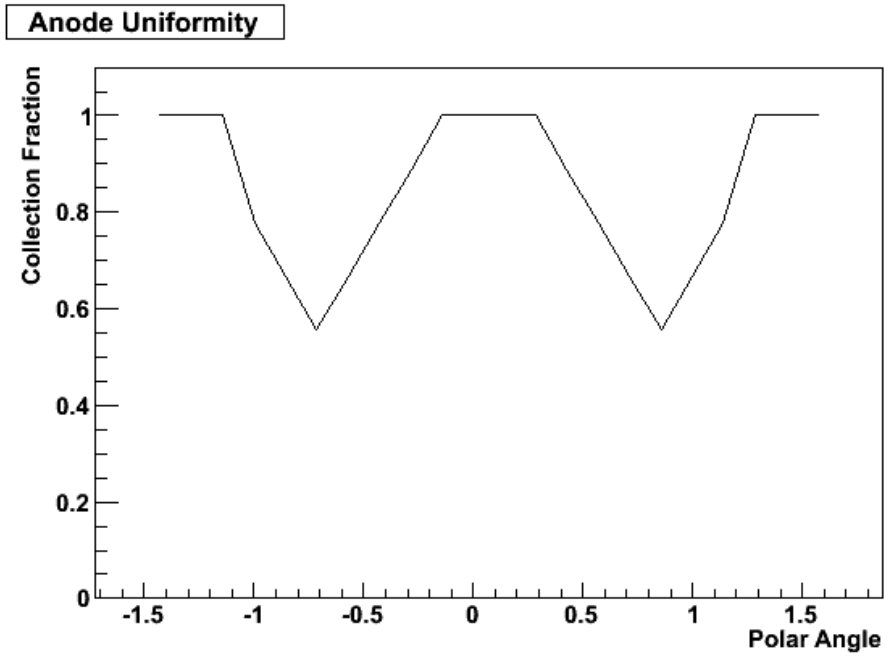

Figure 6.26: Simulated anode uniformity

by,

$$A = \frac{N}{\epsilon \cdot Br \cdot m \cdot t_S} \tag{6.1}$$

where t_S is the live time of the sample measurement, m is the mass of the sample. and ϵ and Br are the detector efficency and branching ratio of the line under consideration. Additionally, the net counts are found by scaling the background counts by the livetimes of the sample and background runs,

$$N = N_S - N_B \times \frac{t_S}{t_B} \tag{6.2}$$

where N_S and N_B are the counts of the sample and background respectively, and t_B is the livetime of the background measurement.

The detector efficiency for each line is found by a monte carlo simulation of the sample inside the detector. This was conducted for four QUPIDs as shown in figure 6.27 to find the efficiencies for lines from the decay chains of ^{238}U, ^{232}Th,

^{60}Co, and ^{40}K. The lines analyzed are listed in table 6.1.

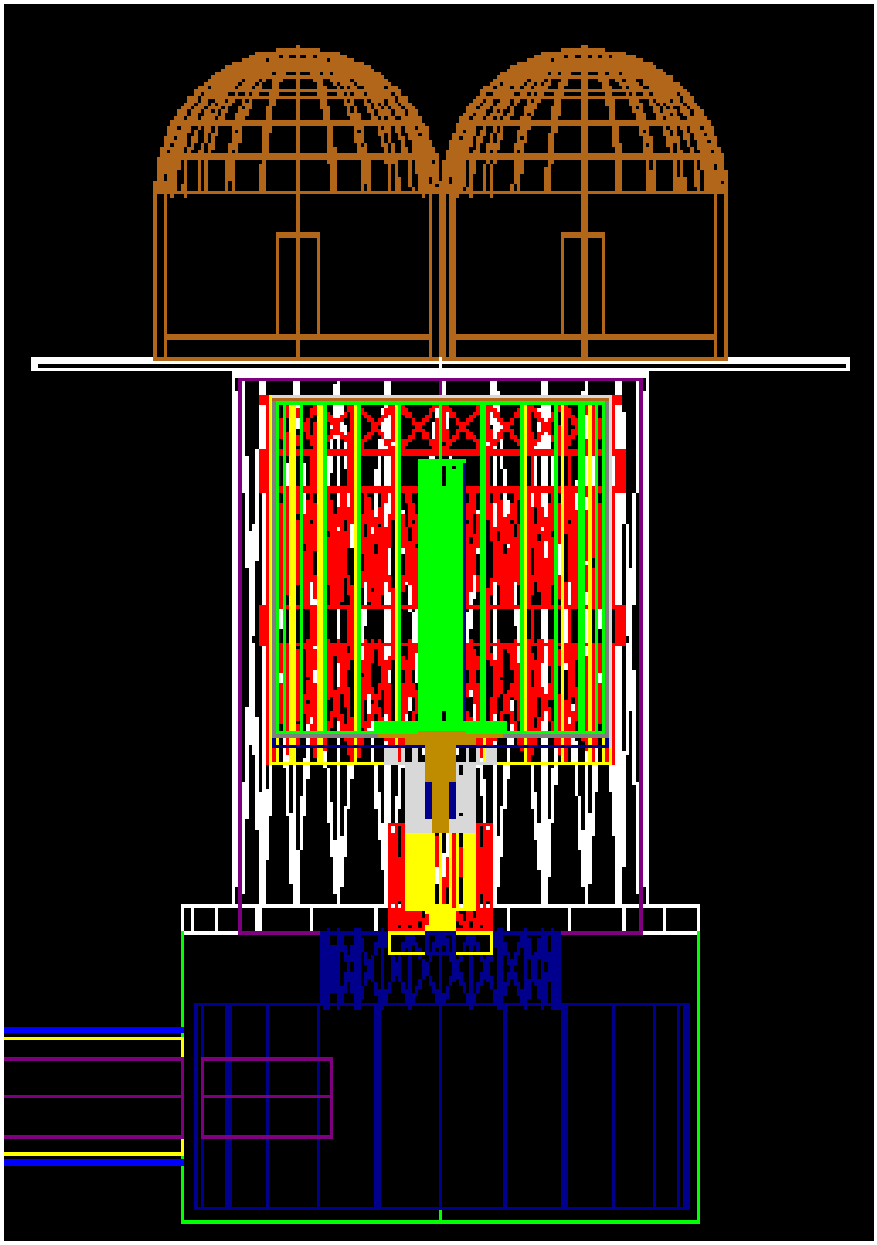

Figure 6.27: Visualization of a simulation to find the detector efficiency for QUPIDs in the GATOR screening facility.

For a low rate measurement such as a radioactivity screening, there are three

Isotope	^{238}U	^{232}Th	^{60}Co	^{40}K
	295	239	1173	1460
Line	352	339	1332	
(keV)	609	911		
	1120	969		
	1765	2614		

Table 6.1: Lines analyzed to determine the activity for each isotope

possibilities for the net count rate given by equation 6.2. The net counts from the screening can exceed the background, be equal to the background, or be less than the background. In the first case, it is straightforward to calculate the activity by using equation 6.1, but in the other two cases, a statistical likelihood analysis, which accounts for the fluctuations in the background, must be performed to determine an upper limit on the activity. There are many different statistical methods that may be used, two of which were chosen for this experiment, a Bayesian method [38] and the Health Physics Society method [24].

Figure 6.28 shows the entire gamma spectrum for both the background and the screening run. Analysis of each line yielded the activities and upper limits shown in table 6.2, as obtained from both statistical methods for both 90% CL and 95% CL. Comparison with table 2.1 shows that the QUPID is at least a factor of 100 more radiopure than a conventional PMT and base, per photocathode coverage, thus confirming that the QUPID can be used for future low background experiments to reduce the internal background substantially. Additionally, the results of this measurement can be used for monte carlo studies of backgrounds in the development of such experiments.

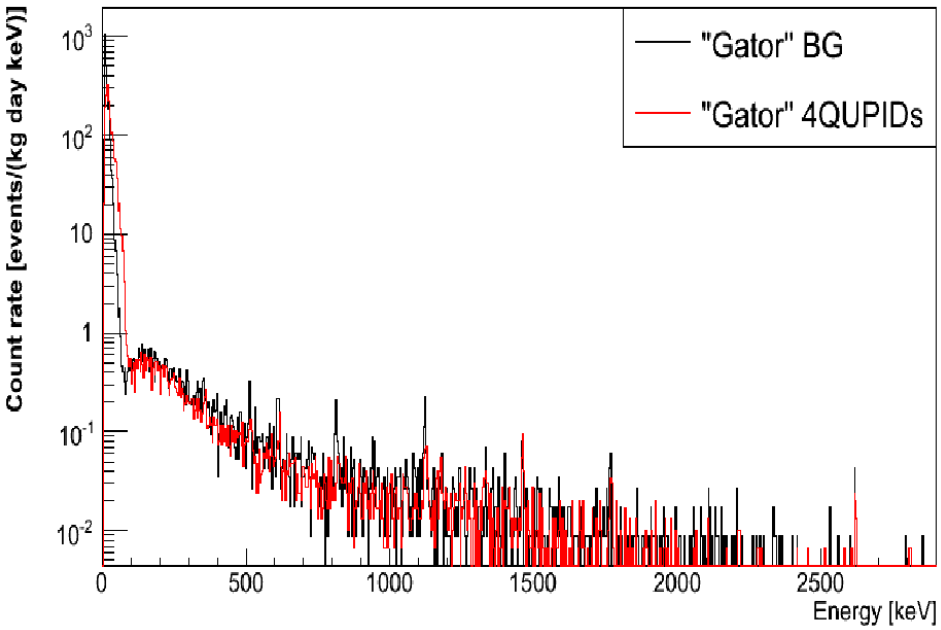

Figure 6.28: Gamma Spectrum for the background and for the screening run with 4 QUPID mechanical samples

	^{238}U	^{232}Th	^{60}Co	^{40}K
Bayesian (90% CL)	< 0.36	< 0.30	0.12 ± 0.06	< 1.96
Bayesian (95% CL)	< 0.49	< 0.40	< 0.21	< 2.40
HPS (90% CL)	< 0.37	< 0.30	0.12 ± 0.06	< 1.96
HPS (95% CL)	< 0.47	< 0.39	0.12 ± 0.06	< 2.34

Table 6.2: Activity of QUPID (in mBq/QUPID) from Bayesian statistics and the Health Physics Society (HPS) for both 90% CL and 95% CL

CHAPTER 7

Simulations for 1 Ton and 10 Ton Liquid Xenon Dark Matter Detectors

7.1 1 Ton and 10 Ton Liquid Noble Detectors

Dark matter detection experiments are currently beginning to probe the predicted phase space for WIMPs, and accordingly are on the verge of either discovering WIMP dark matter or ruling out WIMP models as viable theories. Further, there are great advances in the field, and the next generations of detectors will have dramatically increased sensitivity and probe orders of magnitude deeper into the WIMP cross section. In particular, liquid noble detectors, which are easily scalable, are approaching the ton scale with plans to go beyond as well.

The next phase of the XENON program, which has already been approved and funded, is a 1 ton fiducial detector. Preliminary studies presented here were performed to estimate the light yield and electric field for electron drift for various configurations of PMTs and field shaping techniques.

Additionally, the concept of combining multiple 10 ton scale detectors with xenon and argon targets has been explored [5]. The XAX detector, which is composed of two different 10 ton liquid xenon detectors with separated isotopes, one enriched in ^{136}Xe and the other depleted, and a 10 ton liquid argon detector, has been proposed with an increased scientific scope. At the sensitivity of 10 ton

targets, not only are detectors increasingly sensitive to the WIMP cross section, but new science becomes accessible as well.

Should the WIMP be discovered, the use of both xenon and argon as targets would allow for the measurement of the A^2 dependence of the cross section in equation 1.3.1. The isotope separation of the xenon provides the ability to perform separate measurements of the spin dependence of the WIMP. Additionally, ^{136}Xe is predicted to undergo double beta decay, and, if the neutrino is a majorana particle, meaning it is its own anti particle, it can also undergo neutrinoless double beta decay. Dedicated searches are already underway to detect neutrinoless double beta decay in many materials, such as ^{76}Ge in Gerda and ^{136}Xe in Exo. The sensitivity of a 10 ton liquid xenon dark matter detector enriched in ^{136}Xe is sufficient to perform this search as well. Finally, the solar neutrinos from the pp chain, which are yet undetected, will be measurable by a 10 ton liquid xenon detector as well.

Simulations have been conducted for 1 ton scale and 10 ton scale detectors to explore different options for detector designs. For 1 ton scale detectors, the designs incorporated a 1 m high by 1 m diameter TPC, which, after a 10 cm fiducial cut, has a 1 ton xenon target. For the 10 ton scale detectors, a 2 m high by 2 m diameter target was considered, which gives a 10 ton volume after a 20 cm fiducial cut.

7.2 Electric Field Simulations

The current generation of liquid noble detectors has required delicate work to obtain the uniform drift field inside the TPC that is needed to collect charge from all portions of the active target. In particular, it is difficult to generate

a uniform field in the bottom corner of the detector due to the strong potential gradient outside the bottom of the TPC generated by the proximity of the cathode to other detector components that are held at or near ground. Additionally, great care must be taken to avoid dielectric breakdown and field emission in the detector materials. For the development of 1 ton and 10 ton scale detectors, new approaches have been considered, in addition to conventional techniques, for applying the high voltage necessary to generate the drift field in the active liquid volume and amplification field at the liquid gas interface where the S2 amplification occurs.

Field simulations have been conducted to obtain the electic potential and trajectories of drifted electrons inside the TPC for 1 ton and 10 ton scale detectors. The goal of the simulations was to find detector designs capable of creating a uniform drift field. Additionally, these large scale detector prototypes have been designed with QUPIDs in place of conventional PMTs. Since the QUPID requires a higher operating voltage than a conventional PMT by an order of magnitude, the simulations show how they can be arranged in the high field environments of large scale liquid noble detectors.

There are several design features which were held constant for all of the detector designs considered. In the simulations, the QUPIDs were held at -10 kV. While the current design for the QUPID is for operation at -6 kV, there is a possibility that the final version will be capable of higher operational voltage. Another constant for the simulations is the potential arrangement for the amplification field at the liquid gas interface. The anode is held at -10 kV so that no screening mesh is necessary between the anode and the QUPIDs. There is a wire grid 1 cm below the anode held at -17.5 kV. When the liquid level is maintained halfway between the anode and the lower grid, the relative electric

permeabilities create a field of 10 kV/cm in the gas phase and 5 kV/cm in the liquid phase, which is sufficient for complete electron extraction []. All detector types considered were designed for a drift field of 1 kV/cm, so the cathode high voltage is set at -117.5 kV and -217.5 kV for the 1 ton scale and 10 ton scale detectors respectively.

Additionally, the height of the gas gap is determined by optimization for position reconstruction based on the S2 hit pattern. This is roughly when the gap height is the same size as the PMT spacing, so the gas layer in all the simulations was held at 7 cm, the size of the QUPID. There is effectively zero field between the anode and the QUPIDs, so there is ample room for adjustments to the gap size without affecting the field.

Three design types were considered for 1 ton and 10 ton scale detectors, a conventional design with QUPIDs on top and bottom and a teflon reflector on the side of the TPC, a TPC with full QUPID coverage on the side as well, with a transparent cage of field shaping wires, and a TPC built from an acrylic vessel with QUPIDs on all sides outside of the vessel.

7.2.1 Conventional Field Shaping Design

The first TPC design considered is one based on extrapolating the techniques developed for current detectors to accomodate larger sized detectors. For this type of conventional TPC, with PMTs on top and bottom only, it is fairly straightforward to design a TPC with a uniform drift field using wire grids for the anode and cathode and field shaping rings inside the teflon reflector on the side. The advantage of using such a design is that the techniques are well developed and only need to be modified slightly to support the increased high voltage supplied to the cathode. There are drawbacks, however, particularly since the light col-

lection is limited (see section 7.3), so this design is not well suited for a 10 ton scale detector.

Simulations were performed for a 1 ton scale detector with this conventional design. As in XENON100, the field shaping is implemented by a double layer of field shaping wires embedded within the teflon reflector, one just at the inner radius of the TPC and the other 1 cm deep. There is a 1 cm vertical spacing between each layer of shaping wires, with a 1 kV step between each layer. At the bottom of the TPC, there is a 5 cm gap between the cathode and the bottom QUPID array to prevent shorting between the cathode and the QUPIDs. An additional screening grid may also be necessary between the cathode and the QUPID array, depending on the final geometry used, but this was not included in the simulation.

The field and corresponding electron trajectories for this conventional design are shown in figure 7.1, with zoomed views of the lower and upper corner of the TPC shown in figure 7.2. The equipotentials are very nearly flat just above the cathode at the bottom of the TPC, and the electrons therefore follow nearly straight paths, even near the edge of the detector, thus yielding a very uniform charge collection. The simulation demonstrates that by extrapolating conventional techniques to a 1 ton scale detector, an adequate drift field can be achieved with nearly uniform electron collection from the entire detector.

7.2.2 Full PMT Coverage with Field Shaping Wires

An increased light yield can be achieved by adding PMTs to the side surfaces of the TPC. This, however, complicates the process of generating a uniform drift field, as a transparent field shaping structure must be developed. One way to do this, that is still rather conventional, is to use wire grids for the equipotential

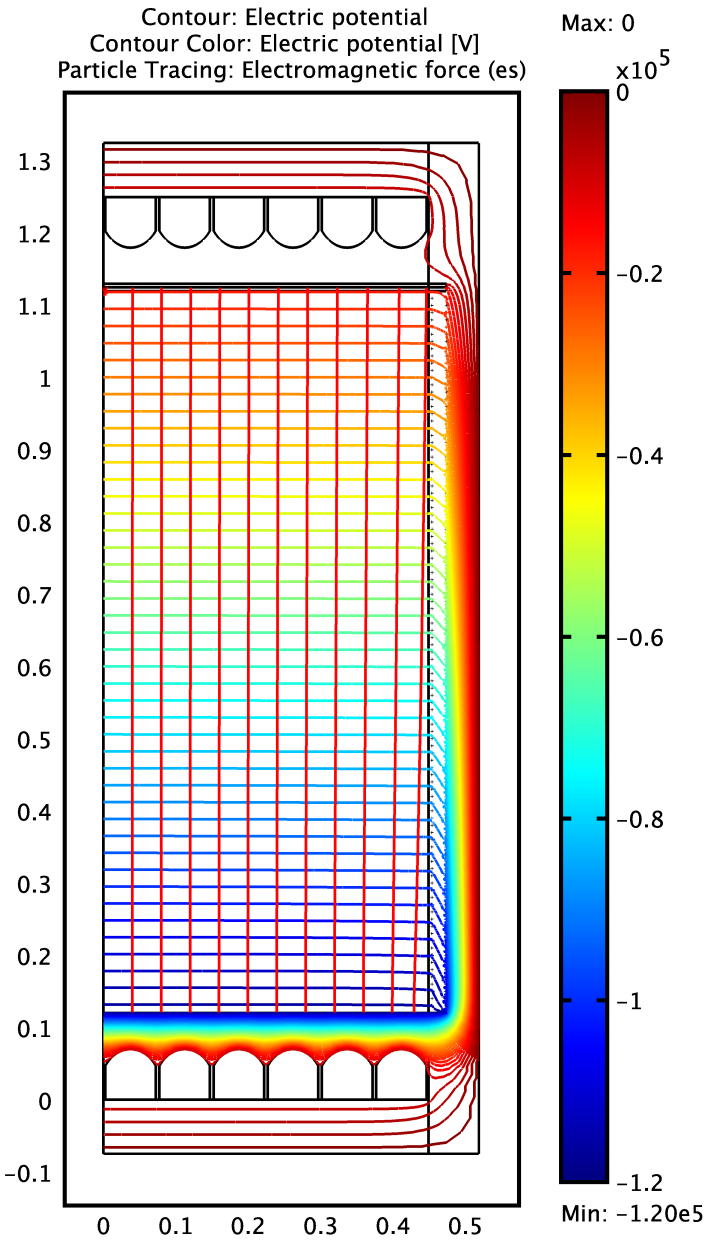

Figure 7.1: Electric potential and electron trajectories for the entire TPC for a conventional 1 ton scale detector

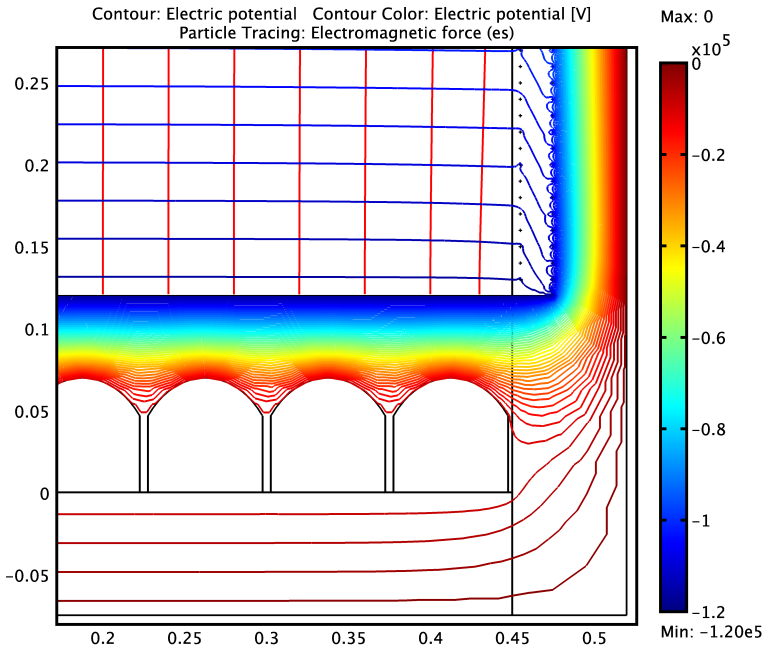

(a) Bottom corner

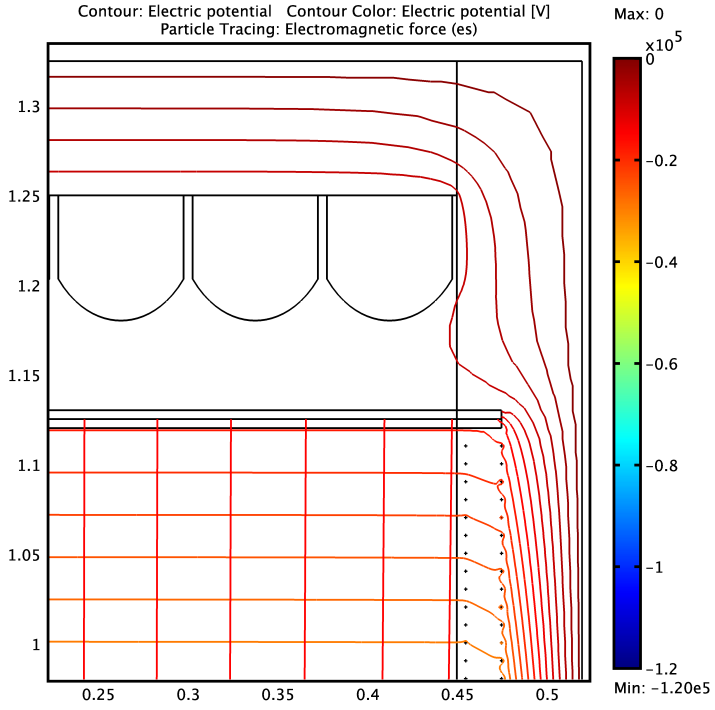

(b) Top corner

Figure 7.2: Zoomed views of the electric potential and electron trajectories for the corners of a conventional 1 ton scale detector

planes as in current TPC designs, and use a thin wire frame mounted inside the side PMT array to shape the field inside the TPC. This is essentially the same method as in current designs but without the teflon reflector to support the field shaping rings. Thus, it is only necessary to develop a new mounting design for the wire cage so that the gaps between the wires remain empty.

In order to effectively shape the field, particularly at the bottom where there is high field leakage between field shaping rings, a double layer of wires is used on the cage with a radial gap of either 1 cm or 2 cm, depending on the specific design. Roughly, the field uniformities penetrate between field rings to a depth equal to the ring spacing, so the radial gap is always set equal to the vertical gap in the simulations. The transparency of the double cage is independent of the radial spacing, and is given by,

$$T = 1 - \frac{2d}{h}, \tag{7.1}$$

where h is the vertical spacing of the shaping wires and d is the wire diameter.

The goal of this design is to construct a field shaping cage with a similar transparency to the grids used for the anode and cathode, namely 95%. However, there are important constraints due to the necessity of a uniform field and minimization of the dead target volume from which no S2 can be obtained.

Two designs were found that yielded a combination of high transparency and high field uniformity in both 1 ton scale and 10 ton scale detectors. The first, which has a transparency of 95%, has field shaping rings constructed from 500 μm diameter wires with a wire spacing of 2 cm. The other uses the same diameter wires with a wire spacing of 1 cm, and while the transparency for this design is only 90%, it yields a more uniform field. As such, both will be compared.

In order to achieve uniform drift fields, the potential assignment on the field shaping rings is somewhat complicated, yet can still be achieved in practice by a

simple resistor chain. The inner layer of rings are set at 1 kV or 2 kV steps for 1 or 2 cm wire spacing respectively. For example, in the 1 cm spacing case, the top most field shaping ring on the inner layer is 1 kV below the screening mesh, the second is 2 kV below, etc. The outer layer has the potentials shifted by one step upward compared to the inner layer, that is, the potential for an outer ring on is equal to the potential for the inner ring one level below. This setup was found by performing simulations on a variety of designs for the field shaping structure, and is the design that gives the most uniform field inside the TPC.

The results for a 1 ton scale detector with 90% transparency are shown in figures 7.3 and 7.4, the latter showing zoomed views of the bottom and top corners of the TPC. These figures show the nearly uniform field and straight electron trajectories for this design. In the zoomed view of the bottom of the detector shown in figure 7.4(a), one can see that the equipotentials are very flat all the way out to the field shaping structure, indicating that the structure shapes the field very effectively even at the bottom of the detector. Although the transparency is relatively low, compared to the 95% optical transparency that is commonly achieved for the wire grids for the anode and cathode, the field uniformity is comparable to that of the conventional TPC design.

For the 1 ton scale detector design with 95% transparency on the field shaping cage, it is much more difficult to obtain a uniform field. Figure 7.5 shows the electric potential and electron trajectories for this design, and zoomed views of the bottom and top corner are shown in figure 7.6. Obviously, the electron trajectories are much more curved than in the 90% transparency case, with the trajectories from the bottom corner curving out of the TPC, indicating a much poorer electron collection uniformity. In particular, the zoomed view of the bottom corner shows how the equipotentials curve sharply toward the edge of the TPC due to the

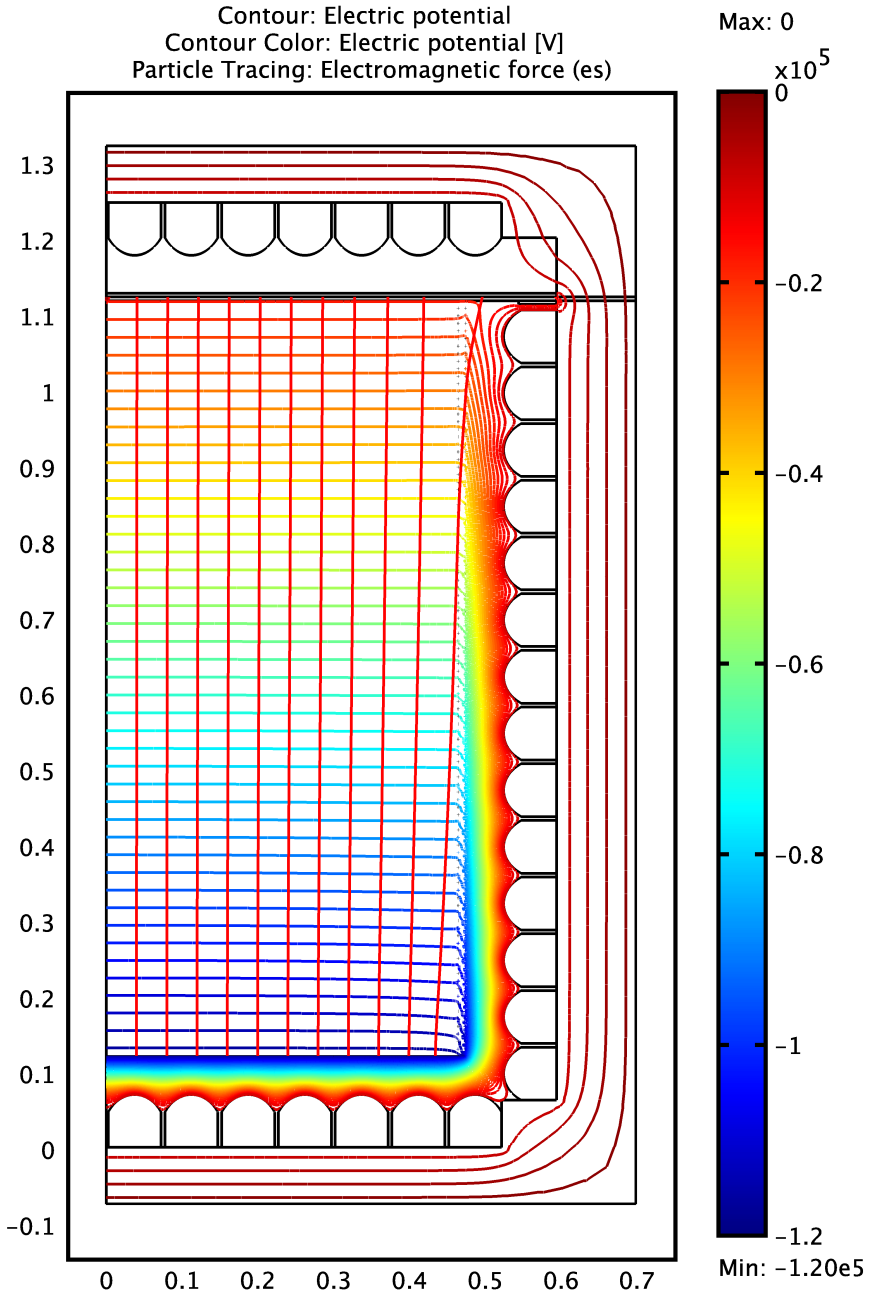

Figure 7.3: Electric potential and electron trajectories for a 1 ton scale detector with 90% transparency on the field shaping cage

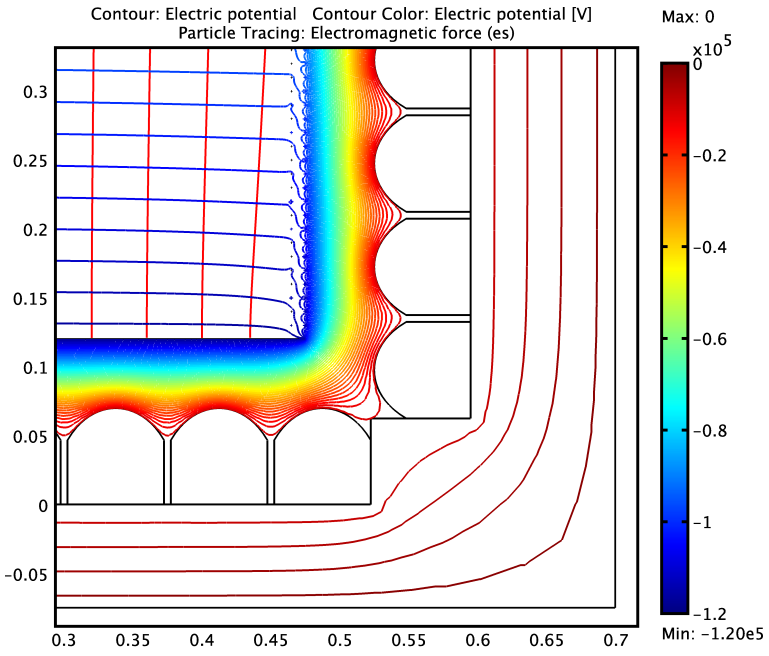

(a) Bottom corner

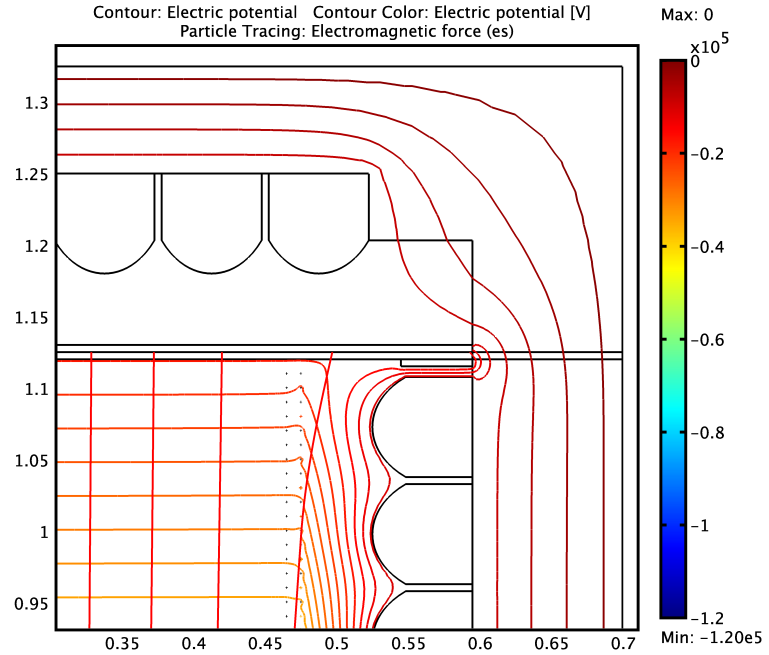

(b) Top corner

Figure 7.4: Zoomed views of the electric potential and electron trajectories for a 1 ton scale detector with 90% transparency on the field shaping cage

strong fringe field, making it impossible to collect electrons at the anode from this region. One additional problem with this design is that the 2 cm radial gap space on the field shaping cage adds a substantial extra dead volume of xenon.

This is certainly not the optimal design for a 1 ton scale detector due to the poor electron collection. It is included here only to show that a 95% optical transparency can be achieved with a somewhat acceptable drift field uniformity. If light yield proves to be the limiting factor for such a design, perhaps compromises such as this will have to be made by utilizing a tighter fiducial cut and using the regions of poor electron collection as a passive shield.

In the case of 10 ton scale detectors, the results are almost identical to the 1 ton scale case. The field and electron trajectories for a 90% transparent field shaping cage are shown in figure 7.7, with zoomed views in figure 7.8. Like the 1 ton scale detector, the field is very uniform and the electron trajectories are very straight out to the edge of the TPC. The zoomed view of the bottom corner shows that the equipotentials remain flat almost all the way to the field shaping cage.

The 10 ton scale detector with 95% transparency, like the 1 ton version, has a marginally acceptable field uniformity. As shown in figure 7.9, the outer electron trajectories curve and leave the TPC before reaching the anode. On inspection of the zoomed views of the corners shown in figure 7.10, one can see that the equipotentials are curved well inside of the TPC, which explains the poor electron collection.

There is, however, one key difference between the 1 ton scale and 10 ton scale detector designs, namely that there is a much larger fiducial cut in the 10 ton case. Because of this, the field non-uniformity may be less critical in the 10 ton case, as events from the bottom corner, where charge collection decreases, will be

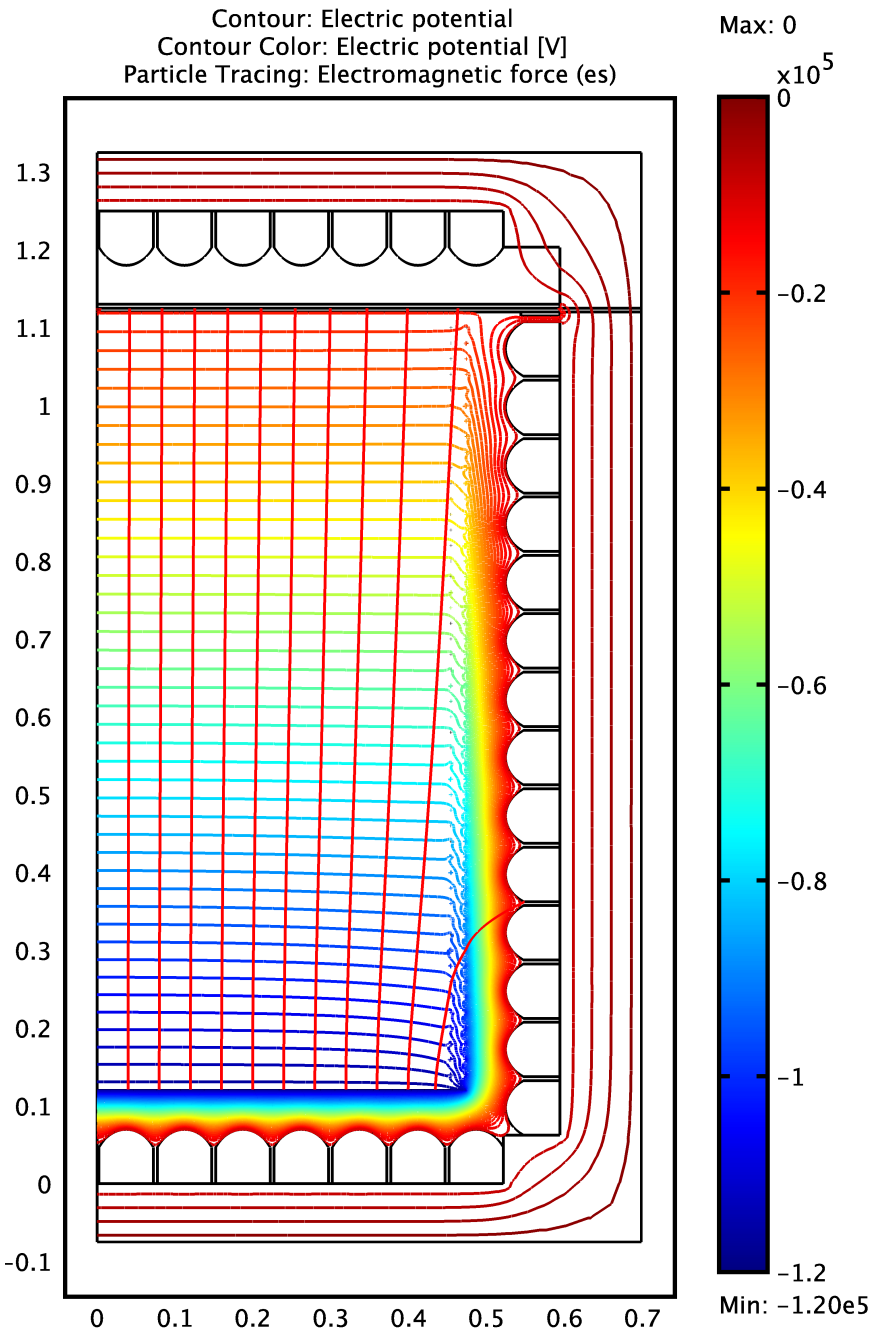

Figure 7.5: Electric potential and electron trajectories for a 1 ton scale detector with 95% transparency on the field shaping cage

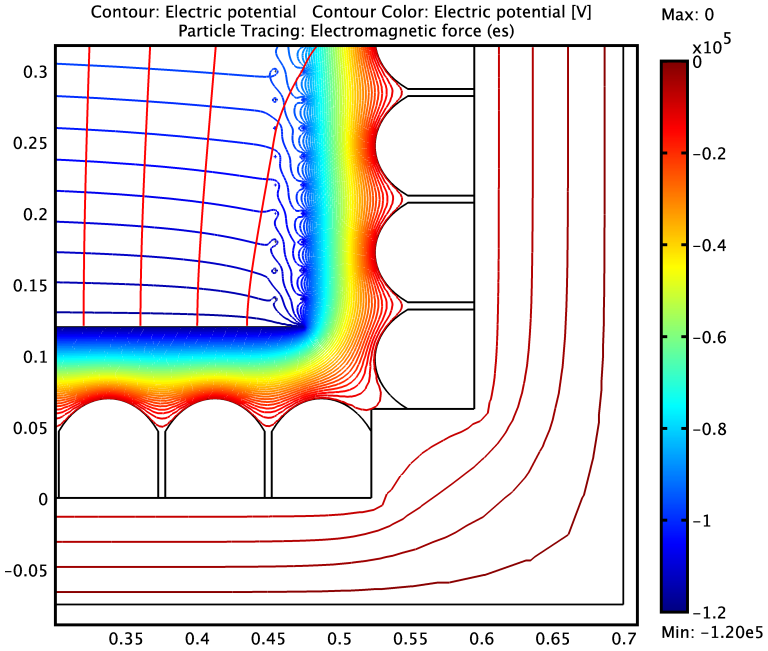

(a) Bottom corner

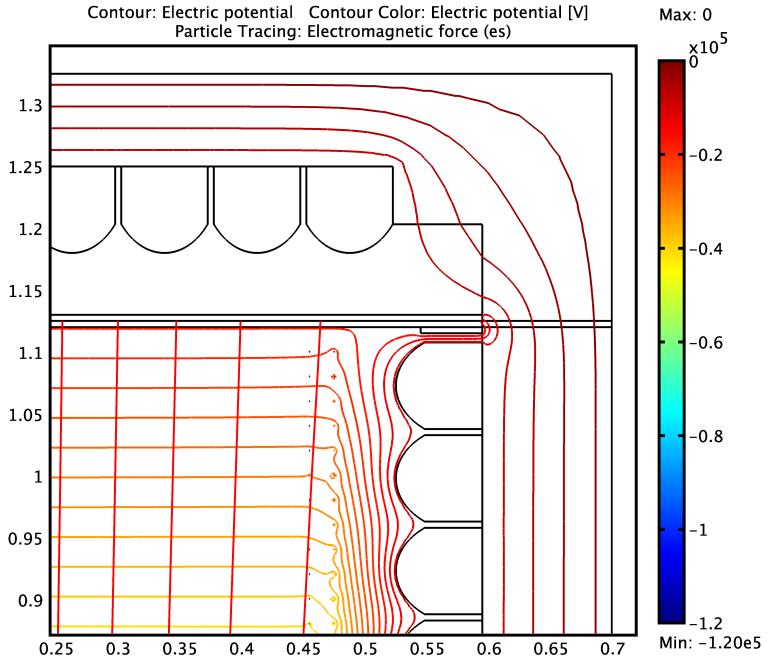

(b) Top corner

Figure 7.6: Zoomed views of the electric potential and electron trajectories for a 1 ton scale detector with 95% transparency on the field shaping cage

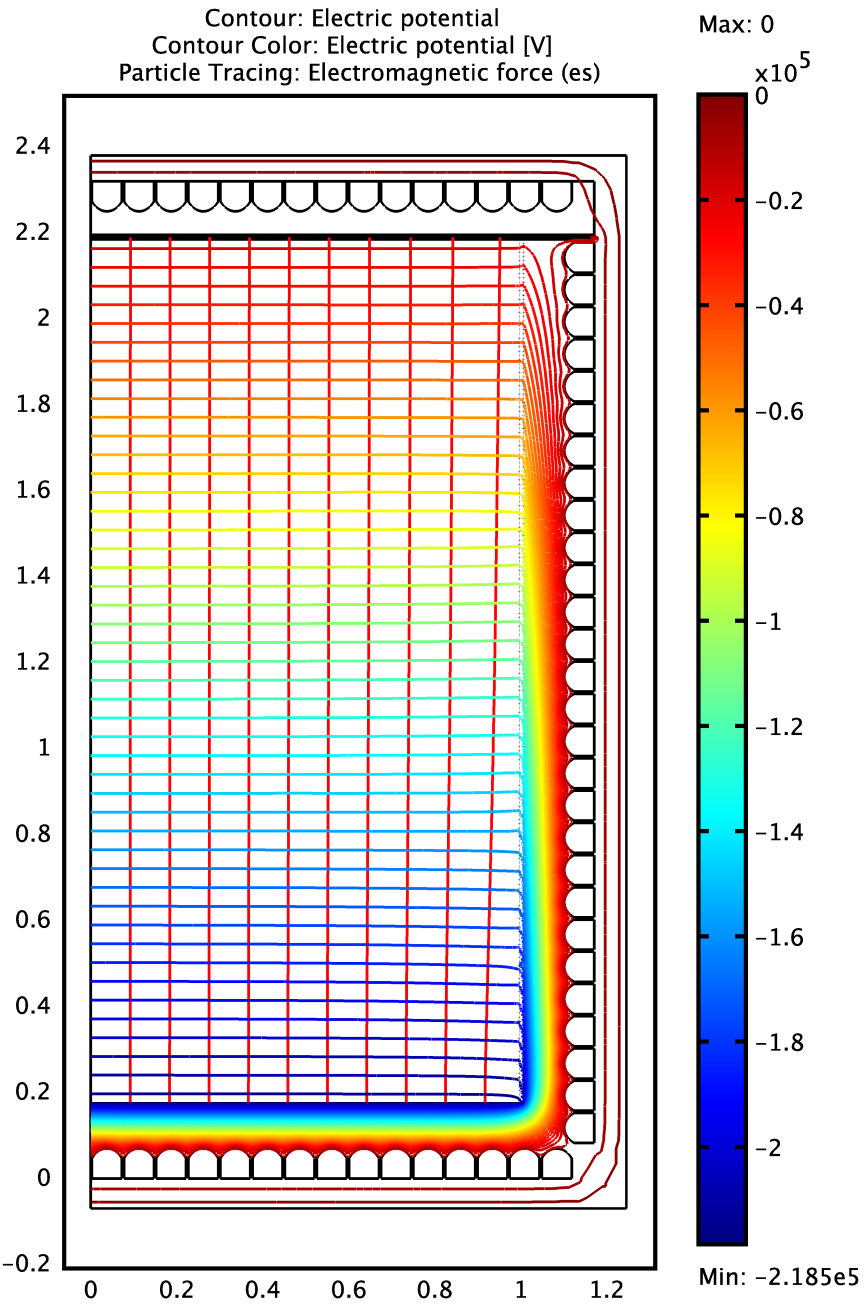

Figure 7.7: Electric potential and electron trajectories for a 10 ton scale detector with 90% transparency on the field shaping cage

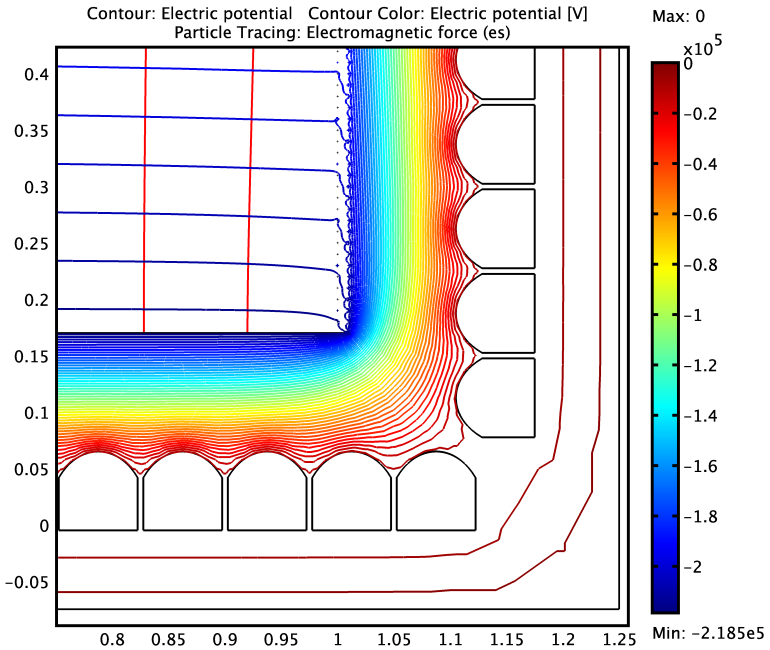

(a) Bottom corner

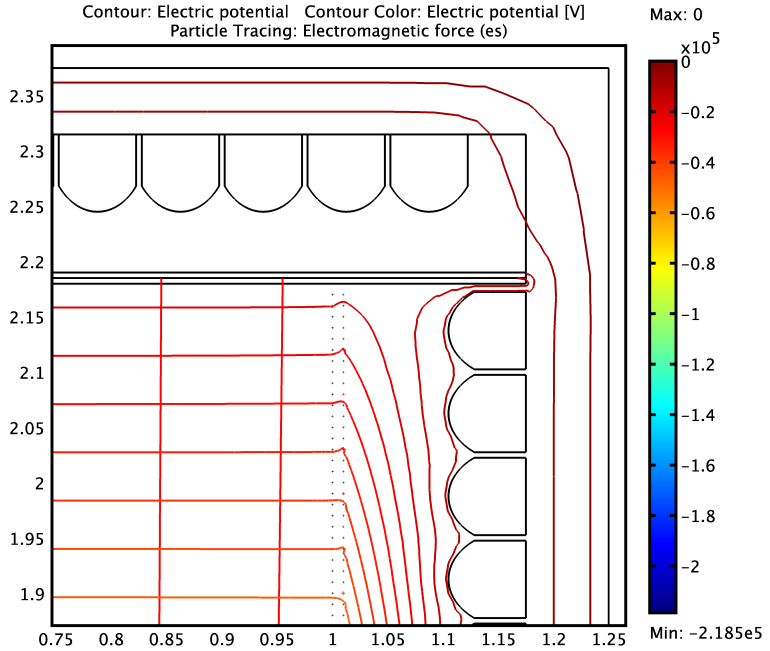

(b) Top corner

Figure 7.8: Zoomed views of the electric potential and electron trajectories for a 10 ton scale detector with 90% transparency on the field shaping cage

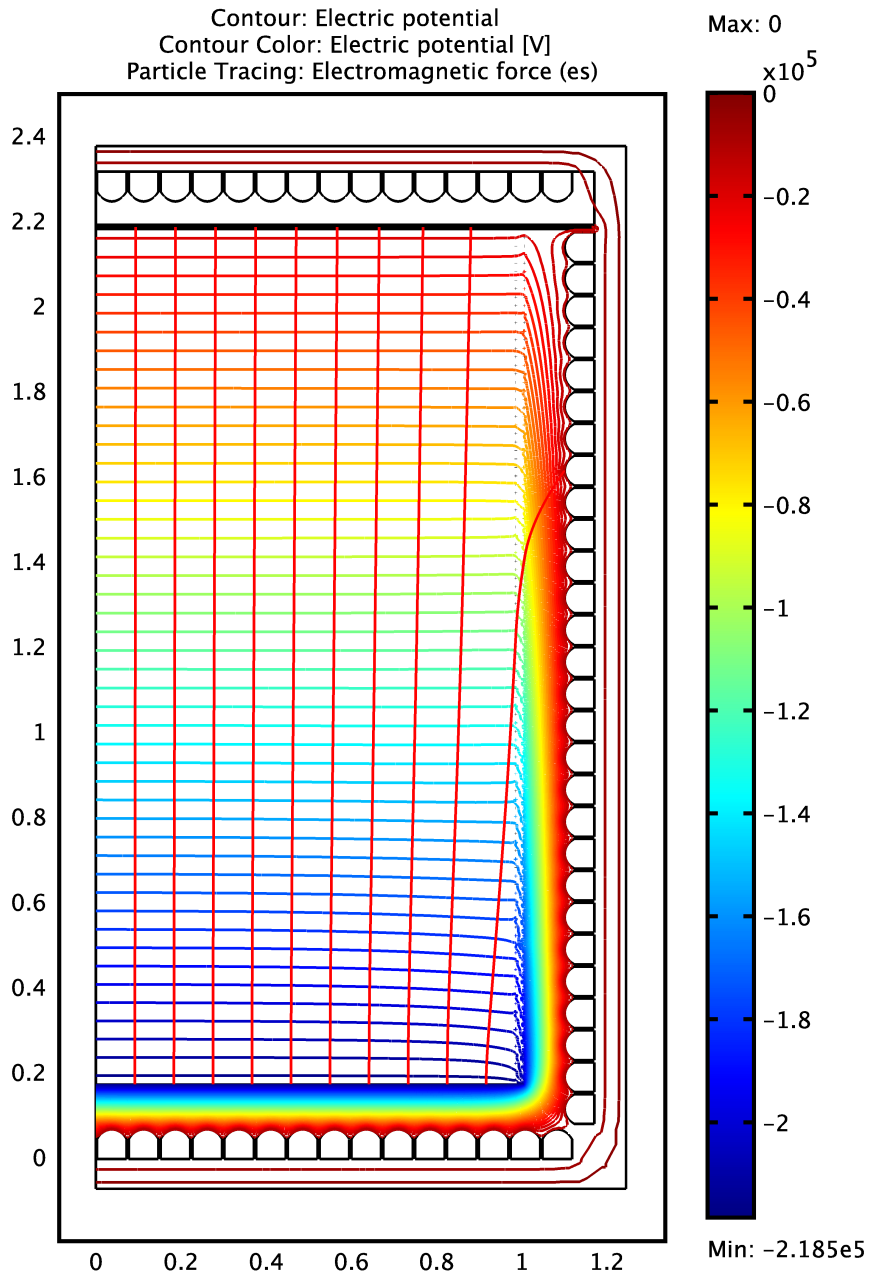

Figure 7.9: Electric potential and electron trajectories for a 10 ton scale detector with 95% transparency on the field shaping cage

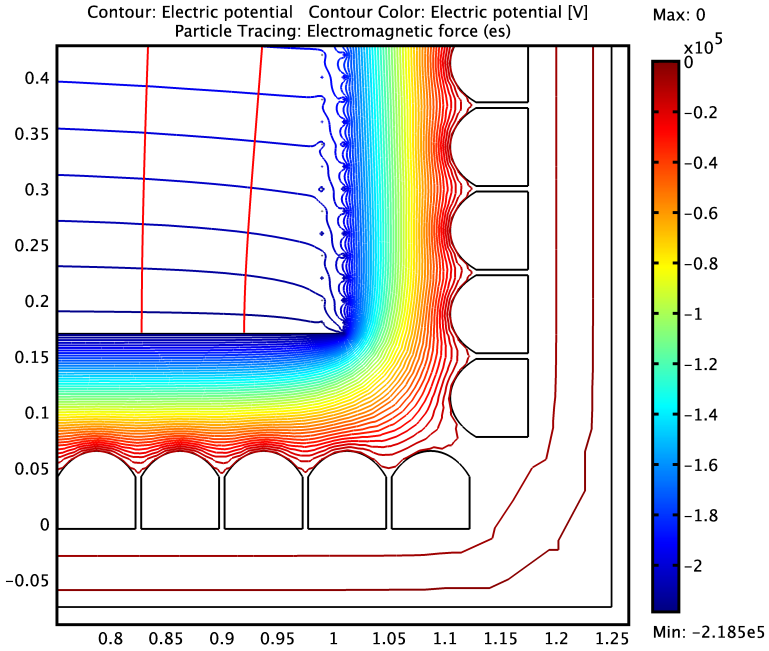

(a) Bottom corner

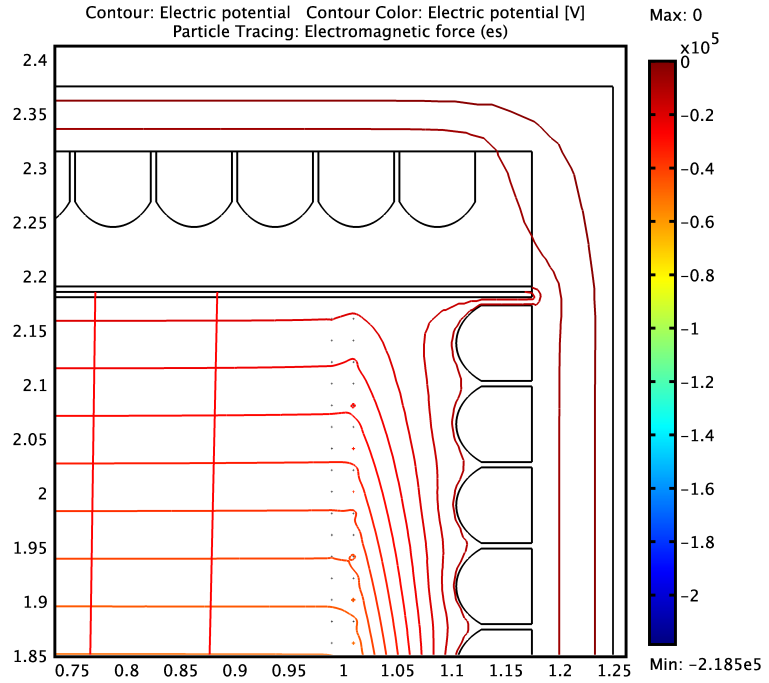

(b) Top corner

Figure 7.10: Zoomed views of the electric potential and electron trajectories for a 10 ton scale detector with 95% transparency on the field shaping cage

cut anyway. But this would still remove the ability to tag events in this region to give a multiple scatter cut, and would instead add to the dead volume.

7.2.3 Acrylic Vessel

A more progressive idea has also been explored which completely changes the design of the TPC. Instead of filling the entire cryostat with the liquid noble target material, an acrylic vessel is inserted into the cryostat and this vessel is filled. It is monitored by PMTs outside of the vessel. The drift field is obtained by painting transparent conductive coatings on the top and bottom surfaces for the cathode and anode, and a transparent resistive coating on the side walls to provide a uniform potential gradient to shape the field. Additionally, since acrylic is not transparent to UV light, the scintillation light must be wavelength shifted to a color for which acrylic is transparent.

Tetra Phenyl Butadiene (TPB) is a common wavelenth shifter used in detectors using argon and helium to convert UV light into blue light at 420 nm [31]. In these systems, the wavelength of the scintillation light is too short to penetrate the quartz windows of PMTs, so wavelength shifting is required to detect the scintillation. This technique can easily be applied to xenon detectors as well. Indium Tin Oxide (ITO) and Antimony Tin Oxide (ATO) are conductive and resistive coatings respectively that are transparent to blue light and can be used to create the cathode, anode and field shaping surfaces [22].

The TPB, ITO and ATO can be painted onto an acrylic vessel as shown in figure 7.11 to create a new type of TPC that can be used for either xenon or argon. The inside surface of the acrylic vessel is painted with ITO on top and bottom for the anode and cathode, and with ATO on the side surface to create the uniform potential gradient. The inner surface of this is then painted with TPB

so that the UV scintillation light from both S1 and S2 is converted to blue light, which can then pass through the ITO or ATO and the acrylic and be collected by the PMTs.

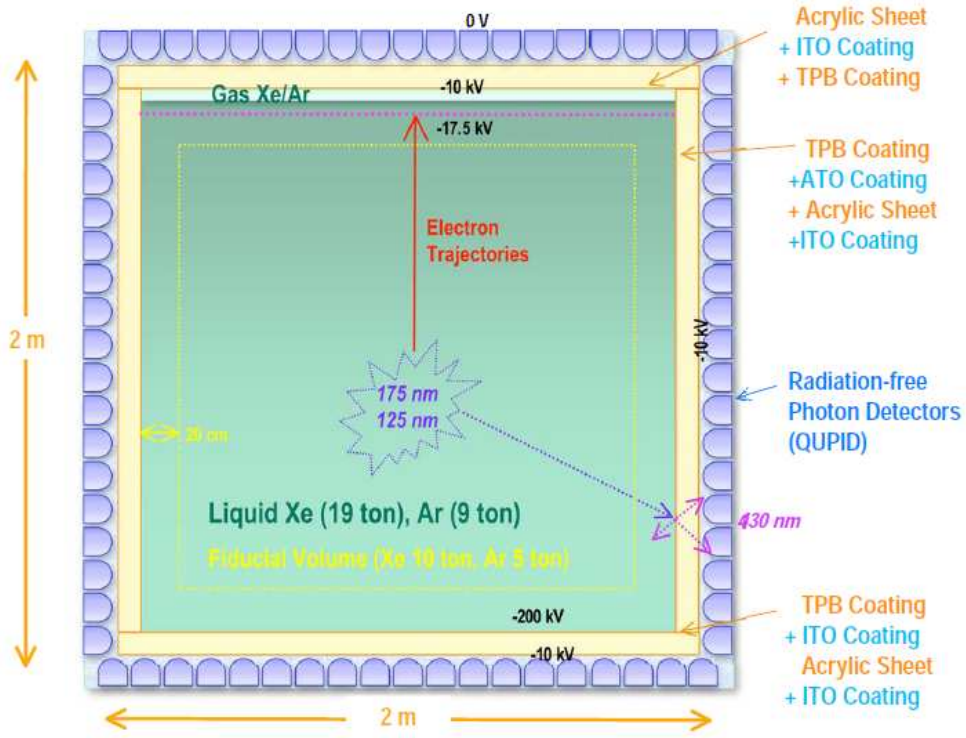

Figure 7.11: Schematic of the acrylic vessel design for a TPC, showing the different materials painted on the surfaces of the acrylic

Figure 7.12 shows the emission spectra for xenon and argon, the absorption and emission spectra for TPB, the transmittance for acrylic, ITO and ATO, as well as the spectrum for the quantum efficiency (QE) of bialkalai photocathodes. This TPC is specifically designed to have high transmission through the conductive and resistive coatings and the acrylic layer and also to have a QE above 40%. The wavelength shifter, which is already necessary for argon detectors, makes the TPC very versatile as it can be used for both argon and xenon, as suggested in the XAX concept, and possibly neon as well.

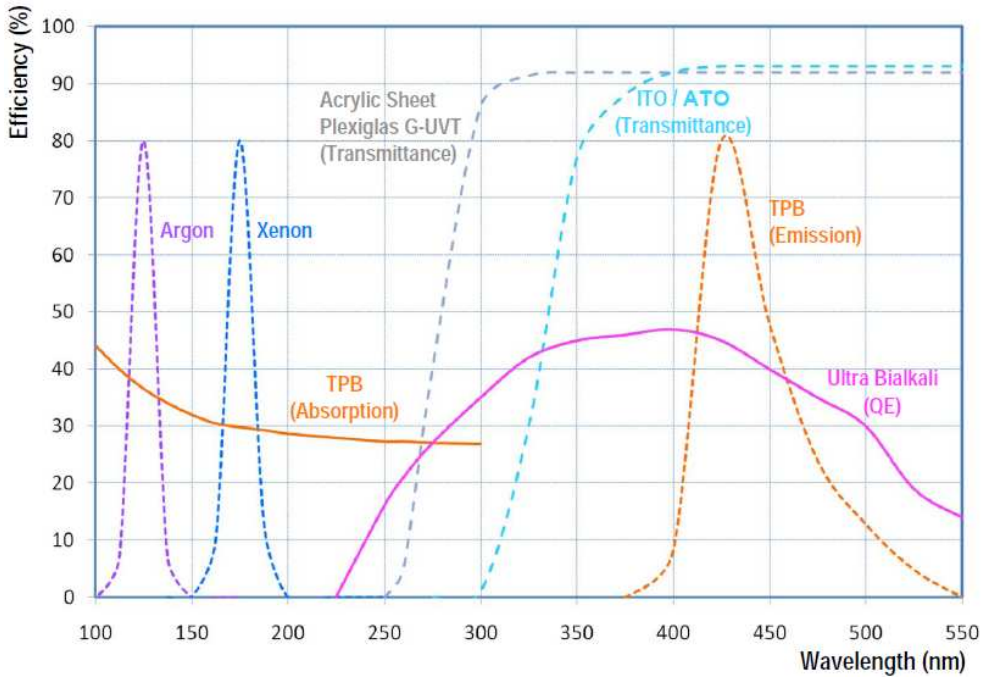

Figure 7.12: Spectra for emission of xenon and argon, emission and absorption spectra for TPB, transmittance for acrylic, ITO and ATO, and QE spectrum for Ultra Bialkali photocathodes.

For the acrylic vessel TPC, there is only one wire gird required for the electric fields. This is the grid just below the liquid gas interface, which separates the drift field and the amplification field. Additionally, the acrylic vessel must be designed to be thick enough to avoid dielectric breakdown in the high field near the cathode.

In the simulation for this design for a 1 ton scale detector, an acrylic vessel 5 cm thick was used, which is sufficient for both structural integrity and to avoid dielectric breakdown. The resultant electric potential and electron trajectories shown in figure 7.13 show that the field is completely uniform inside the detector. This is particularly evident in the zoomed views shown in figure 7.14. Accordingly, the electron trajectories are perfectly straight, and charge can be collected

uniformly from all parts of the detector.

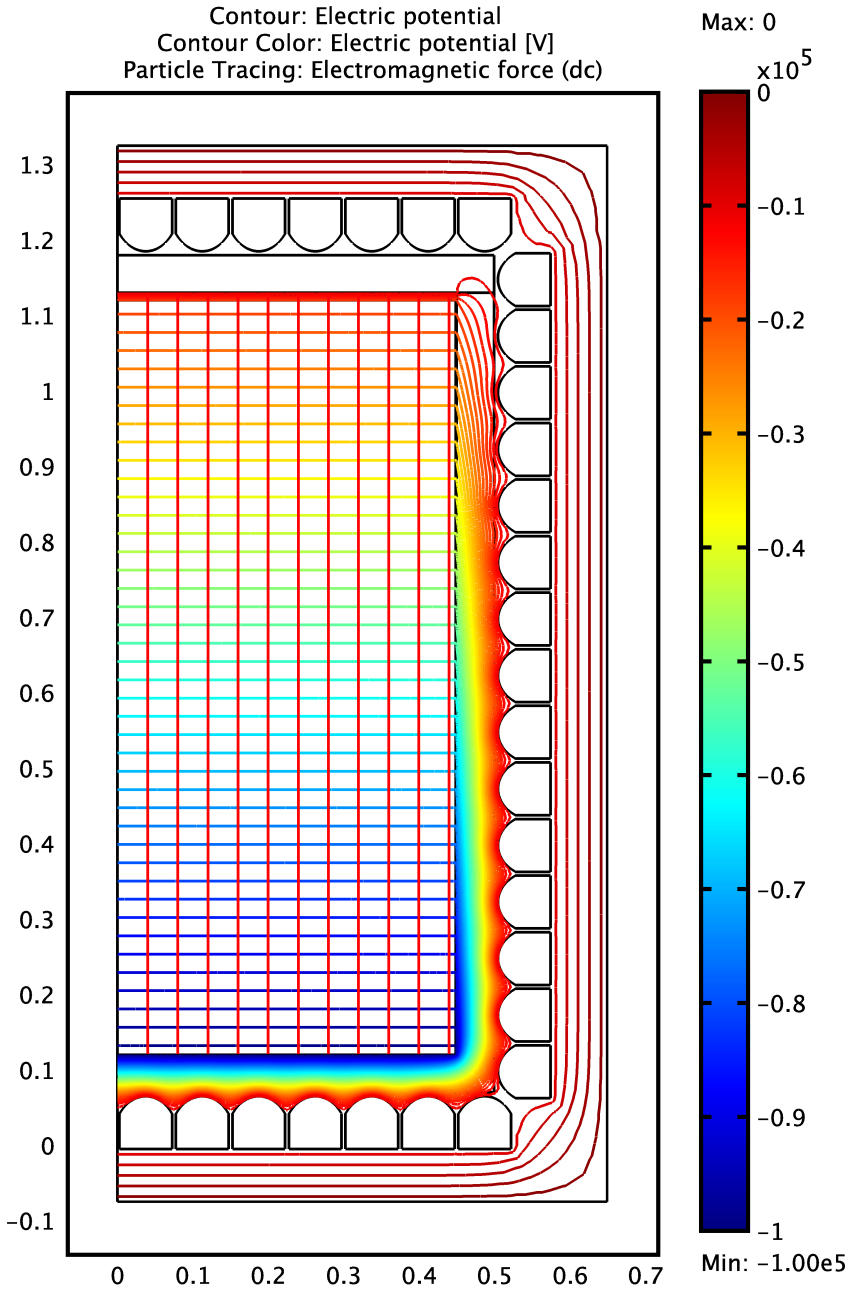

Figure 7.13: Electric potential and electron trajectories for a 1 ton scale detector made from an acrylic vessel

For a 10 ton scale detector, the acrylic vessel must be thicker, both to hold the

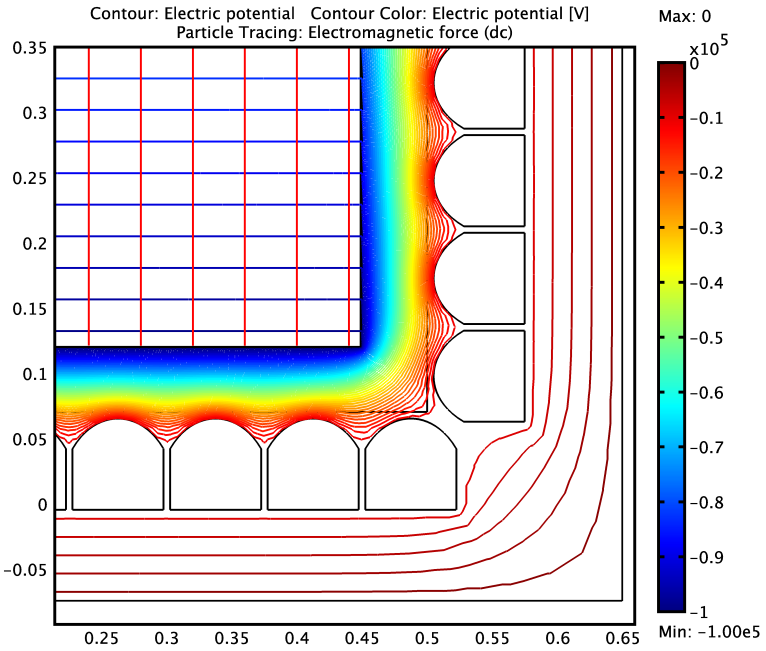

(a) Bottom corner

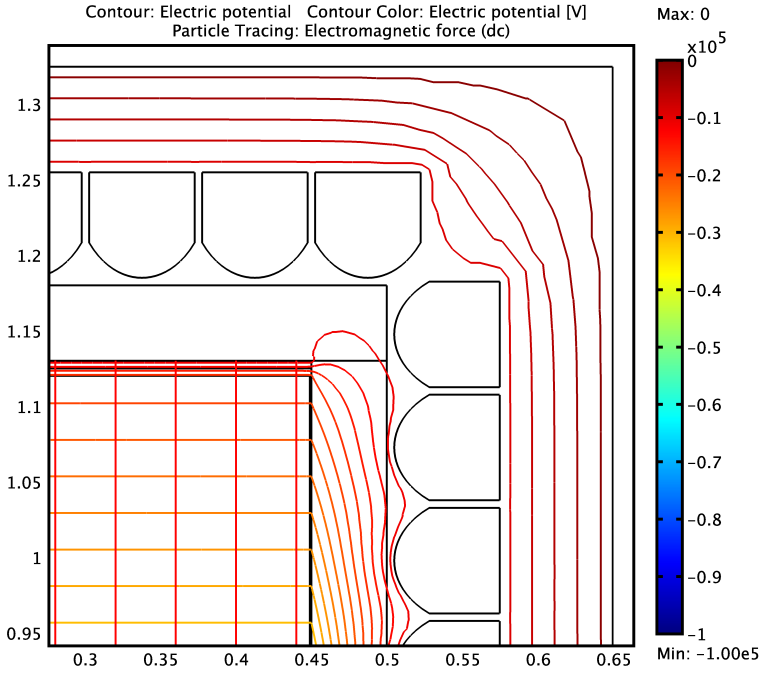

(b) Top corner

Figure 7.14: Zoomed views of the electric potential and electron trajectories for a 1 ton scale detector made from an acrylic vessel

extra weight of the xenon and to avoid dielectric breakdown due to the increased voltage on the cathode compared to the 1 ton case, and the acrylic thickness was thus increased to 10 cm. Figures 7.15 and 7.16 show the results for this simulation for the full TPC and zoomed views respectively. Like the 1 ton scale detector, the field and electron trajectories are completely uniform.

In summary, the three TPC designs each have their strong points and drawbacks. The conventional design, which can easily create a uniform drift field inside the TPC based on current techniques, suffers from a decreased light collection, and will likely only be suitable for a 1 ton scale detector. The transparent field shaping cage can provide a uniform field with 90% transparency, or a somewhat distorted field with 95% transparency. This may be suitable for a 1 ton scale or a 10 ton scale detector, and introduces a minimum of new construction techniques. The acrylic vessel, which provides the best field uniformity for both the 1 ton scale and 10 ton scale detectors, has the most new concepts to be tested. Indeed, these techniques will likely not be suitable for a 1 ton scale detector, as such an experiment is already being developed, but may be well suited for a 10 ton scale detector.

7.3 Light Yield Studies

7.3.1 Light Attenuation

Since liquid noble detectors must achieve an extremely low energy threshold of a few keV to search for dark matter interactions, they are designed with as high a light yield as possible. While liquid noble gases in principle do not absorb their own scintillation light, trace amounts of electronegative impurities give rise to a

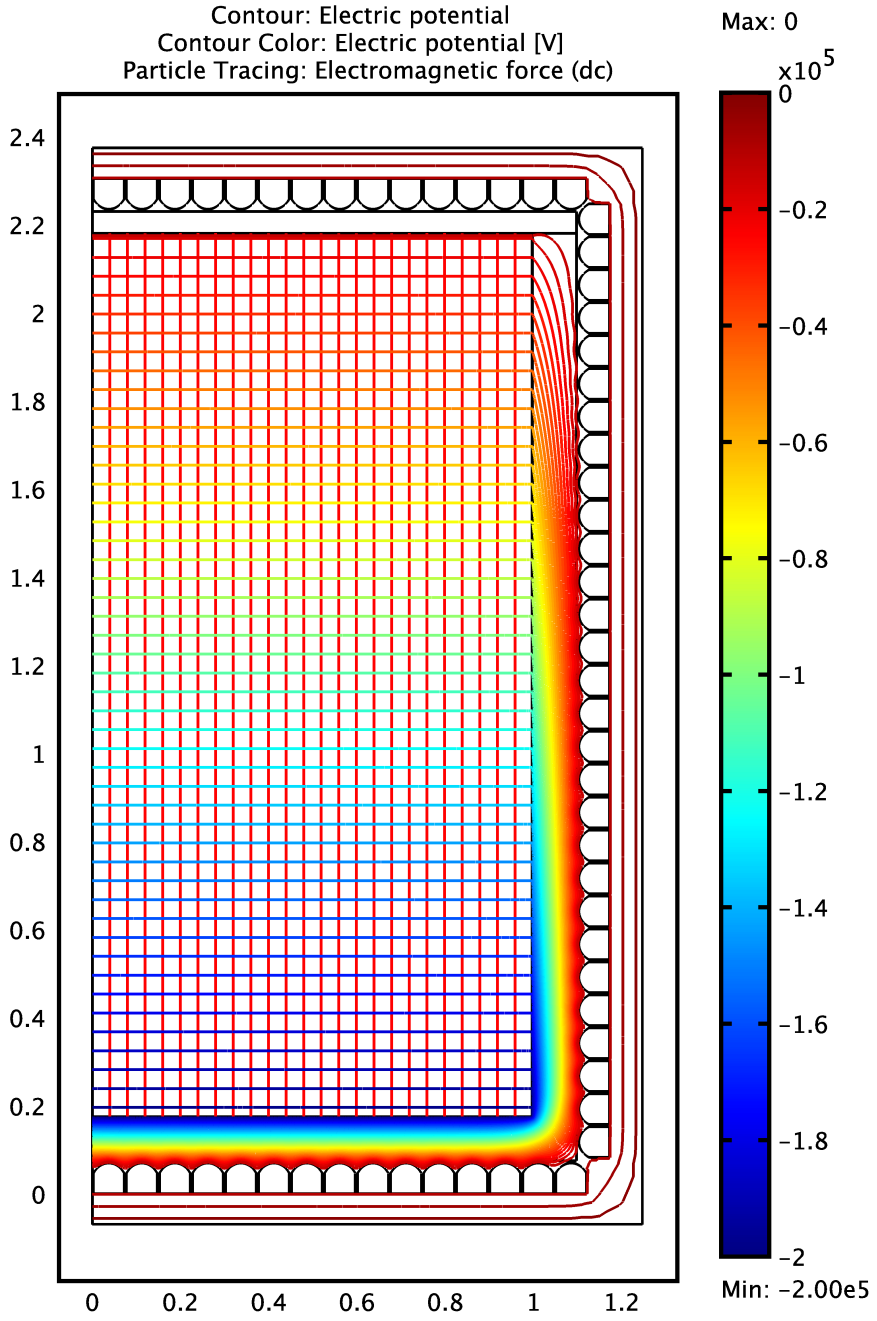

Figure 7.15: Electric potential and electron trajectories for a 10 ton scale detector made from an acrylic vessel

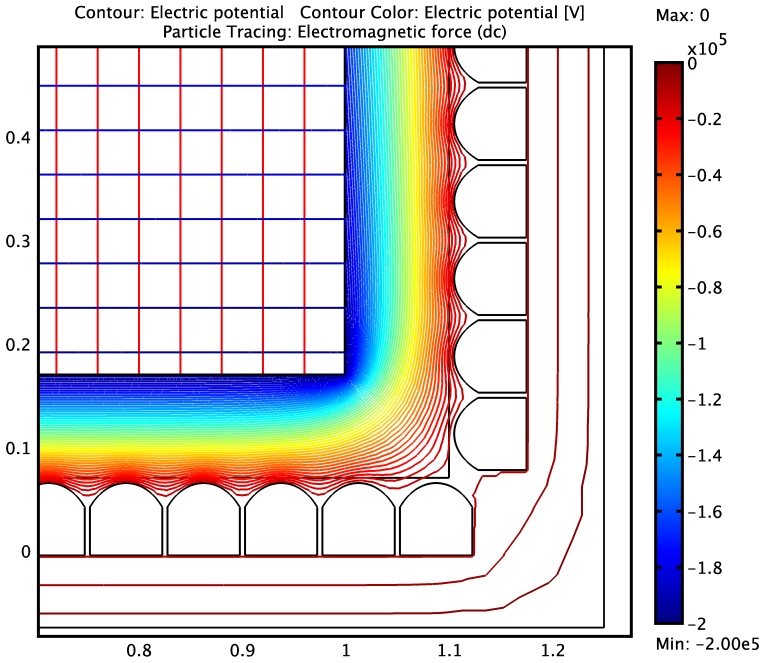

(a) Bottom corner

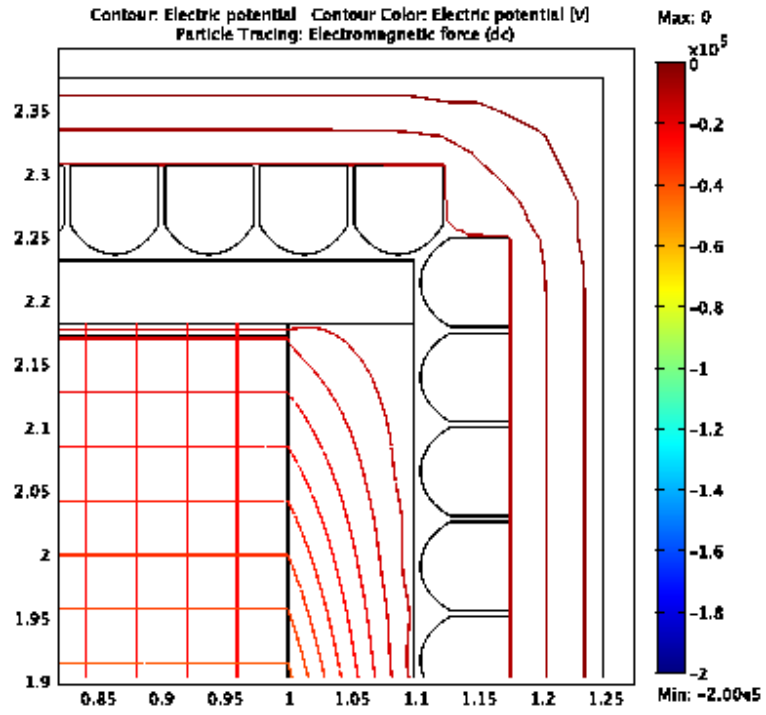

(b) Top corner

Figure 7.16: Zoomed views of the electric potential and electron trajectories for a 10 ton scale detector made from an acrylic vessel

finite attenuation length in the liquid. The attenuation is given by,

$$A = A_0 e^{-x/x_0} \tag{7.2}$$

where A_0 is the original intensity, A is the intensity after travelling a distance x, and x_0 is the attenuation length. Several phenomena contribute to the attenuation length. Those important here are the absorption length λ_A and the Rayleigh scattering length λ_S, from which x_0 is obtained through the relation,

$$\frac{1}{x_0} = \frac{1}{\lambda_A} + \frac{1}{\lambda_S}. \tag{7.3}$$

The Rayleigh scattering length for liquid xenon is calculated to be 30 cm [35] and is measured to be between 29 and 50 cm [25] [10] [11]. The absorption length, which depends greatly on the level of impurities in the xenon, can in principle be extended indefinitely as purification techniques are improved. In practice, absorption lengths nearing at least 3 meters have been measured [26].

An additional source of light attenuation in the detector arises from the imperfect reflection of the UV light off of the teflon surface. For UV light, reflection off of teflon is known to have both specular and diffuse components. The diffuse component gives rise to much longer path lengths for scintillation light when it reflects off of the teflon. Further, the reflectivity of the teflon is less than 100%, so a finite fraction of photons that hit the reflector are absorbed.

One final consideration for light attenuation in the TPC is the wire grids used for the drift field. They are typically 90 to 95% transparent, so the presence of the several grids necessary to produce the correct fields for electron drift and S2 amplification substantially affects the total light yield.

7.3.2 Simulation Parameters

For the light yield studies of 1 ton and 10 ton detectors, a simulation was developed that could easily be scaled to different detector sizes. Instead of writing a detailed simulation of the entire detector, a simple geometry of the inside of the TPC was created, which is valid for the light simulations, and yet is also flexible for varying the size of the detector or the type and placement of PMTs.

The key parameters for the simulation, which address the sources of attenuation listed in section 7.3.1, are the Rayleigh scattering length, absorption length, teflon reflectivity and placement of field shaping grids. The values scanned for these parameters are shown in table 7.1. Additionally, the placement of the PMTs was varied to account for TPCs with PMTs on the top and bottom only and for TPCs with PMTs on the side as well.

Parameter	Range	Unit
Rayleigh Scattering	30 - 50	cm
Absorption Length	0.5 - 20	m
Teflon Reflectivity	90 - 100	%

Table 7.1: Parameters for Monte Carlo Simulation.

All PMT arrays were assumed to have 90% photocathode coverage, with the spaces between filled with PTFE. Both flat faced PMTs, such as the Hamamatsu R8520 used in XENON100, and spherical faced PMTs, like the QUPID, were simulated, but no significant difference in the light yield was found. The grids and field shaping cage were modeled by introducing a thin layer of finite optical transparency, with 95% transparency on the grids and 90% transparency on the field shaping cage, consistent with the more conservative case of a field shaping structure considered in section 7.2.2.

Like in the electric field simulations in section 7.2, the light yeild simulations are for 1 ton scale detectors measuring 1 m high by 1 m diameter and 10 ton scale detectors measureing 2 m high by 2 m diameter.

7.3.3 Results of Light Yield Studies

In a real detector, there are light yield non-uniformities due to the details of the detector construction. As these are very dependent on the specific design of the real detector, they are not of particular interest in this study. Instead, large scale trends on the absolute light yield are desireable. Of particular interest is the light yield at the center of the detector, and as a function of height in the detector. Due to the high index of refraction in liquid xenon, there is substantial total internal reflection at the liquid gas interface. Thus, the darkest portion of the detector may not be the exact center, but rather shifted toward the top. Radial trends are not considered, as the measured radial dependence is not strong in real detectors, and since this is grossly dependent on the particulars of the physical detector.

Two cases were considered for both 1 ton scale and 10 ton scale detectors. The first is a conventional TPC design with PMTs on top and bottom only and a teflon reflector on the side, and the second is a TPC with PMTs on the side as well for full coverage, with a field shaping cage inside the TPC.

No strong dependence was found on the Rayleigh scattering length until it is extended to 1 m or more, which is far beyond the measured and calculated values. Similarly, there was no significant dependence on the PTFE reflectivity found in the ranges considered, the variations being a only few percent. Thus, the results presented here are for a 50 cm Rayleigh scattering length and a 95% PTFE reflectivity.

Figure 7.17 shows the light yield at the center of a 1 ton scale detector as a function of vertical position. The light yield is shown for the top and bottom arrays separately, as well as for the sum. The bottom array indeed collects much more light than the top array nearly to the top of the detector, which is consistent with the strong total internal reflection. A strong dependence on the absorption length is observed. Since this is a function of xenon purity, the absorption length can in principle be extended indefinitely by improved purification techniques. Even assuming that good purity increases the absorption length to 5 m, the light collection for this design is limited to 2 pe/keV at the dimmest part of the detector.

Such a light yield is certainly on the border of acceptable at best, as compared to an average light yield of 3 pe/keV in XENON100. Presumably, to achieve a low energy threshold with this design, great care would have to be taken to ensure a maximum xenon purity, thus extending the absorption length and increasing the light yield. However, as 1 ton scale detectors are currently being developed, and since the conventional TPC design is well established and PMTs are expensive, this may be a suitable option.

However, by adding PMTs on the side of the detector as well, a sharp increase in the light yield is observed. Figure 7.18 shows the light yield at the center of a 1 ton scale detector with PMTs on all sides, again showing the collection of the separate detector arrays and the sum. For this detector design, the side PMTs collect the most light for all regions except very near the bottom of the detector. The net affect is an increase in the light yield to 3 pe/keV at the dimmest part of the detector, a 50% increase compared to no PMTs on the side.

A similar trend is found for 10 ton scale detectors, but with a decreased absolute light yield due to the larger detector size. Figure 7.19 shows the light

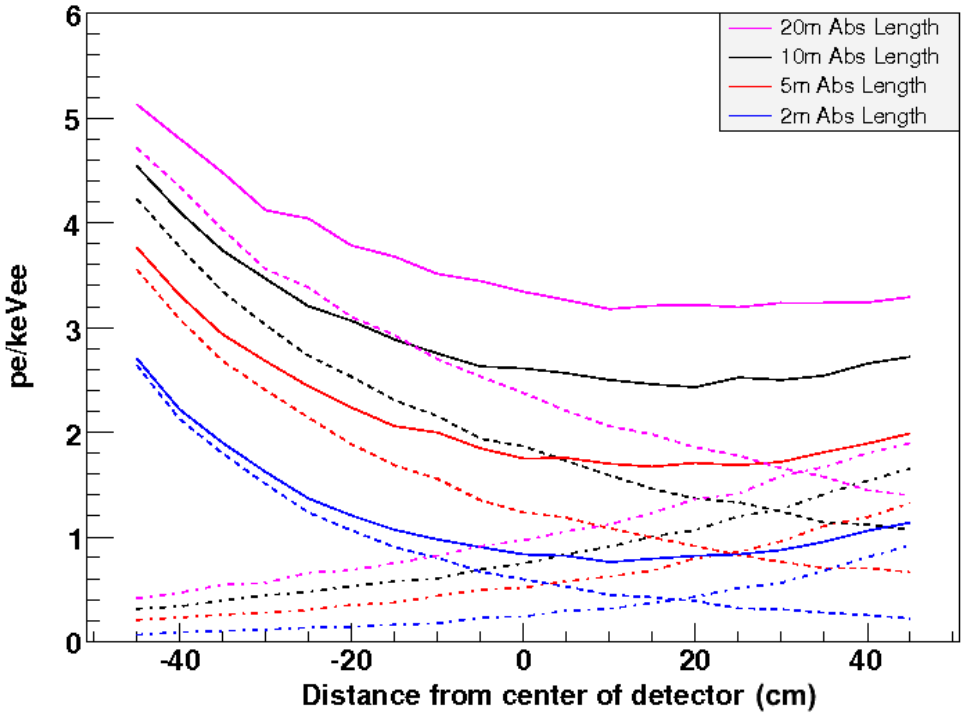

Figure 7.17: Light yield at the center of a conventional 1 ton scale detector with PMTs on the top and bottom only as a function of height in the detector for different absorption lengths, showing the light yield for the top (dashed) and bottom (dotted) arrays and the sum (solid).

yield at the center of a 10 ton scale detector with PMTs on the top and bottom only. Again, the majority of the light is collected by the bottom PMT array. For this design, even assuming a 20 m absorption length the darkest part of the detector still has less than 3 pe/keV. Thus, this detector design is not well suited for a 10 ton scale detector, and a design that includes PMTs on the side of the TPC must be considered.

The light yield for a TPC for a 10 ton scale detector with PMTs on all sides is shown in figure 7.20. With this configuration, an absorption length of 5 m yields 2 pe/keV at the darkest part of the detector, similar to the situation for

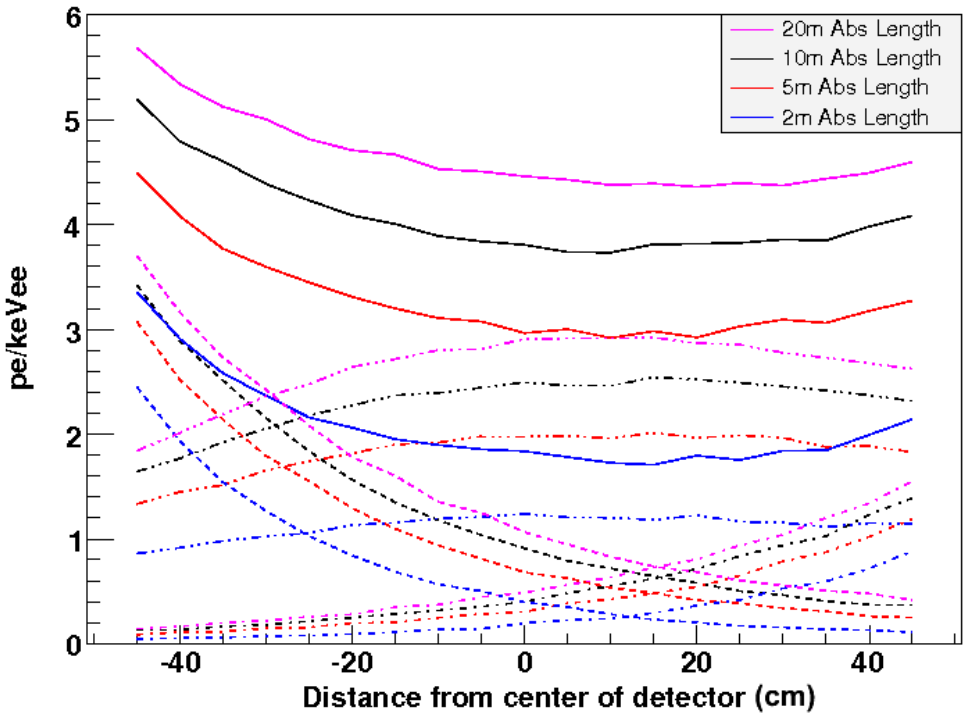

Figure 7.18: Light yield at the center of a 1 ton scale detector with PMTs on the side as a function of height in the detector for different absorption lengths, showing the light yield for the top (dashed), bottom (dotted) and side (dot-dashed) arrays, as well as the sum (solid).

the conventional 1 ton scale design.

In conclusion, for a 1 ton scale detector, there are two possibilities for TPC designs that have a sufficient light yield to obtain a suitable energy threshold. A conventional design would provide a moderate light yield of 2 pe/keV, whereas a design with PMTs on the side would increase the light yield to 3 pe/keV. For 10 ton scale detectors, however, the purity of the liquid xenon necessary to give a sufficient light yield in a conventional TPC is most likely unrealistic. Thus, a TPC with PMTs on all sides is necessary for a 10 ton scale detector, and should provide 2 - 3 pe/keV given sufficient purification.

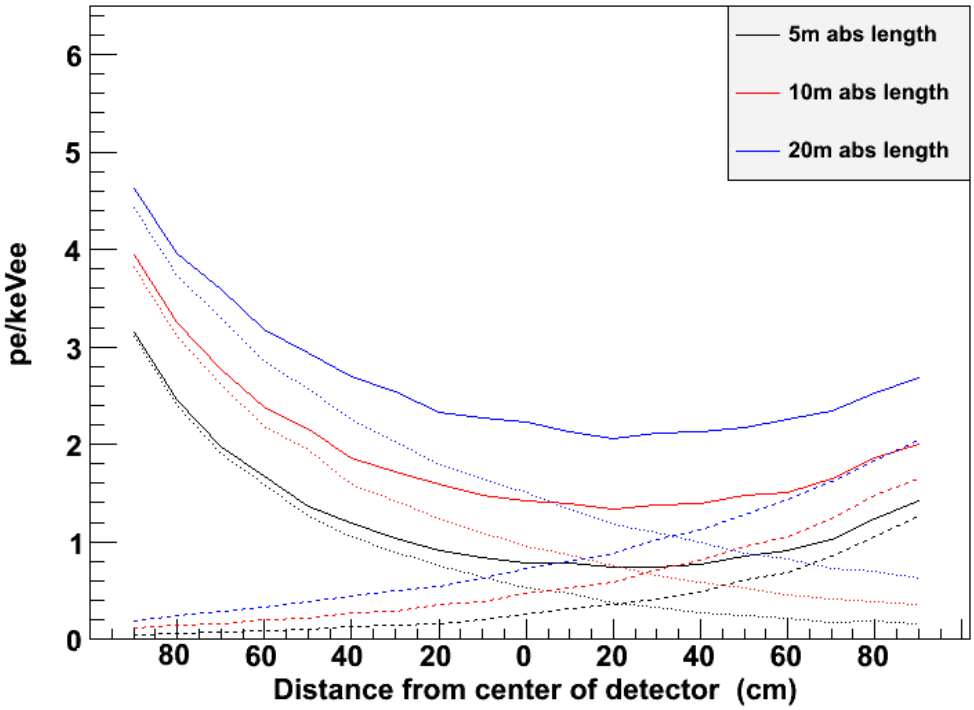

Figure 7.19: Light yield at the center of a conventional 1 ton scale detector with PMTs on the top and bottom only as a function of height in the detector for different absorption lengths, showing the light yield for the top (dashed) and bottom (dotted) arrays and the sum (solid).

7.4 Solar Neutrino Detection

By the time liquid noble detectors reach the 10 ton scale, they will be sensitive enough not only to probe small WIMP cross sections, but also to detect low energy solar neutrinos. Indeed, studies have shown that the pp chain solar neutrino scatters should be visible in 10 ton liquid xenon and liquid argon detectors [5]. In natural argon, the signal would be swamped by the beta decay signal from ^{39}Ar, so isotope separation techniques would be necessary to use an argon detector for solar neutrino detection.

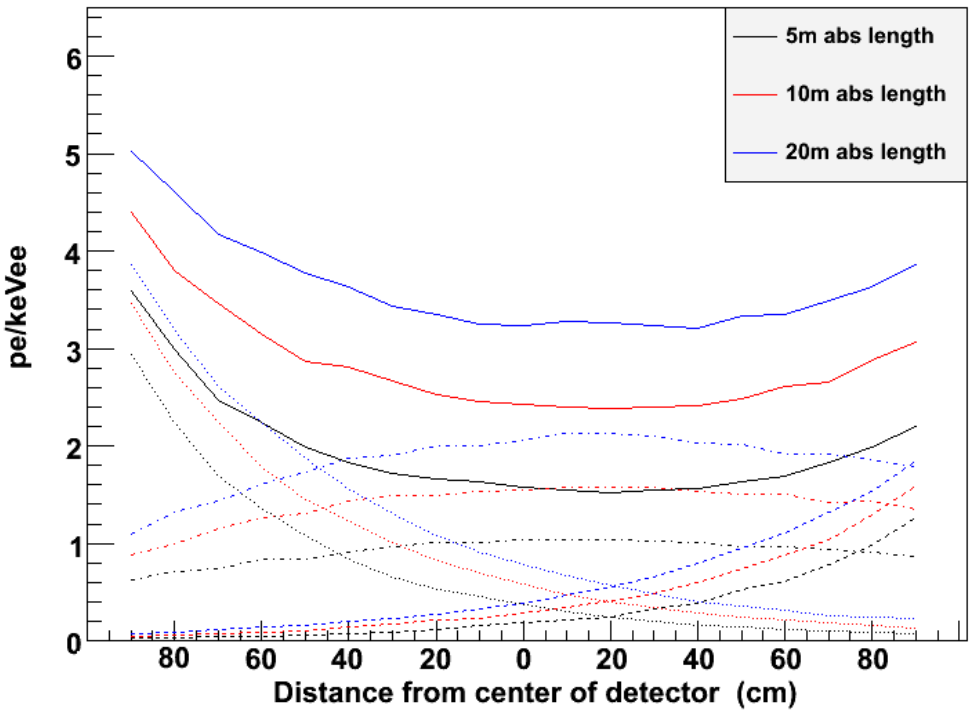

Figure 7.20: Light yield at the center of a 10 ton scale detector with PMTs on the side as a function of height in the detector for different absorption lengths, showing the light yield for the top (dashed), bottom (dotted) and side (dot-dashed) arrays, as well as the sum (solid).

7.4.1 Solar Neutrino Production

Solar neutrinos are generated inside the sun during fusion reactions in the pp chain and the CNO cycle. The pp chain, from which the majority of solar neutrinos are created, has several steps, the first of which is the combination of two protons to make deuterium.

$$ {}^1_1H + {}^1_1H \rightarrow {}^2_1H + e^+ + \nu_e \tag{7.4} $$

There are then four different mechanisms through which the deuterium fuses with hydrogen to produce ^4He, only two of which are of particular interest here. One

of these branches, lithium burning, produces monochromatic ^7Be neutrinos at 861 keV or 383 keV through the process

$$\begin{aligned} {}^3He + {}^4He &\rightarrow {}^7Be + \gamma \\ {}^7Be + e^- &\rightarrow {}^7_3Li + \nu_e \\ {}^7_3Li + {}^1_1H &\rightarrow 2\ {}^4_4He \end{aligned} \tag{7.5}$$

The other branch of interest produces high energy ^8B neutrinos through the process

$$\begin{aligned} {}^3_2He + {}^4_2He &\rightarrow {}^7_4Be + \gamma \\ {}^7_4Be + {}^1_1H &\rightarrow {}^8_5B + \gamma \\ {}^8_5B &\rightarrow {}^8_4B + e^+ + \nu_e \\ {}^8_4B &\rightarrow 2\ {}^4_4He \end{aligned} \tag{7.6}$$

The flux for each of the neutrinos listed above is shown in figure 7.21 [8]. While the high energy ^8B and ^7Be neutrinos are the only solar neutrinos that have currently been detected, the majority of the neutrino flux is composed of the low energy pp chain. Detection of the pp neutrinos is therefore an important step in confirming the solar model.

7.4.2 Neutrino Oscillations

All of the neutrinos produced within the sun are created as electron neutrinos, but this, however, is not a mass eigenstate. The three neutrino species mix to create the mass eigenstates, which are the states that propagate. The two sets of states are related by a unitary transformation by,

$$|\nu_i> = U_{i\alpha}|\nu_\alpha> \tag{7.7}$$

where the index i represents the species eigenstate, either electron, muon, or tau, α represents the mass eigenstate, and a sum on the repeated index α is implied.

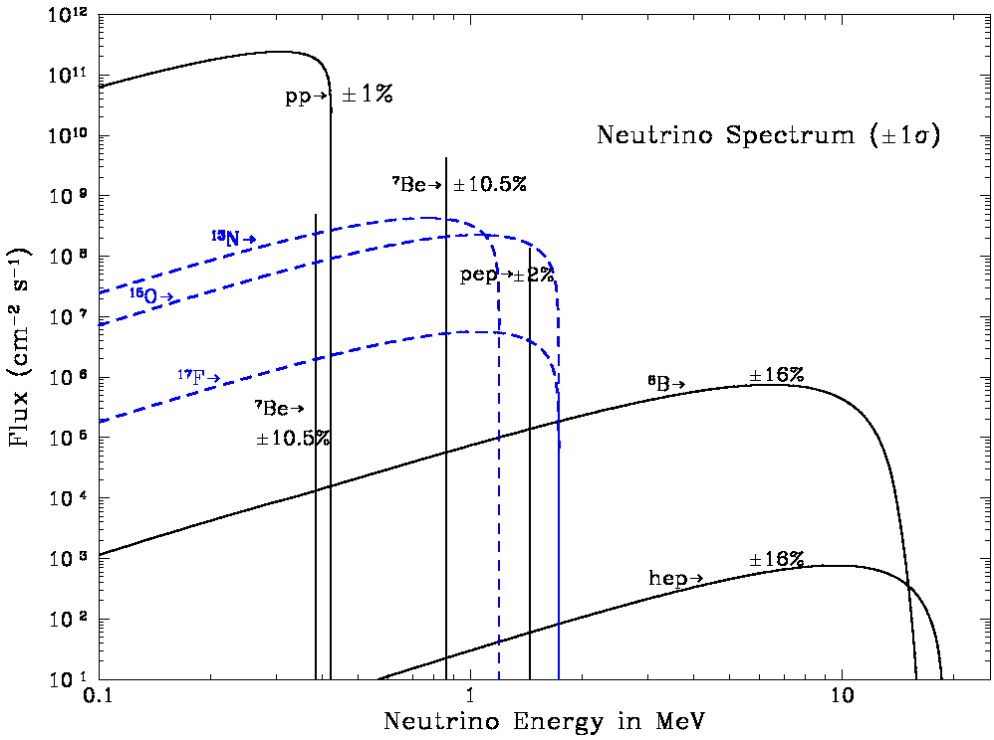

Figure 7.21: Emission Spectrum of Solar Neutrinos from [8]

This is typically written in terms of three mixing angles and three phases as [18],

$$U = \begin{pmatrix} 1 & 0 & 0 \\ 0 & c_{23} & s_{23} \\ 0 & -s_{23} & c_{23} \end{pmatrix} \times \begin{pmatrix} c_{13} & 0 & s_{13}e^{-i\delta} \\ 0 & 1 & 0 \\ -s_{13}e^{i\delta} & 0 & c_{13} \end{pmatrix} \times \begin{pmatrix} c_{12} & s_{12} & 0 \\ -s_{12} & c_{12} & 0 \\ 1 & 0 & 0 \end{pmatrix} \times \begin{pmatrix} e^{i\alpha_1/2} & 0 & 0 \\ 0 & e^{i\alpha_2/2} & 0 \\ 0 & 0 & 1 \end{pmatrix} \tag{7.8}$$

where $c_{ij} = cos\theta_{ij}$ and $s_{ij} = sin\theta_{ij}$. The phases α_i are non-zero if the neutrinos are majorana particles and do not contribute to the oscillation phenomenon. The other phase, δ, is a CP violation parameter, but this has not yet been observed in neutrino oscillation. Thus, the important parameters for neutrino oscillation are the three mixing angles θ_{ij}.

Because the mass eigenstates are those that propagate, a neutrino that is known to be produced as an electron neutrino in the sun has a probability to be in a different neutrino type state when measured on earth, a phenomenon referred to as neutrino oscillation. Further, the oscillation probability is different in the presence of matter than in vacuum, due to coherent ν_e scattering off of electrons called the MSW effect, and since ^8B neutrinos are produced deeper within the sun than pp and ^7Be neutrinos, they have different oscillation probabilities. In the case of pp and ^7Be neutrinos, the survival probability P_{ee}, or the probability of the solar neutrino to be measured as an electron neutrino, is given by [7],

$$P_{ee} = cos^4(\theta_{13})(1 - \frac{1}{2}sin^2 2\theta_{12}), \tag{7.9}$$

while for ^8B neutrinos it is given by

$$P_{ee} = cos^4\theta_{13} sin^2\theta_{12} \tag{7.10}$$

Neutrino oscillation, in general, also depends on the energy and the mass differences of neutrino species, but for solar neutrinos, these terms average out and are therefore not present in equations 7.9 and 7.10.

7.4.3 Solar Neutrino Scattering in Liquid Noble Detectors

Solar neutrinos become important in multi ton liquid noble detectors for two reasons. First, as the electron recoil background is reduced for these large detectors, the neutrino signal will ultimately be irreducible. While electron recoils are removed by S2/S1 discrimination for dark matter searches, the leak of the electron recoil band into the nuclear recoil band renders the discrimination imperfect. Thus, with the current discrimination techniques, the solar neutrino signal may ultimately become an irreducible background for dark matter searches.

The second important fact about the solar neutrino signal is that as the

electron recoil background is reduced, it will be possible to measure the solar neutrino spectrum, in particular, the yet undetected pp chain. Neutrinos scatter off of the electrons in the target, so the solar neutrino signal in different targets is ultimately determined by the sensitivity of each target to electron recoils.

There are two modes available for neutrino scattering off of electrons, a charged current interaction and a neutral current interaction. The sum of these yields the total cross section for neutrino scatters given by [17],

$$\frac{d\sigma}{dT} = \frac{2G^2 m_e}{\pi E^2}[(\frac{1}{2} + sin^2\theta_w)^2 E^2 + sin^4\theta_w (E-T)^2 - sin^2\theta_w (1+sin^2\theta_w) m_e T] \quad (7.11)$$

where E is the neutrino energy, T is the electron recoil energy, G is the Fermi constant, and θ_w is the Weinberg angle.

To detect solar neutrinos clearly above all backgrounds, several steps need to be taken, which fall naturally out of the XAX concept. The size of the detectors provides an adequate reduction of the backgrounds from the phototubes and environmental radio impurities due to the large fiducial cut. Additionally, the internal background from the double beta decay of ^{136}Xe is at the same level as the pp neutrino flux for naturally occurring xenon. However, the XAX concept already addresses this issue because of the isotope separation necessary for the spin dependence measurement and for the neutrinoless double beta decay search. Thus, the XAX detector provides a target well suited for pp solar neutrino measurement.

Combining the cross section in equation 7.11 with the solar neutrino flux, one can derive the differential energy spectrum for solar neutrino scatters in a liquid xenon detector. In figure 7.22, this has been done to find the scattering rate for pp, ^7Be and ^8B solar neutrinos as a function of recoil energy in a 10 ton liquid xenon detector depleted in ^{136}Xe to 1% the level in naturally occurring xenon. As a comparison, the WIMP scattering rate is shown for a WIMP mass between

100 GeV and 10 TeV and a cross section of 10^{-44} cm^2 (10^{-8} pb), as well as the gamma background for 5 and 10 cm fiducial cuts and the internal background from the double beta decay of ^{136}Xe.

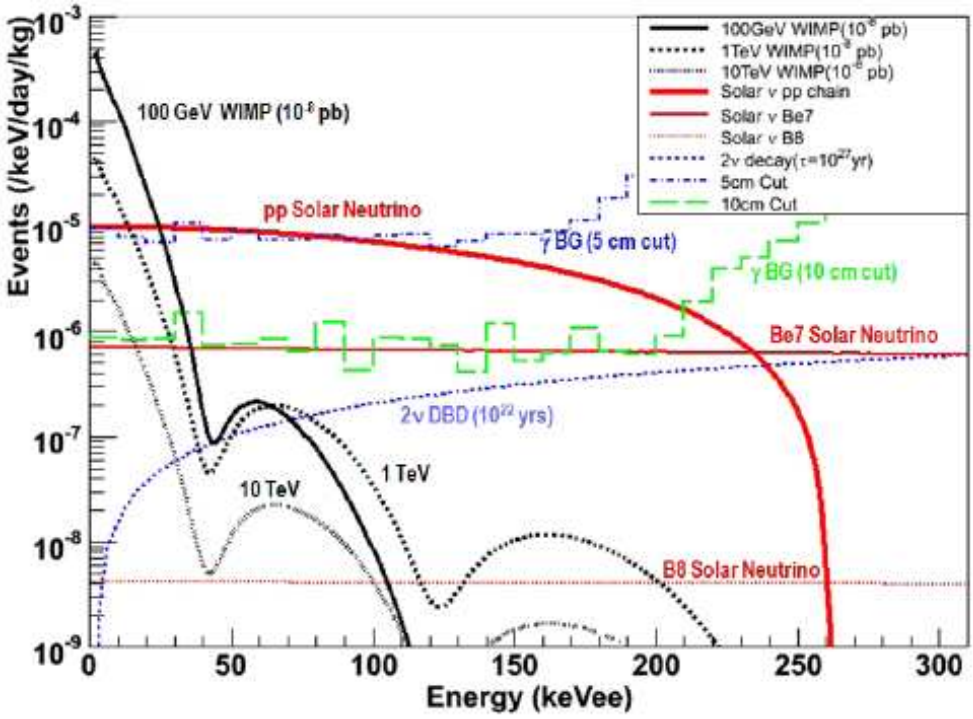

Figure 7.22: Differential rate of solar neutrinos in a liquid xenon detector

With a fiducial cut of 10 cm, the pp solar neutrino signal is clearly measurable above the background up to 200 keV. Indeed, with a 10 ton-year exposure, around 4000 events could be collected, providing a $\pm 2\%$ measurement of the pp flux.

As mentioned above, the pp solar neutrino signal is ultimately an irreducible electron recoil background for dark matter searches. As an electron recoil background, the rate can be reduced by at least two orders of magnitude by an S2/S1 cut, but this would still limit dark matter searches to a WIMP-nucleon cross section of 10^{-47} cm^2. If the WIMP is not discovered with a cross section greater than this, improved discrimination techniques may be necessary to probe smaller

cross sections.

References

[1] C. E. Aalseth et al. Results from a Search for Light-Mass Dark Matter with a P-type Point Contact Germanium Detector. *archiv:1002-4703*, 2010.

[2] Z Ahmed, D S Akerib, S Arrenberg, C N Bailey, D Balakishiyeva, L Baudis, D A Bauer, P L Brink, T Bruch, R Bunker, B Cabrera, D O Caldwell, J Cooley, P Cushman, M Daal, F DeJongh, M R Dragowsky, L Duong, S Fallows, E Figueroa-Feliciano, J Filippini, M Fritts, S R Golwala, J Hall, R Hennings-Yeomans, S A Hertel, D Holmgren, L Hsu, M E Huber, O Kamaev, M Kiveni, M Kos, S W Leman, R Mahapatra, V Mandic, K A McCarthy, N Mirabolfathi, D Moore, H Nelson, R W Ogburn, A Phipps, M Pyle, X Qiu, E Ramberg, W Rau, A Reisetter, T Saab, B Sadoulet, J Sander, R W Schnee, D N Seitz, B Serfass, K M Sundqvist, M Tarka, P Wikus, S Yellin, J Yoo, B A Young, and J Zhang. Results from a low-energy analysis of the cdms ii germanium data. Technical Report arXiv:1011.2482, Nov 2010. Comments: 5 pages, 3 figures. Supplementary material included as ancillary files.

[3] E. Aprile, L. Baudis, B. Choi, K. L. Giboni, K. Lim, A. Manalaysay, M. E. Monzani, G. Plante, R. Santorelli, and M. Yamashita. New measurement of the relative scintillation efficiency of xenon nuclear recoils below 10 kev. *Phys. Rev. C*, 79(4):045807, Apr 2009.

[4] E. Aprile, C. E. Dahl, L. de Viveiros, R. J. Gaitskell, K. L. Giboni, J. Kwong, P. Majewski, K. Ni, T. Shutt, and M. Yamashita. Simultaneous measurement of ionization and scintillation from nuclear recoils in liquid xenon for a dark matter experiment. *Phys. Rev. Lett.*, 97(8):081302, Aug 2006.

[5] K. Arisaka, H. Wang, D. Cline, A. Teymourian, E. Brown, W. Ooi, D. Aharoni, C. W. Lam, K. Lung, S. Davies, and M. Price. Xax: a multi-ton, multi-target detection system for dark matter, double beta decay and pp solar neutrinos. *Astrophysics*, 2008.

[6] F. Arneodo, B. Baiboussinov, A. Badertscher, P. Benetti, E. Bernardini, A. Bettini, A. Borio di Tiogliole, R. Brunetti, A. Bueno, E. Calligarich, M. Campanelli, C. Carpanese, D. Cavalli, F. Cavanna, P. Cennini, S. Centro, A. Cesana, D. Cline, I. De Mitri, R. Dolfini, A. Ferrari, A. Gigli Berzolari, C. Matthey, F. Mauri, D. Mazza, L. Mazzone, G. Meng, C. Montanari, G. Nurzia, S. Otwinowski, O. Palamara, D. Pascoli, A. Pepato, S. Petrera, L. Periale, G. Piano Mortari, A. Piazzoli, P. Picchi, F. Pietropaolo, T. Rancati, A. Rappoldi, G. L. Raselli, D. Rebuzzi, J. P. Revo, J. Rico, M. Rossella, C. Rossi, A. Rubbia, C. Rubbia, P. Sala, D. Scannicchio, F. Sergiampietri,

S. Suzuki, M. Terrani, W. Tian, S. Ventura, C. Vignoli, H. Wang, J. Woo, and Z. Xu. Scintillation efficiency of nuclear recoil in liquid xenon. *Nuclear Instruments and Methods in Physics Research Section A: Accelerators, Spectrometers, Detectors and Associated Equipment*, 449(1-2):147 – 157, 2000.

[7] John Bachall and Carlos Peña-Garay. Solar models and solar neutrino oscillations. *New Journal of Physics*, 6, 2004.

[8] John N. Bahcall, Aldo M. Serenelli, and Sarbani Basu. New solar opacities, abundances, helioseismology, and neutrino fluxes. *The Astrophysical Journal Letters*, 621(1):L85, 2005.

[9] R. Bernabei et al. First results from DAMA/LIBRA and the combined results with DAMA/NaI. *Eur. Phys. J.*, C56:333–355, 2008.

[10] A. Braem, A. Gonidc, D. Schinzel, W. Seidl, E. F. Clayton, G. Davies, G. Hall, R. Payne, S. Roe, C. Seez, J. Striebig, T. S. Virdee, and D. J. A. Cockerill. Observation of the uv scintillation light from high energy electron showers in liquid xenon. *Nuclear Instruments and Methods in Physics Research Section A: Accelerators, Spectrometers, Detectors and Associated Equipment*, 320(1-2):228 – 237, 1992.

[11] V.Y. Chepel, M.I. Lopes, R. Ferreira Marques, and A.J.P.L. Policarpo. Purification of liquid xenon and impurity monitoring for a pet detector. *Nuclear Instruments and Methods in Physics Research Section A: Accelerators, Spectrometers, Detectors and Associated Equipment*, 349(2-3):500 – 505, 1994.

[12] Douglas Clowe, Marusa Bradac, Anthony H. Gonzalez, Maxim Markevitch, Scott W. Randall, Christine Jones, and Dennis Zaritsky. A direct empirical proof of the existence of dark matter, 2006.

[13] XENON100 Collaboration. Reply to the comments on the xenon100 first dark matter results. Technical Report arXiv:1005.2615, May 2010.

[14] Xenon100 Collaboration, E. Aprile, K. Arisaka, F. Arneodo, A. Askin, L. Baudis, A. Behrens, E. Brown, J. M. R. Cardoso, B. Choi, D. B. Cline, S. Fattori, A. D. Ferella, K. L. Giboni, K. Hugenberg, A. Kish, C. W. Lam, J. Lamblin, R. F. Lang, K. E. Lim, J. A. M. Lopes, T. Marrodán Undagoitia, Y. Mei, A. J. Melgarejo Fernandez, K. Ni, U. Oberlack, S. E. A. Orrigo, E. Pantic, G. Plante, A. C. C. Ribeiro, R. Santorelli, J. M. F. Dos Santos, M. Schumann, P. Shagin, A. Teymourian, D. Thers, E. Tziaferi, H. Wang, and C. Weinheimer. First dark matter results from the xenon100 experiment. May 2010.

[15] J. I. Collar and D. N. McKinsey. Comments on "first dark matter results from the xenon100 experiment". May 2010.

[16] J I Collar and D N McKinsey. Response to arxiv:1005.2615. Technical Report arXiv:1005.3723, May 2010.

[17] Andre de Gouvea and James Jenkins. What can we learn from neutrino electron scattering? *Phys. Rev.*, D74:033004, 2006.

[18] S. Eidelman, K. G. Hayes, K. A. Olive, M. Aguilar-Benitez, C. Amsler, D. Asner, K. S. Babu, R. M. Barnett, J. Beringer, P. R. Burchat, C. D. Carone, S. Caso, G. Conforto, O. Dahl, G. D'Ambrosio, M. Doser, J. L. Feng, T. Gherghetta, L. Gibbons, M. Goodman, C. Grab, D. E. Groom, A. Gurtu, K. Hagiwara, J. J. Hernndez-Rey, K. Hikasa, K. Honscheid, H. Jawahery, C. Kolda, Y. Kwon, M. L. Mangano, A. V. Manohar, J. March-Russell, A. Masoni, R. Miquel, K. Mnig, H. Murayama, K. Nakamura, S. Navas, L. Pape, C. Patrignani, A. Piepke, G. Raffelt, M. Roos, M. Tanabashi, J. Terning, N. A. Trnqvist, T. G. Trippe, P. Vogel, C. G. Wohl, R. L. Workman, W. M. Yao, P. A. Zyla, B. Armstrong, P. S. Gee, G. Harper, K. S. Lugovsky, S. B. Lugovsky, V. S. Lugovsky, A. Rom, M. Artuso, E. Barberio, M. Battaglia, H. Bichsel, O. Biebel, P. Bloch, R. N. Cahn, D. Casper, A. Cattai, R. S. Chivukula, G. Cowan, T. Damour, K. Desler, M. A. Dobbs, M. Drees, A. Edwards, D. A. Edwards, V. D. Elvira, J. Erler, V. V. Ezhela, W. Fetscher, B. D. Fields, B. Foster, D. Froidevaux, M. Fukugita, T. K. Gaisser, L. Garren, H. J. Gerber, G. Gerbier, F. J. Gilman, H. E. Haber, C. Hagmann, J. Hewett, I. Hinchliffe, C. J. Hogan, G. Hhler, P. Igo-Kemenes, J. D. Jackson, K. F. Johnson, D. Karlen, B. Kayser, D. Kirkby, S. R. Klein, K. Kleinknecht, I. G. Knowles, P. Kreitz, Yu. V. Kuyanov, O. Lahav, P. Langacker, A. Liddle, L. Littenberg, D. M. Manley, A. D. Martin, M. Narain, P. Nason, Y. Nir, J. A. Peacock, H. R. Quinn, S. Raby, B. N. Ratcliff, E. A. Razuvaev, B. Renk, G. Rolandi, M. T. Ronan, L. J. Rosenberg, C. T. Sachrajda, Y. Sakai, A. I. Sanda, S. Sarkar, M. Schmitt, O. Schneider, D. Scott, W. G. Seligman, M. H. Shaevitz, T. Sjstrand, G. F. Smoot, S. Spanier, H. Spieler, N. J. C. Spooner, M. Srednicki, A. Stahl, T. Stanev, M. Suzuki, N. P. Tkachenko, G. H. Trilling, G. Valencia, K. van Bibber, M. G. Vincter, D. R. Ward, B. R. Webber, M. Whalley, L. Wolfenstein, J. Womersley, C. L. Woody, O. V. Zenin, and R. Y. Zhu. Review of particle physics. *Physics Letters B*, 592(1-4):1 – 5, 2004. Review of Particle Physics.

[19] C Savage et al. Compatibility of DAMA/LIBRA dark matter detection with other searches in light of new Galactic rotation velocity measurements. *JCAP*, 2009.

[20] Z. Ahmed et al. Dark matter search results from the cdms ii experiment. *Science*, 327(5973):1619–1621, 2010.

[21] Gary J. Feldman and Robert D. Cousins. Unified approach to the classical statistical analysis of small signals. *Phys. Rev. D*, 57(7):3873–3889, Apr 1998.

[22] C. Goebbert, R. Nonninger, M. A. Aegerter, and H. Schmidt. Wet chemical deposition of ato and ito coatings using crystalline nanoparticles redispersable in solutions. *Thin Solid Films*, 351(1-2):79 – 84, 1999.

[23] Richard H. Helm. Inelastic and elastic scattering of 187-mev electrons from selected even-even nuclei. *Phys. Rev.*, 104(5):1466–1475, Dec 1956.

[24] Christian Hurtgen, Simon Jerome, and Mike Woods. Revisiting currie – how low can you go? *Applied Radiation and Isotopes*, 53(1-2):45 – 50, 2000.

[25] N. Ishida, M. Chen, T. Doke, K. Hasuike, A. Hitachi, M. Gaudreau, M. Kase, Y. Kawada, J. Kikuchi, T. Komiyama, K. Kuwahara, K. Masuda, H. Okada, Y. H. Qu, M. Suzuki, and T. Takahashi. Attenuation length measurements of scintillation light in liquid rare gases and their mixtures using an improved reflection suppresser. *Nuclear Instruments and Methods in Physics Research Section A: Accelerators, Spectrometers, Detectors and Associated Equipment*, 384(2-3):380 – 386, 1997.

[26] N. Ishida, T. Doke, J. Kikuchi, K. Kuwahara, T. Kashiwagi, M. Ichige, K. Hasuike, K. Ito, S. Ben, A. Hitachi, Y.H. Qu, K. Masuda, M. Suzuki, M. Kase, T. Takahashi, M. Chen, S. Sumorok, M. Gaudreau, and E. Aprile. Measurement of attenuation length of scintillation light in liquid xenon. *Nuclear Instruments and Methods in Physics Research Section A: Accelerators, Spectrometers, Detectors and Associated Equipment*, 327(1):152 – 154, 1993.

[27] Gerard Jungman, Marc Kamionkowski, and Kim Griest. Supersymmetric dark matter. *Phys. Rept.*, 267:195–373, 1996.

[28] D. Larson, J. Dunkley, G. Hinshaw, E. Komatsu, M. R. Nolta, C. L. Bennett, B. Gold, M. Halpern, R. S. Hill, N. Jarosik, A. Kogut, M. Limon, S. S. Meyer, N. Odegard, L. Page, K. M. Smith, D. N. Spergel, G. S. Tucker, J. L. Weiland, E. Wollack, and E. L. Wright. Seven-year wilkinson microwave anisotropy probe (wmap) observations: Power spectra and wmap-derived parameters. *Astrophysics*, 2010.

[29] J. D. Lewin and P. F. Smith. Review of mathematics, numerical factors, and corrections for dark matter experiments based on elastic nuclear recoil. *Astroparticle Physics*, 6(1):87 – 112, 1996.

[30] A. Manzur, A. Curioni, L. Kastens, D. N. McKinsey, K. Ni, and T. Wongjirad. Scintillation efficiency and ionization yield of liquid xenon for monoenergetic nuclear recoils down to 4 kev. *Phys. Rev. C*, 81(2):025808, Feb 2010.

[31] D. N. McKinsey, C. R. Brome, J. S. Butterworth, S. N. Dzhosyuk, R. Golub, K. Habicht, P. R. Huffman, C. E. H. Mattoni, L. Yang, and J. M. Doyle. Detecting ionizing radiation in liquid helium using wavelength shifting light collection. *Nuclear Instruments and Methods in Physics Research Section A: Accelerators, Spectrometers, Detectors and Associated Equipment*, 516(2-3):475 – 485, 2004.

[32] Gioacchino Ranucci, Danilo Giugni, Istvan Manno, Anna Preda, Patrizia Ullucci, Alexei Golubchikov, and Oleg Smirnov. Characterization and magnetic shielding of the large cathode area pmts used for the light detection system of the prototype of the solar neutrino experiment borexino. *Nuclear Instruments and Methods in Physics Research Section A: Accelerators, Spectrometers, Detectors and Associated Equipment*, 337(1):211 – 220, 1993.

[33] V. C. Rubin and W. K. Ford, Jr. Rotation of the Andromeda Nebula from a Spectroscopic Survey of Emission Regions. , 159:379–+, February 1970.

[34] Christopher Savage, Graciela Gelmini, Paolo Gondolo, and Katherine Freese. Xenon10/100 dark matter constraints in comparison with cogent and dama: examining the leff dependence. 2010.

[35] G. M. Seidel, R. E. Lanou, and W. Yao. Rayleigh scattering in rare-gas liquids. *Nuclear Instruments and Methods in Physics Research Section A: Accelerators, Spectrometers, Detectors and Associated Equipment*, 489(1-3):189 – 194, 2002.

[36] P. Sorensen, A. Manzur, C.E. Dahl, J. Angle, E. Aprile, F. Arneodo, L. Baudis, A. Bernstein, A. Bolozdynya, L.C.C. Coelho, L. DeViveiros, A.D. Ferella, L.M.P. Fernandes, S. Fiorucci, R.J. Gaitskell, K.L. Giboni, R. Gomez, R. Hasty, L. Kastens, J. Kwong, J.A.M. Lopes, N. Madden, A. Manalaysay, D.N. McKinsey, M.E. Monzani, K. Ni, U. Oberlack, J. Orboeck, G. Plante, R. Santorelli, J.M.F. dos Santos, P. Shagin, T. Shutt, S. Schulte, C. Winant, and M. Yamashita. The scintillation and ionization yield of liquid xenon for nuclear recoils. *Nuclear Instruments and Methods in Physics Research Section A: Accelerators, Spectrometers, Detectors and Associated Equipment*, 601(3):339 – 346, 2009.

[37] Roberto Trotta, Farhan Feroz, Mike Hobson, Leszek Roszkowski, and Roberto Ruiz de Austri. The impact of priors and observables on param-

eter inferences in the constrained mssm. *Journal of High Energy Physics*, 2008(12):024, 2008.

[38] K. Weise, K. Hubel, E. Rose, M. Schlager, D. Schrammel, M. Taschner, and R. Michel. Bayesian decision threshold, detection limit and confidence limits in ionising-radiation measurement. *Radiat Prot Dosimetry*, 121:52–63, December 2006.